SISSA
Scuola
Internazionale
Superiore di
Studi Avanzati

Physics Area – PhD course in

Theory and Numerical Simulation of Condensed Matter

A Multi-scale Approach to Studying the Complexity in Glutamine Aggregates: Structure, Dynamics and Electronic Properties.

Candidate:

Muhammad Nawaz Qaisrani

Advisors:

Prof. Ali Hassanali

Prof. Ralph Gebauer

Internal Advisor:

Prof. Stefano Baroni

SISSA

Scuola
Internazionale
Superiore di
Studi Avanzati

Academic Year 2018-19

OFFICE NAME

Via Bonomea, 265
34136 Trieste – Italy
T +39 0403787111
E info@sissa.it
sissa.it

Abstract

Single amino acid glutamine crystals have recently been shown to exhibit non-aromatic intrinsic fluorescence during their aggregation in aqueous solution. The optical activity of these systems is similar to other complex proteins like amyloids which are involved in various types of neurodegenerative diseases such as Alzheimer and Parkinson. We use a multi-scale atomistic simulation approach to dissect in detail the chemical and structural complexities associated with glutamine crystals.

We investigate the ground and excited-state properties of the three different glutamine systems. Our results show that one system that has short hydrogen bonds absorbs light at low energy and is optically brighter, a finding that is consistent with the experimental observation.

As a consequence of thermal fluctuations, the proton transfer occurs along the short hydrogen bond. The corresponding free energy profile is characterised by an asymmetric double-well potential. We also investigate the role of the vibrational modes in the excited state. Our results show that the optical properties of glutamine crystals are sensitive to the initial conditions in the ground state and tuned by the collective vibrational modes in the excited state.

Different glutamine aggregates differ in terms of their hydrogen bond network. We present a classical versus quantum mechanical analysis of the proton motion along different hydrogen bonds, where we show that the nuclear quantum effects strengthen the short hydrogen bonds and enhance electronic polarisation.

Finally, we investigate the coupling of glutamine crystals with the surrounding water by using large scale molecular dynamics simulations. We study the structural and dynamical properties of water near different crystalline surfaces of L-glutamine crystals. Despite having the same molecular composition, water at each surface displays characteristic structural, orientational and dynamical correlations. This behaviour is tuned by how the different chemical groups of the amino-acids make contact with the liquid phase. We show that the binding of glutamine molecules to the crystal surface creates a crowded environment involving pockets of trapped water molecules altering the water dynamics in a highly non-trivial manner suggesting that the solvent dynamics may have important implications on crystal nucleation.

Table of contents

List of figures

List of tables

Chapter 1

Introduction

Self-assembly of biological matter is a fundamental problem to understand the structure and function of multimeric biomolecules such as proteins [7, 8]. Proteins and peptides are self-assembled through a wide variety of chemical interactions which includes hydrogen bonds, electrostatic interactions, water-mediated hydrogen bonds, hydrophobic and hydrophilic interactions and van der Waals forces. These non-covalent interactions are the key ingredients of all the aggregation processes and the stability of large biomolecular ensembles [9–12]. The native self-assemblies of proteins build a vast array of structures such as keratin, collagen, pearl, shell and coral, which performs a wide variety of biological functions [13–15].

However, in certain conditions, the self-assembled processes lead to misfolded and insoluble protein aggregates which are involved in various types of neurodegenerative disorders such as Alzheimer, Parkinson and Huntington diseases [16–20]. These misfolded protein aggregates are called Amyloid proteins and have been the subject of intense research for several decades [21–24]. A schematic picture of the aggregation mechanism of folded and misfolded proteins is illustrated in Fig. 1.1 [1]. The most common structural feature in all amyloid aggregates is the presence of a dense network of hydrogen bonds. The network stabilizes the parallel and anti-parallel stacking of the beta-sheets which form elongated protofibrils [25, 26]. Relative to other protein structures, the ordered stacking of beta-sheets and hydrogen bond packing provides amyloids tremendous structural stability. Fig. 1.2 illustrates the thermodynamics of different protein aggregates. It is clear from the figure that the ordered amyloid assemblies lay deep in the minimum energy of their intermolecular and intramolecular contacts [2]. There are ongoing studies to understand the various structural and kinetic factors that lead to amyloids aggregation and formation of their hydrogen bond network [27].

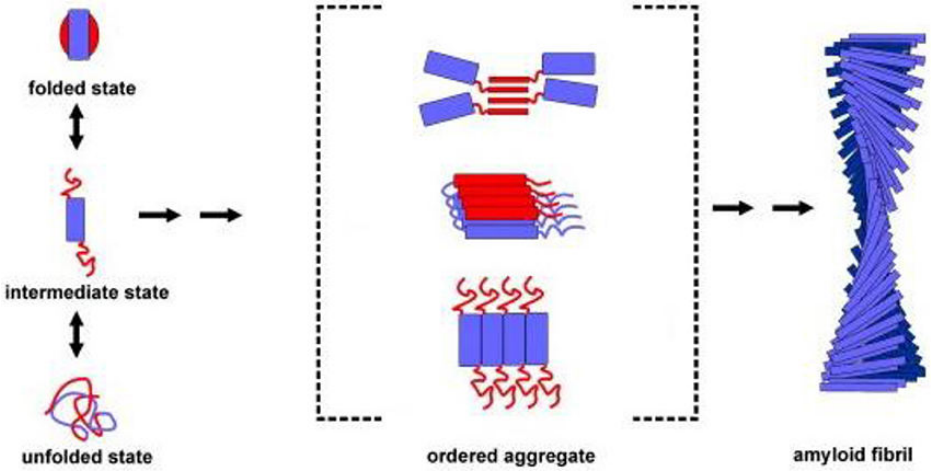

Fig. 1.1 A schematic picture of the aggregation mechanism of folded and misfolded proteins. The self-assembled processes lead through several intermediate states to either natively folded proteins or in certain conditions to misfolded ordered aggregates. These ordered aggregates further leads to form mature elongated amyloid protofibrils. This figure is reproduced from Ref. [1]

Most of the proteins self-assembly and aggregation processes discussed earlier occur in aqueous solutions. It is well known that water plays a fundamental role in determining the structure, stability and function of biomolecules like proteins [28–30]. Similarly, the proteins perturb the structure and dynamics of water in their vicinity [31]. Numerous studies have been devoted to understand this coupling (protein-water) both on theoretical and experimental sides [31, 30, 32–35]. One of the fundamental problems in biophysical chemistry pertains at which extent water near the biological interfaces is altered and in particular, how different it is from the bulk. Much cumulative evidence over the last few decades shows that water in the hydration shell of proteins is slowed by a factor of $\sim$4-7 [31].

However, understanding the water retardation near biological interfaces is a challenging task as water dynamics is coupled to the soft modes associated with the protein fluctuations [36–39]. Therefore, the interfaces such as amyloid proteins and other self-assembled stable protein aggregates serve as excellent systems to investigate origins of water retardation in the vicinity of proteins.

Monitoring the self-assembly processes in aqueous solution with experiments is essential to understand the aggregation mechanism of the proteins. One possible way to monitor these processes is through fluorescence [40, 41], which is a powerful experimental tool to study protein folding, binding interactions and aggregation [40–43]. Generally in proteins, the conventional source of fluorescence is associated with the presence of aromatic amino acids

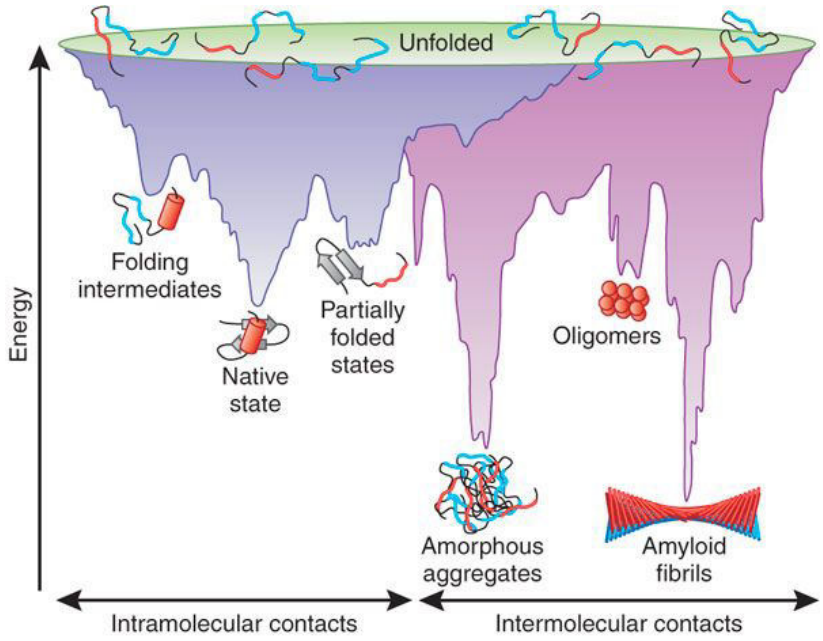

Fig. 1.2 Schematic energy landscape for protein folding and aggregation in terms of intramolecular and intermolecular contacts. The figure is reproduced from Ref. [2].

or conjugated bonds that lead to electron delocalisation [44, 45, 41]. The three aromatic aminoacid are the phenylalanine (Phe), tryptophan (Trp) and tyrosine (Tyr) [41]. These amino acids tend to absorb light in ultraviolet (UV) range and emit in the visible. Among these amino acids, tryptophan has the highest quantum yield, and its photoactivity is sensitive to its location and its interaction with the chemical environment around [46, 47]. The fluorescence characteristic of the three aromatic amino acids is depicted in Fig. 1.3. Furthermore, there are some particular proteins such as Green Fluorescent Proteins (GFP) found for the first time in a jellyfish, aequorea victoria. GFP has a sequential serine-tyrosine-glycine internal structure which modified post-translationally and fluorescent in the visible [48, 49]. GFP are widely used as a fluorescent tag to monitor many biological processes [50–52].

In 2004 Guptasharma's lab in India observed a different type of fluorescence in different protein crystals and aggregates, which is independent of the presence of aromatic residues [53]. This fluorescence is somewhat specific to structures which contain high proportions of the β sheets. After these observations, there have been various experimental studies confirming this emission developed in a range of protein crystals and aggregates [54–57]. The fluorescence intensities of different protein crystals and aggregates are shown in the middle panel of Fig. 1.4. Furthermore, it has been observed that the fluorescence increases with the aggregation time, as illustrated in the lower panel of Fig. 1.4.

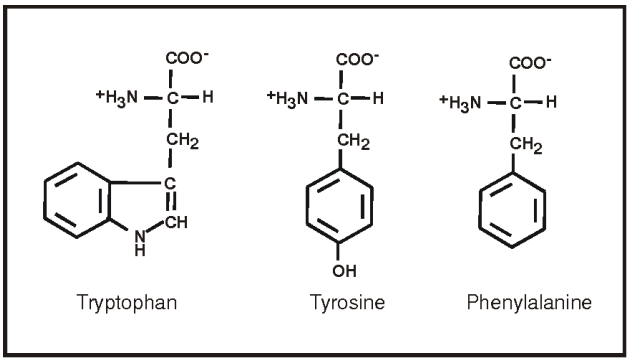

	Absorption		Fluorescence	
Amino Acid	Wavelength (nm)	Absorbtivity	Wavelength (nm)	Quantum Yield
Tryptophan	280	5,600	348	0.20
Tyrosine	274	1,400	303	0.14
Phenylalanine	257	200	282	0.04

Fig. 1.3 Upper panel: The chemical structure of the three aromatic amino acids is shown. Lower panel: The fluorescence characteristic of the aromatic amino acids, where tryptophan emits at longer wave length with highest quantum yield. The figure is reproduces from Ref. [3].

Despite these exciting observations have been made on the experimental side, the origin describing this emission still remains elusive. Different previous studies proposed different hypotheses on the origins of this photophysics. For instance, Shukla et al [53] observed first time intrinsic fluorescence in nonaromatic proteins and hypothesized that the delocalization of peptide electrons through intramolecular or intermolecular hydrogen bond formation is responsible for this emission. Likewise, Homchaudhuri and coworkers [58], observed the emission from concentrated solutions of L-lysine monohydrochloride and described it to the gathering of amino (NH2) side chains. Furthermore, De Mercato et al [56], suggested that within the cross-β structure, the hydrogen-bonded water molecules are responsible for the peptide emission. Recently, Ye and coworkers [59] linked the peptide emission to the interactions between amide groups.

In 2016 some of our collaborators in collaboration with Kaminski lab in Cambridge took the first step to combine fluorescence spectroscopy and state of the art atomistic simulations methods such as *ab initio* molecular dynamics and time-dependent density functional theory on model amyloid systems [57]. They suggest that the proton transfer specific to strong hydrogen bonds lowers the excited state energy, hence coupled to the photoabsorption of these systems.

However, the generality of this result and particularly, the role of vibrational modes upon excitation in non-aromatic systems, has not been elucidated. We have thus searched for model systems and inspired from recent experiments on single amino acid-based structures

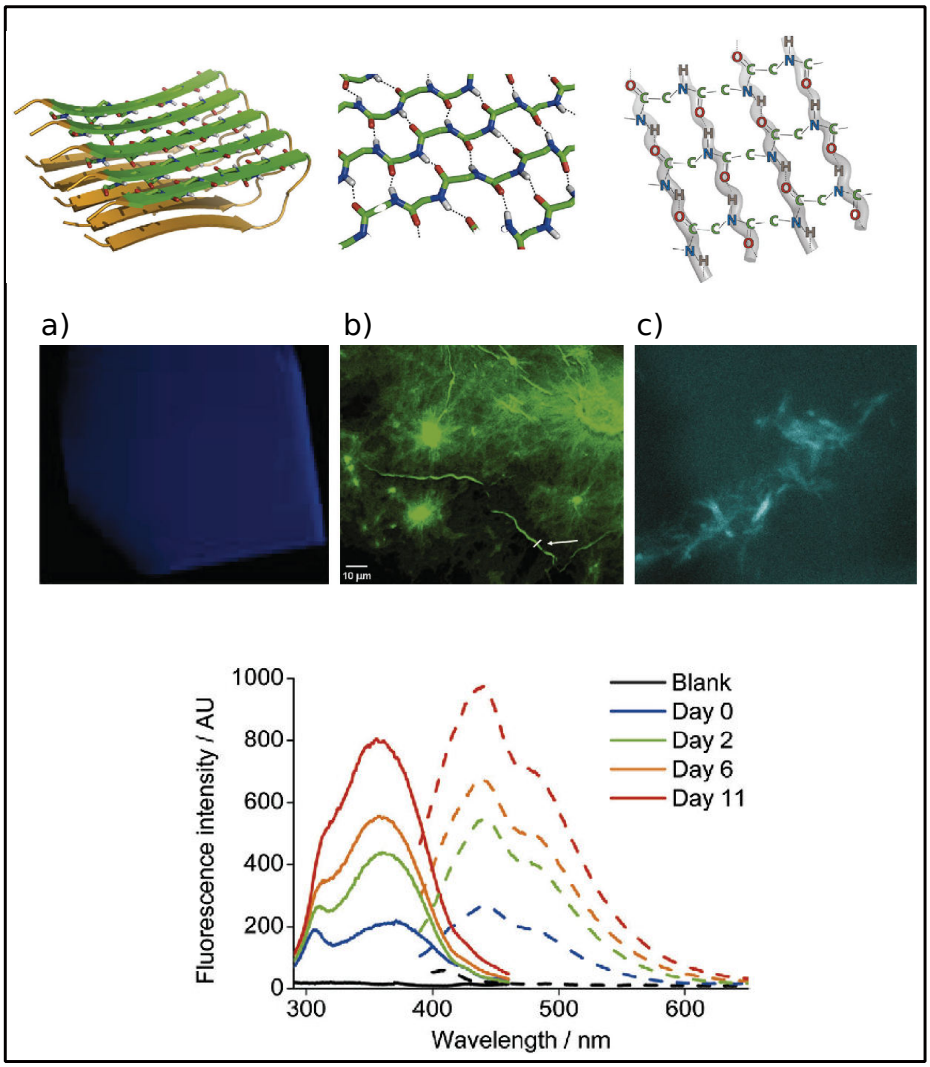

Fig. 1.4 Top panel: Structural model for $A_{\beta 42}$ amyloid fibrils (2BEG) (left) in which the backbone atoms of one of the β-sheets have been highlighted. The zoomed structure (middle and right) illustrating the hydrogen bond network [4]. Middle panel: Intrinsic fluorescence of different protein crystals and aggregates. a) Crystal of hen egg white lysozyme. b) Fibrillar aggregates of poly (VGGLG) and C) Fibrillar aggregate of GVGVAGVG. Bottom panel: The time resolved excitation (solid lines) and emission (dashed lines) spectra of hen egg white lysozyme (HEWL) is illustrated during the aggregation process. The behaviour shows that the intrinsic fluorescence intensity increased with amyloid formation. The figures are reproduced from Ref. [4].

(L-glutamine aggregates) that displays similar optical properties to amyloids.
The experiments show that the non-aromatic L-glutamine [5], dissolved in water and hydrolyse to form a new structure which is previously unknown and resemble L-pyroglutamine [6]. This chemical transformation leads to a very short hydrogen bond in the structure and the new system optically bright compare to the parent structure. We thus used these structures as model systems and their small size and chemical simplicity allow us to investigate their optical properties with more sophisticated computational approaches.
In this thesis, we used a multiscale atomistic simulation approach to dissect in detail the chemical and structural complexities associated with single amino acid crystals. We interrogate their coupling with the surrounding water and investigate the molecular origins of their intrinsic fluorescence.

The thesis is organised as follows: In Chapter 2, we provide a comprehensive review of the theory of computational methods used in this work. The ground and excited-state properties of different glutamine systems are discussed in Chapter 3. Here we show that the structure with a short hydrogen bond is optically more bright. Chapter 4 is dedicated to investigating the role of nuclear quantum effects on the structural, dynamical and electronic properties of different hydrogen bonds in glutamine systems. In Chapter 5, we used large scale molecular dynamics simulations to model glutamine systems in aqueous solutions and investigated their coupling with the surrounding water. We use different surfaces of L-glu systems to interrogate the heterogeneities of water structure and dynamics at the interface. In Chapter 6, we will summarize the main findings of this thesis and will discuss the future perspectives.

Chapter 2

Theoretical Background

In this chapter, we will briefly describe the theoretical background of various atomistic simulation methods used to assess the structural, dynamical and optical properties of self-assembled amino acid aggregates. For computational modelling of these systems in aqueous solution, and determination of their interfacial properties, we used large scale molecular dynamics (MD) simulations with empirical force field methods (Section 2.1). The optical properties of these systems such as absorption spectra and nature of electronic excitations were investigated by combining *ab initio* molecular dynamics (AIMD) (Section 2.2) and time-dependent density functional theory (TDDFT) (Section 2.4). As L-glutamine crystals are rich in hydrogen bonds and due to the light mass of the protons, the role of the nuclear quantum effects on the structural and electronic properties of these systems is investigated by conducting path integral molecular dynamics simulations (Section 2.5).

2.1 Classical Molecular Dynamics

Molecular dynamics is a powerful technique to monitor the motion of atoms and molecules and determine from their time evolution the static and dynamical properties of a system. The applications of MD simulations are vast, ranging from studies of liquids, defects, surfaces and interfaces, friction phenomenon, biomolecular ensembles and many more. The basic ingredient of MD simulations is the time evolution of the atomic trajectories obtained by integrating Newton's equations of motion.

$$\vec{F}_i = m_i \vec{a}_i, [i = 1...N] \tag{2.1}$$

Where F_i is the force on i^{th} particle with mass m_i, moving with acceleration $\vec{a}_i = \frac{d^2\vec{x}_i}{dt^2}$. The forces between the particles are then calculated from the gradient of potential with respect to atomic positions such as:

$$\vec{F}_i = -\vec{\nabla}_{ri} V(\vec{r}_1, ...\vec{r}_N) \tag{2.2}$$

For large biomolecular systems, it is computationally not feasible to compute the accurate potential from quantum chemistry electronic structure calculations. Therefore the modelling of the physical interactions between the atoms is done by using simple classical functions called Force Fields. The atoms in this description are considered as point charges and various components of these potential functions are defined in terms of bonded interactions such as stretches, bending and twists and also non bonded interactions which are mainly electrostatic and van der Waals. The modelling of such functions introduces a large number of parameters which are optimised to give good agreement with quantum chemistry calculations or with experimental data [60]. There are various families of force fields developed by different groups to model physical interactions of the soft matter. A few widely used force fields are AMBER [61], CHARMM [62] and OPLSA [63] force fields. A typical force field function defines as:

$$V(\vec{r}) = V_{bonded}(\vec{r}) + V_{non-bonded}(\vec{r}) \tag{2.3}$$

where,

$$V_{bonded}(\vec{r}) = \sum_{bonds} k_b(l-l_0)^2 + \sum_{angles} k_\theta(\theta-\theta_0)^2 + \sum_{dihedral}\sum_{n}\frac{1}{2}V_n[1+cos(n\phi-\gamma)] \tag{2.4}$$

and

$$V_{nonbonded}(\vec{r}) = \sum_{j=1}^{N-1}\sum_{i=j+1}^{N} f_{ij}\Big\{\frac{q_i q_j}{4\pi\varepsilon_0\vec{r}_{ij}} + \varepsilon_{ij}\Big[(\frac{r_{0ij}}{\vec{r}_{ij}})^{12} - 2(\frac{r_{0ij}}{\vec{r}_{ij}})^6\Big]\Big\} \tag{2.5}$$

The terms in equation 2.4 are different bonded interactions of atoms connected through covalent bonds with bond lengths (l), angles (θ) and the dihedrals (ϕ) and the equation 2.5 represents the non covalent bonded terms for long range electrostatic and van der Waals energies. The van der Waals interactions can be modeled by Lennard Jones potential function. The parameters associated to each term in equations 2.4 and 2.5 are optimized from the experimental data or from quantum chemistry calculations. Where all the bonds, angles

and dihedral angles are defined from the atomic coordinates $\vec{r}(t)$ obtained by integrating equation 2.1. Several algorithms exist to numerically integrate equations of motion such as some of the widely used Verlet [64] and velocity Verlet [65] algorithms. These algorithms are built on the basis of Taylor expansion of the coordinates at time $t \pm \Delta t$, where Δt is the time step. The mathematical expression of Verlet and velocity Verlet algorithms is written as

$$\vec{r}(t+\Delta t) = \vec{r}(t) + \vec{v}(t)\Delta t + \frac{1}{2}\vec{a}(t)\Delta t^2 \tag{2.6}$$

$$\vec{v}(t+\Delta t) = \vec{v}(t) + \frac{\vec{a}(t) + \vec{a}(t+\Delta t)}{2}\Delta t \tag{2.7}$$

At each time step, the forces are computed, which is the most expensive part of the simulation. Then by using equation 2.6 and equation 2.7, atomic coordinates and velocities are updated and at the end, physical quantities expressed in terms of $\vec{r}(t)$ and $\vec{v}(t)$ can be computed using statistical averages.

2.2 Density Functional Theory (DFT)

With its strong predictive power to study the electronic ground-state properties of N electrons systems, density functional theory is remarkably widespread in the condensed matter physics and quantum chemistry communities since its first appearance in 1964. The main achievement of this approach is to provide approximate calculations on many electrons systems by using functionals of the electronic density rather than constructing complex many-body wavefunctions or their equivalent. The theoretical development of DFT was done by the work of Hohenberg and Kohn [66] and later by Kohn and Sham [67]. The two famous theorems established by Hohenberg and Kohn (HK) constitute the theoretical foundation of DFT. The first theorem states that for a many electrons system with nondegenerate ground state, all the ground state properties such as external potential and total energy are completely determined by the electron density (up to an additive constant). The second HK theorem is simply a corollary to the first and states that the energy of an interacting-electron system $E_{HK}[n]$ in an external potential $v_{ext}(\vec{r})$ can be expressed as a functional of the electronic density,

$$E_{HK}[n] = F_{HK}[n] + \int v_{ext}(\vec{r})n(\vec{r})d\vec{r} \tag{2.8}$$

where $F_{HK}[n]$ is the universal i.e. sytem independent function of the electronic density $n(\vec{r})$ and does not depend on the external potential $v_{ext}(\vec{r})$. Furthermore, $E_{HK}[n]$ is minimal on the ground state density $n_0(\vec{r})$ and its value at $n_0(\vec{r})$ is the exact ground state energy of the

many electrons system. The two HK theorems provide a general theoretical result but do not contain any recipe to solve the quantum many-body problem in practice. One year later, the practical formulation of DFT was established by Kohn and Sham. The Kohn-Sham (KS) ansatz is to map within the framework of DFT the many-body system onto an auxiliary system of non-interacting particles by rewriting the equation 2.8 as:

$$E_{KS}[n] = T_0[n] + E_H[n] + E_{xc}[n] + \int v_{ext}(\vec{r})n(\vec{r})d\vec{r} \tag{2.9}$$

Where T_0 is the F_{HK} functional of non-interacting electrons system, coinciding therefore with its kinetic energy;

The Hartree energy term $E_H[n]$ in equation 2.9 represents the electrostatic interaction energy written as a functional of $n(\vec{r})$ as:

$$E_H[n] = \frac{1}{2}\int \frac{n(\vec{r})n(\vec{r}')}{|\vec{r}-\vec{r}'|}d\vec{r}d\vec{r}' \tag{2.10}$$

Finally the term $E_{xc}[n]$ is defined as the difference $F_{HK}[n] - T_0[n] - E_H[n]$ and accounts for the exchange and correlation effects arise from the many body nature of the electronic system. Formally DFT is an exact theory, but the correct functional form of $E_{xc}[n]$ is not known, therefore to apply DFT in practice, a good approximation on $E_{xc}[n]$ is necessary. Section 2.3 will briefly describe the different approximations made on defining the functional form of $E_{xc}[n]$. Applying the variational principle of the second HK theorem to the energy functional of equation 2.9, one minimises that expression and obtains

$$\frac{\delta T_0[n]}{\delta n(\vec{r})} + V_{KS}(\vec{r}) = \mu \tag{2.11}$$

Where $V_{KS}(\vec{r})$ is defined as:

$$V_{KS}(\vec{r}) = \int \frac{n(\vec{r}')}{|\vec{r}-\vec{r}'|}d\vec{r}' + \frac{\delta E_{xc}[n]}{\delta n(\vec{r})} + v_{ext}(\vec{r}) \tag{2.12}$$

and the Lagrange multiplier μ in equation 2.11 enforces the conservation of the total number of particles. Similarly, the variational principle applied to equation 2.9 leads to the Schrödinger equation of the fictitious non-interacting system.

$$\Big[-\frac{1}{2}\nabla^2 + V_{KS}(\vec{r})\Big]\phi_i(\vec{r}) = \varepsilon_i\phi_i(\vec{r}) \tag{2.13}$$

The one particle fictious orbitals ϕ_i can used to construct the electronic density i.e.

$$n(\vec{r}) = \sum_{i}^{N_{occ}} \phi_i^*(\vec{r})\phi_i(\vec{r}) \tag{2.14}$$

The above equations are called the KS equations, the eigenfunctions of these equations are the KS orbitals and the corresponding eigenvalues ε_i are the KS orbital energies. As $V_{KS}(\vec{r})$ is a functional of the density, therefore the equation 2.13 is usually solved in a self-consistent way. However, the eigenvalues and eigenfunctions obtained by solving the KS equation do not have any physical meaning; rather than these are just mathematical expressions to obtain the ground state energy and the charge density of a many-body system. Once the KS equation is solved, various ground state properties of a many-body system are obtained such as forces, equilibrium geometries, stress tensors and phonons dispersion.

2.3 Exchange Correlation Functional

The KS formalism is independent of the approximation used for $E_{xc}[n]$. There are many reasonably good approximations for the functional $E_{xc}[n]$ such as Local Density Approximation (LDA), which assumes the *xc* energy of a real system behaves locally as that of a uniform electron gas. In the LDA approximation the xc functional can be expressed as:

$$E_{xc}^{LDA}[n] = \int \varepsilon_{xc}^{hom}(n(\vec{r}))n(\vec{r})d\vec{r} \tag{2.15}$$

Where $\varepsilon_{xc}^{hom}(n)$ is denoting the *xc* energy per electron of a homogeneous gas with density $n(\vec{r})$. In the limit of homogeneous density or slowly varying density distributions, the LDA is exact. In most realistic cases, LDA works quite well and results obtained with good accuracy in reproducing the experimental structural and vibration properties for covalently bound systems. Usually, LDA overestimates the bonding energies and under estimates the bond lengths. The most important improvement of LDA approximation is the Generalised Gradient Approximation (GGA) which is a semi-local approach and depends on the norm of the gradient of the local electronic density. In its functional form, it is written as:

$$E_{ex}^{GGA}[n] = \int \varepsilon_{xc}^{GGA}(n(\vec{r}), |\nabla n(\vec{r})|)d\vec{r} \tag{2.16}$$

Among the several expressions for GGA approximation, the three most widely used functionals are Becke (B88) [68], Perdew and Wang (PW91) [69] and Perdew, Burke and Enzerhof (PBE) [70]. Compared to LDA, GGA significantly improves the binding energies of real materials.

Generally, these local and semi-local approximations are well suited to compute molecular and crystal structures and their vibrational properties with good accuracy. However, they usually fail to deal with systems where non-local interactions play an essential role, for example in weakly bound molecular systems [71]. One way to tackle the non-local feature of the XC functionals is to use hybrid functionals [72], which in practice are computationally expensive but provide a remarkable improvement on the accuracy of the results at least on energetics. These functionals use a linear combination of a semi-local GGA like functional and a fully non-local Fock-exchange like component. In this thesis we used both the semi local functional (PBE) and hybrid functionals B3LYP [73], CAMB3LYP [74] and WXB79 [75].

2.4 Time Dependent Density Functional Theory (TDDFT)

DFT works quite well to compute the ground-state properties of many electrons systems but strictly speaking, it gives no access to deal with the properties of excited electronic states. In this section, we will review the theoretical background of Time-Dependent Density Functional Theory (TDDFT) which is an extension of ground-state DFT to deal with time-dependent external potentials such as electric and magnetic fields. These time-dependent external perturbations drive away the many-body system from its stationary ground state to high energy excited states. The individual excitations can be computed using TDDFT with linear response theory. The formal foundations of TDDFT date back to the work of Runge and Gross [76]. The Runge-Gross (RG) theorem states that for a given initial state, there is a one-to-one correspondence between time-dependent densities and time-dependent potentials and the time-dependent potential is a unique functional of the time-dependent density and vice versa. As potentials are functionals of densities, therefore the Hamiltonian H(t), wavefunction $\Psi(t)$ and all physical observables become functionals of the time-dependent electronic density.

For N electrons system with coordinates $\vec{r} = (\vec{r}_1 \ldots \vec{r}_N)$ the many body time dependent Schrödinger equation is written as:

$$\iota \frac{\partial}{\partial t} \psi(\vec{r},t) = H(\vec{r},t)\psi(\vec{r},t) \tag{2.17}$$

Similar to DFT theory a time-dependent version of Kohn-Sham's ansatz is also applied for TDDFT i.e the exact density of the N electron system can be obtained by solving a set of fictitious single particle time-dependent Schrödinger equations:

$$\imath \frac{\partial}{\partial t}\phi_i(\vec{r},t) = \Big[-\frac{1}{2}\nabla^2 + V_{KS}(\vec{r},t) \Big] \phi_i(\vec{r},t) \tag{2.18}$$

Equation 2.18 is called the "time-dependent KS equation" and time-dependent density is obtained by

$$n(\vec{r},t) = 2\sum_{i}^{N_{occ}} \phi_i^*(\vec{r},t)\phi_i(\vec{r},t) \tag{2.19}$$

Where N_{occ} are the number of occupied states. TDDFT written in the time domain does not give direct access to excitation energies. To assess this information, one needs to write TDDFT using linear response theory. Optical absorption spectra, which is the object of the majority of TDDFT applications are computed in the linear response regime and can be compared to the spectroscopic experiments.

2.5 Path Integral Molecular Dynamics (PIMD)

In most of the atomistic simulations, the nuclei are treated as classical point particles, following the Boltzmann statistic and their time evaluation is monitored by Hamilton's equations. For systems containing light nuclei such as hydrogen-bonded systems, this approximation is quite poor as light hydrogen nuclei deviate significantly from their classical behaviour even at room temperature and above. In such situations, the comparison between thermal energy K_BT and the quantum of harmonic energy $\hbar\omega$, at given temperature T should be considered. If $\frac{\hbar\omega}{K_BT} >> 1$ then inclusion of the nuclear quantum effects is essential. There are various such situations where the physical observable measured experimentally deviates significantly from its classical behaviour. For example, the deviation of the heat capacity of substances from a classical value of 3 K_BT per atom. Non-Arrhenius behaviour of reaction rates at low temperature, equilibrium Isotopes effects and deviation of the kinetic energy distribution of light atomic nuclei from Maxwell-Boltzmann distribution measured in neutron scattering experiments.

The inclusion of the NQE in current state of the art atomistic simulations methods is done by means of path integral approach to quantum mechanics which was originally introduced by Richard Feynman [77, 78]. In this formulation, the physical quantities are expressed in terms of the exponential averages of an action integral over all the possible paths joining the two points in phase space. The imaginary time path integral form of quantum mechanical partition function $Z = Tre^{-\beta H}$ in terms of inverse temperature $\beta = \frac{1}{K_BT}$ is written as

$$Z = \oint D[q(\tau)] e^{-\frac{1}{\hbar}\int_0^\beta [\frac{1}{2}m\dot{q}(\tau)+V(q(\tau))]d\tau} \tag{2.20}$$

Where $\oint D[q(\tau)]$ define as a functional integral over all the possible closed paths connecting the two points in the configurational space and $H(q(\tau)) = \frac{1}{2}m\dot{q}(\tau) + V(q(\tau))$ is the Hamiltonian of the quantum system. The practical implementation of this approach to computing the experimental observable with NQEs requires a series of practical steps: The first is to write the partition function in position basis as these are the eigenstates of the potential energy operator $e^{-\beta\hat{V}}|q\rangle = e^{-\beta V(q)}|q\rangle$

$$Z = \int dq_1 \langle q_1|e^{-\beta\hat{H}}|q_1\rangle \tag{2.21}$$

As the Hamiltonian is sum of both kinetic and potential energy operators which do not commute, therefore the splitting of $e^{-\beta[\hat{T}+\hat{V}]} = e^{-\beta\hat{T}}e^{-\beta\hat{V}}$ is not possible. However for small $\beta\hat{H}$, the error doing this decomposition will be small, i.e

$$e^{-\beta\hat{H}} = \left(e^{-\beta\hat{H}/P}\right)^P \approx \left(e^{-\beta_p\hat{V}/2}e^{-\beta_p\hat{T}}e^{-\beta_p\hat{V}/2}\right)^P + \mathscr{O}(\beta_p^2) \tag{2.22}$$

This above expression is exact in the limit $P \to \infty$. The error in the Trotter decomposition is of order $(\beta_p)^2$. With this approximation, and by adding P-1 closure identities of position basis one lead to the discreet version of the partition function after performing some algebra

$$Z_P = (m/2\pi\hbar^2\beta_P)^2 \int dq_1 \ldots dq_P e^{-\beta_P\sum_{i=1}^P [V(q_i)+\frac{1}{2}m\omega_P^2(q_i-q_{i+1})]} \tag{2.23}$$

where $\omega_P = \frac{1}{\beta_P\hbar}$ is spring constant. Equation 2.23 represents the classical partition function of a cyclic polymer (Ring polymer) of P atoms connected through the harmonic springs to their nearest neighbours. The discrete equivalent of $\oint D[q(\tau)]$ of Feynman path integral approach are now the multiple integrals over q_j of ring polymer partition function. This isomorphism motivates in practice referring a single particle to ring polymer which is a set of its replicas name as beads. With this isomorphism established between ring polymer partition function and the quantum partition function of distinguishable nuclei, one can now compute the experimental observables with NQEs, but only those depends sole on atomic coordinates such as potential energy, radial distribution function, bond length and stable molecular configurations. As all the replica are identical, one can estimate the average value of an observable $\langle A\rangle_P$ taken over all the beads.

The sampling of Boltzmann distribution which include now momenta by integrating the Hamilton equations in practice, one can equivalently write the partition function with inclusion of momentum basis as

$$Z_{QMP} = (\frac{1}{(2\pi\hbar)})^P \int dp_1 \dots dp_P \int dq_1 \dots dq_P \, e^{-\beta_P \sum_{i=1}^{P} [V(q_i) + p_i^2/2m] + \frac{1}{2} m\omega_P^2 (q_i - q_{i+1})^2} \quad (2.24)$$

Using equation 2.23 or equation 2.24 the exact quantum partition function is reproduced in $P \to \infty$ limit. It has been shown that using PIMD, at least 32 number of beads are required to converge the structural properties [79, 80]. However, recent developments improve significantly the efficiency of path integral simulation. The important developments are based on using sophisticated thermostats and allowed PIMD simulation to converge with few number of beads [81, 82].

Chapter 3

Non-aromatic intrinsic fluorescence in single amino acid glutamine aggregates

3.1 Introduction

Short peptides void of any aromatic residues have recently been shown to display an intrinsic fluorescence in the visible range [83, 53]. This has primarily been observed in peptide structures linked to neurodegenerative diseases, such as Alzheimer's, Parkinson's and Huntington's diseases [54]. Furthermore, optical properties of double amino acid based nanowires have also been reported, existing either of two non-aromatic or two aromatic amino acids [84, 85]. In our group, it has been recently shown that the fluorescence in crystal structures of the amyloid beta protein is correlated with the presence of short hydrogen bonds (SHB), in the absence of any aromaticity [57]. The SHB permits proton transfer leading to a double-well ground state potential, which was proposed, prevents conical intersection in the excited state and may thus promote the red shift of the exciton transitions. Indeed, it has been suggested that one of the prerequisites for this fluorescence/photoluminescence observed in either amyloid structures or short peptide nanowires is related to hydrogen bonding or aromatic interlocks which, for the latter, decreases the bandgaps down to the semi conductive regions. Thus, these new optical nanowires may pave the way for environmentally clean optical materials for photonic short wavelength devices. Despite the previous suggestions that proton delocalisation is strongly coupled to this intrinsic fluorescence, the generality of this result and more importantly, the role of vibrational modes upon excitation in non-aromatic systems, has not been elucidated. We have thus searched for a model system, such as a single amino acid-based structure that displays similar optical properties to amyloids as well as allowing for more sophisticated computational approaches. We have been inspired by the

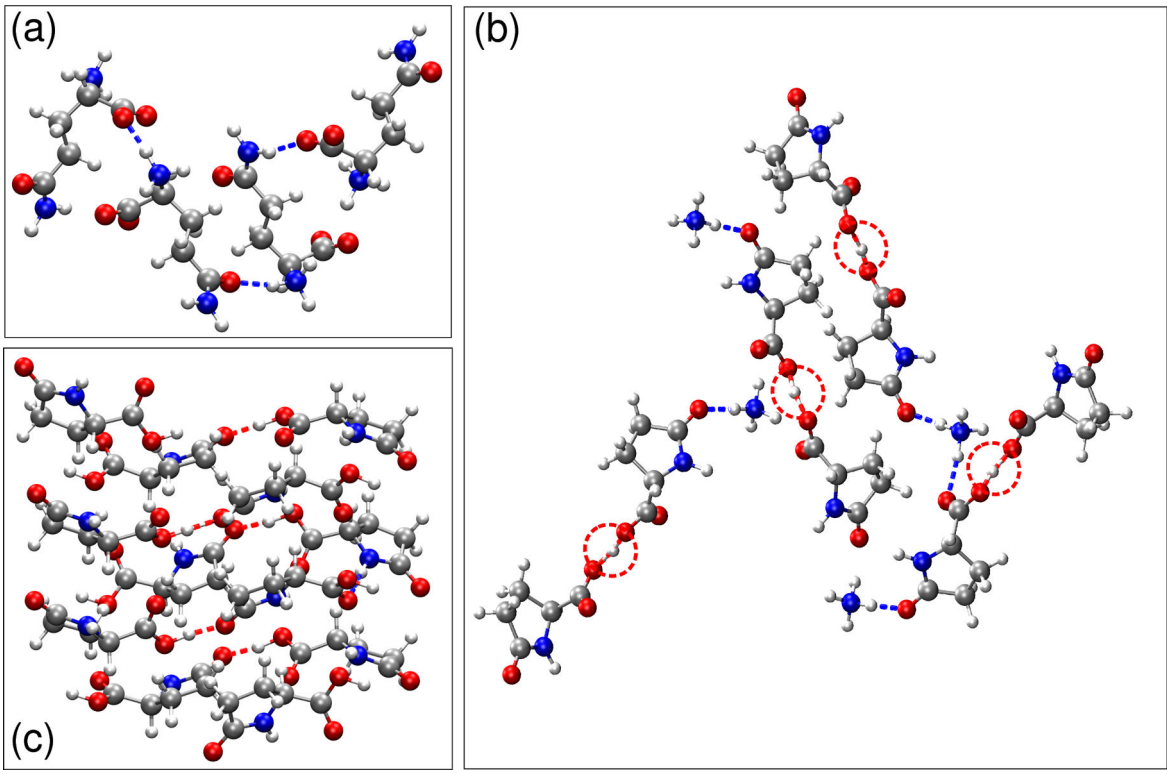

Fig. 3.1 a) L-glutamine crystal structure [5] with four glutamine residues in the unit cell connected through hydrogen bonds shown in blue dashed lines. b) L-pyro-amm crystal structure involves a short hydrogen bonded anionic dimer with an ammonium counterion. The short hydrogen bonds (SHB's) are highlighted by red circles while the hydrogen bonds involving $NH4^{+}$ ions are shown in blue dashed lines and finally c) L-pyroglutamine [6] where the hydrogen bond is colored in red

small peptide nanostructures that have been pioneered by the Gazit laboratory and by the fact that there are several neurodegenerative diseases that have been connected with an increased level of glutamines produced as part of a protein as for example Huntingtin in Huntington's disease, which renders the protein more aggregation prone.

It has been known that the amide group in L-glutamine (L-glu) is uniquely labile and thus can rapidly hydrolyse. Our experimental collaborators in Cambridge, observed that the single amino acid L-glu upon incubation at 65°C in water can form a nanostructural material with optical properties similar to the ones observed in other amyloid proteins such as in amyloid beta, alpha- synuclein or Tau [54, 55, 86]. Using the X-ray diffraction (XRD), they showed that L-glu dissolved in water and becomes cyclysed forming a previously unreported structure which resembles L-pyroglutamine (which has been reported to be a component of amyloid-beta in the brain [87], but involves a low-barrier hydrogen bonded anionic dimer with an ammonium counterion. We have termed the new structure, i.e. Lpyroglutamine

complexed with an ammonium ion, L-pyro-amm. L-pyro-amm has a crystalline morphology as shown by scanning electron microscopy (SEM). The newly formed solid was further characterised using terahertz time-domain spectroscopy (THz-TDS), which provides valuable information on the low-frequency modes in the crystal that control the proton transfer. Additionally, the experiments were interpreted using ground and excited state electronic structure calculations and molecular dynamics simulations. Ultimately, the combination of static structural information, atomic vibrational dynamics and optical properties enable the origins of fluorescence in this particular structure to be elucidated, shedding light on the complementary processes in more complex systems.

3.2 Computational Methods

The work presented in this chapter combines various experimental and computational spectroscopy methods to shed light on the origins of intrinsic fluorescence of L-glutamine crystals. The details of the experimental methods are given in appendix. A. The computational part of this work is presented in details below.

The structures obtained from the experiments were first geometrically optimized at 0 K using the Broyden-Fletcher-Goldfarb-Shanno (BFGS) [88] minimization algorithm implemented in CP2K package [89]. A convergence criterion for the wave function optimization was used as $5x10^{-7}$ a.u. Applying the method of the Gaussian and plane wave, the wave function was expended in the Gaussian double-zeta valence polarized (DZVP) basis set. The cutoff for the electronic density was set to 300 Ry. We used the gradient correction to the local density approximation and the core electrons were treated via Goedecker-Teter-Hutters pseudopotentials [90]. In all the calculations, we used the Becke-Lee-Yang-Parr(BLYP) [68] functional with the D3(0) Grimme dispersion corrections for the van der Waals interactions [91]. For the ground state, ab initio Molecular Dynamics simulations (AIMD) were performed using Quickstep algorithm implemented in CP2K. In these calculations, the propagation of the nuclei were taken into account within the framework of the Born-Oppenheimer approximation. The simulations were performed in NVT ensemble and the temperature was controlled during the simulations by using the velocity-rescaling thermostat [92]. We used the time step of 0.5 femtosecond to update the nuclear coordinates and velocities while the total length of the simulations for each system is 50 picoseconds. The calculations of the excited state were performed within the framework of TDDFT using the Liouville-Lanczos formalism implemented in freely available Quantum-Espresso package [93]. In this approach the optical spectra is obtained directly over the wide spectral range without taking into account the numerically complex calculations of the single excited states. The details of this method have

been presented elsewhere [94, 95]. We used plane wave basis set and the electron-ion interactions were taken into account via norm conserving Martins-Troullier pseudopotentials [96]. To determine the ground state wave function, we used the gamma point of the Brillouin zone. All the periodic calculations employed the computationally demanding B3LYP hybrid functional, the kinetic energy cutoff of 40 Ry was used for the wave functions. The intrinsic band width for the spectra was set to 0.003 Ry (0.0408 eV). TDDFT simulations of the small clusters extracted from the periodic structures were performed using hybrid functional with varying fraction of exact exchange (CAMB3LYP [74] and WB97X [75]). We use the GAUSSIAN 16 code [97] for performing all-electron calculations using the 6-311++G** (d,p) basis set. The optical properties of pyroglutamic acid were investigated using various isolated cluster models with the Gaussian16 software package. The clusters were extracted directly from the crystal structure and used in various combinations (dimers, trimers, tetramers) to perform time-dependent DFT (TD-DFT) calculations. Split-valence triple-zeta 6-311g (2d,2p) basis set for all atom types and was combined with the hybrid B3LYP functional.

3.3 Results and Discussion

It has long been known that poly-glutamine can form amyloid like fibrillar structures in vitro. The more glutamine forming part of the poly-glutamine polymer, the faster the aggregation propensity of the polypeptide chain. This led us to investigate whether L-glu on its own, under certain conditions which normally promote fibril formation such as an increase in temperature [98] was able to form structures with similar optical properties than recently observed for amyloid fibrils [57]. In order to investigate whether L-glu has changed its crystal structure upon incubation at 65°C over time, XRD analysis is performed in Cambridge of the resulting material. In panel (b) of the Fig. 3.1 the crystal structure of the heated L-glu structure is shown, which we termed L-pyro-amm, and the published crystal structures of L-glu and L-pyroglutamine (L-pyro) are shown in panel (a) and (c) respectively. Note, the L-pyro structure was analysed as it displayed structural similarities to the newly formed L-pyro-amm. Images were obtained from geometry optimisations using experimental densities. L-pyro-amm consists of 8 pyroglutamine groups and four ammonium ions (144 atoms) complexed within the crystal (see Fig. 3.1b). In contrast, L-glu consists of 4 glutamine molecules (80 atoms) in the unit cell which form hydrogen bonds involving the termini and side chain. Furthermore, L-pyro consists of 12 pyroglutamine molecules (192 atoms) in the unit cell forming hydrogen bonds involving the NH and COOH groups. L-pyro-amm has a rather unique hydrogen bond network structure since four of the pyroglutamine molecules are deprotonated and hence have a nominal negative charge, while the other four molecules

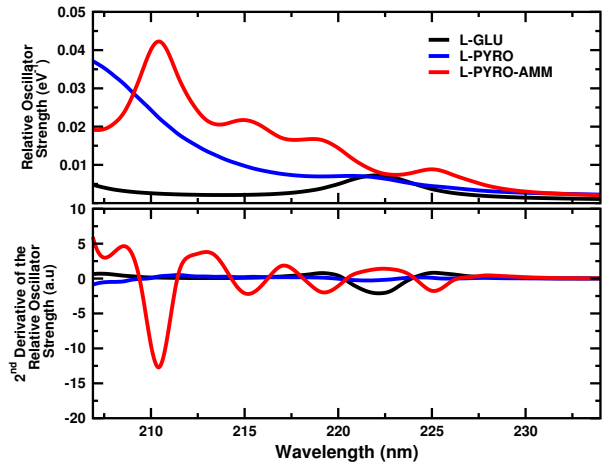

Fig. 3.2 Absorption strength computed for the 0 K structures. The upper panel illustrates the absorption spectra obtained from the TDDFT calculation on three periodic systems while lower panel shows the second derivative of the oscillator strength in order to see the peaks more clearly.

are neutral. One of the important implications of this difference is that L-pyro-amm consists of a very strong hydrogen bond. The red circled region in Fig. 3.1b corresponds to a short hydrogen bond (SHB) with a length of 2.45 Å, while those in L-glu and L-pyro range between 2.55-2.85 Å (see red and blue coloured regions in panel b) and c) of Fig. 3.1)

3.3.1 Absorption Spectra of Glutamine Aggregates

We first investigated whether there were any differences in the optical properties associated with the three crystal structures. Comparing the absorption of the dried powder of L-glu, L-pyro and L-pyro-amm we show that only L-pyro-amm has a significantly red-shifted absorption which lies in the 275-320 nm range, whereas both L-glu and L-pyro primarily absorb in the deep UV $<$ 250 nm (see Fig. 3.2). We next compared the experimental absorption spectra of L-glu, L-pyro and L-pyro-amm with the ones obtained from time dependent density functional theory (TDDFT). We highlight here, that the small size of the systems allowed for the spectra to be determined using the B3LYP hybrid functional significantly advancing the quality of our theoretical predictions in previous studies [57]. Besides the calculations for the periodic systems, we also performed some benchmarks of clusters built from the three systems using long-range corrected hybrid functionals. Fig. 3.2 illustrates the absorption spectra obtained for the TDDFT calculations on the 3 periodic systems in the ground state (i.e. at 0 K). The top panel shows the relative oscillator strength as a function of the frequency while the bottom panel illustrates the second derivative of

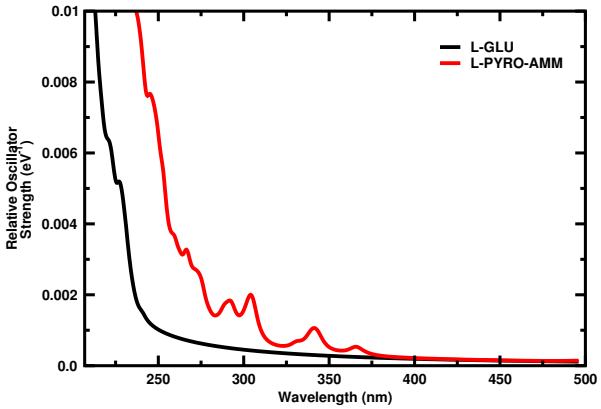

Fig. 3.3 Average thermal spectra over 25 different geometries taken randomly from BOMD simulations. Compare to 0 K, for L-pyro-amm systems, thermal fluctuations cause huge red shift of 2 eV while for L-glutamine the trends remains the same as at 0 K

the oscillator strength allowing for the positions of the maxima in the spectra to be more easily identified. The spectra reveal some striking differences between the different systems. Interestingly, we observe that L-pyro is essentially dark up to an excitation energy of 5.75 eV (216 nm). On the other hand, L-pyro-amm shows the presence of more structure in the spectra. Specifically, it is the only system where the spectra feature a low energy excitation at ∼5.5 eV (225 nm) and subsequently other peaks slightly above 5.625eV (220 nm) and 5.75eV (216 nm). While L-glu exhibits a peak at ∼5.58eV (222 nm), it is dark up to ∼6eV (206 nm). We have previously shown that thermal fluctuations have a large impact on the absorption spectra of peptide structures compared to absorption spectra at 0 K [57]. In Fig. 3.3 we show that, compared to the 0 K spectra, thermal fluctuations cause a large red shift to around 3.4 eV (365 nm) for L-pyro-amm, similar to what is observed experimentally. Importantly, no such effect is observed for L-glu which remains dark up to more than 5 eV (247 nm) as seen at 0 K. Similar to our previous studies on the intrinsic fluorescence of amyloid- beta, absorption appears to be closely related to structures containing SHB, as neither L-glu, nor L-pyro display a significantly red shifted absorption. Furthermore, the data present that the cyclisation of L-glu to L-pyro-amm does not significantly contribute to the optical properties observed in L-pyro-amm since L-pyro on its own, which is identical to L-pyro-amm but lacks the complexed ammonium ions, does not exhibit absorption at low energies. In order to understand better the physical origin of the low energy excitation at ∼5.5 eV (226 nm) in L-pyro-amm, we computed the electron response density at this frequency. This is illustrated in Fig. 3.4, where we observe that most of the electron response involves regions around the pyroglutamine rings as well as regions near the SHB. The optical response thus involves a collective charge reorganization involving several parts

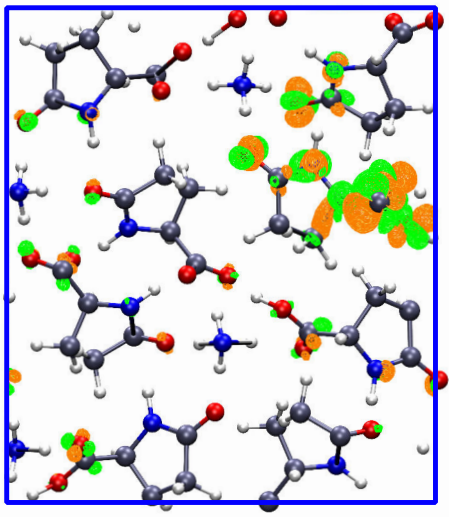

Fig. 3.4 The electronic response density calculated at the first excitation peak around 226 nm is plotted for L-pyro-amm structure. The orange and green colours correspond to positive and negative values of the response densities, the iso-value for the response density was set $5x10^{-3}$

of the molecular crystal. We next investigated whether the above structures also display fluorescence excitation and emission properties as has been observed for amyloid -like structures reported previously [57]. Experiments shows that the excitation scan ranging from 250-400 nm with the emission set at 430 nm of L-glu in water at day 0 to 8 after incubation at 65°C. Interestingly, the excitation peak observed around 360 nm which is similar to what have been measured previously for amyloid proteins [57]. The corresponding emission scan with excitation at 360 nm and emission from 380-560 nm showed an emission peak around 430 nm, again lying in the same visible range as for amyloid proteins. When the L-pyro-amm solution was dried the excitation and emission peaks were slightly blue shifted. Furthermore, an emission peak of 430 nm was observed when measuring photoluminescence of L-pyro-amm. Importantly, experiments do not see any fluorescence in L-glu. To determine the importance of the ammonium ion experimentally, L-pyro was incubated in water and heated at 65°C for 8 days, and no intrinsic fluorescence was observed. Pinpointing the exact mechanisms and origins of the difference in the optical properties between the three systems from the ground state calculations at 0°K can only be indirect. As eluded to earlier, one of the factors that distinguishes L-pyro-amm from the other systems is the presence of the SHB (highlighted by red circles in Fig. 1.1) and the presence of the ammonium ion. In order to characterise the behaviour of the SHB we conducted *ab initio* molecular dynamics simulations of the three systems and examined the proton transfer coordinates defined as

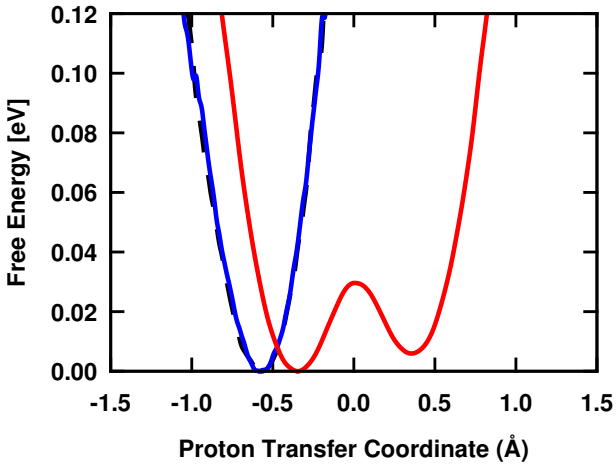

Fig. 3.5 The estimated free energy as a function of proton transfer coordinate (PTC) is plotted for the three systems. L-glu (black dashed line) and L-PYRO (blue line) are characterized by single well while L-pyro-amm exhibits asymmetric double well character with barrier height $\sim 30\,meV$

the difference in distance between the proton and the two oxygen atoms that sandwich it as shown in Fig. 3.5 for the different types of hydrogen bonds in the crystals. It is clear that the short hydrogen bond in L-pyro-amm is characterised by a double-well potential implying that proton transfer events are triggered by thermal fluctuations. The barrier associated with this proton transfer is on the order of thermal energy indicating that zero- point energy (ZPE) proton transfer would become barrierless [99]. We will see in chapter the role of nuclear quantum motion on barrier height and hydrogen bond symmetrisation. An examination of similar proton transfer coordinates for hydrogen bonds in L-glu and L-pyro show that they are characterised by only single-well potentials.

3.3.2 Environment Effect on Optical Spectra

The nature of the optical properties is sensitive to the environment in which the glutamine molecules reside. It has previously been reported that charged amino acids already display an absorption in the range of 250-350 nm that is significantly red shifted [100, 57, 53]. The origins of the low energy absorption were attributed to charge transfer excitations. The simulations of these systems were performed in the gas phase, rather than considering the protein environment such as shown for L-pyro-amm in Fig. 3.3. In order to investigate the role of the protein environment on the electronic excitations we performed a couple of simulations and experiments. Using a series of molecular clusters of varying size and configuration that were extracted from the crystal structure, we computed the optical absorption. In comparison to the results presented in Fig. 3.2, the calculation of the small clusters of L-pyro-amm in a

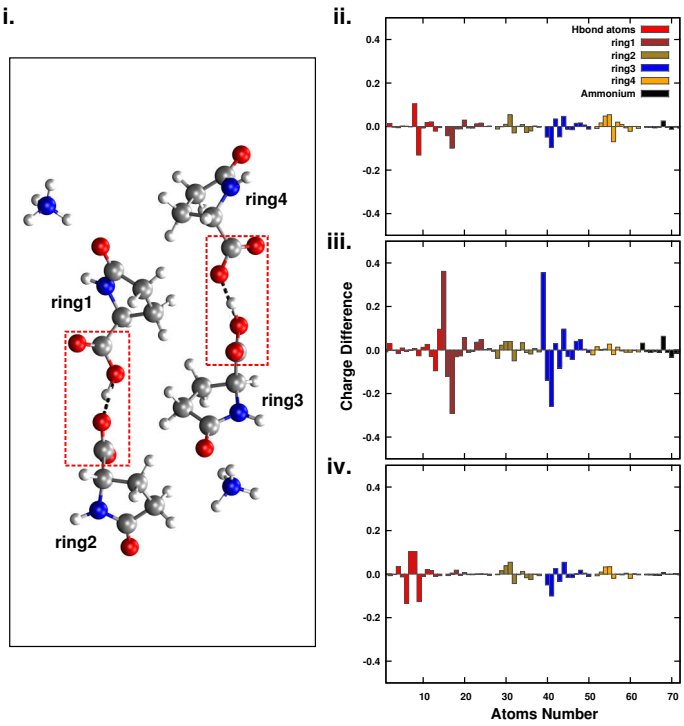

Fig. 3.6 Panel i) showing a snapshot of the molecular cluster highlighting the different part in the structure such as SHB region (dashed red rectangles). RESP charges were extracted for the ground state and the first three excited states. These exited states are very close in energy therefore we take the average of their charges and calculate the differences from the ground state charges. Panel ii) illustrating the average charge difference of the L-Pyro-amm cluster of 72 atoms extracted from the periodic crystal. Panel iii) shows the average charge difference of the cluster as function of protons motion along the SHB. Panel iV) illustrate the average charge difference for the cluster where the short H-bond length (the O-O distance) is altered from 2.45 to 3.2 Å.

continuum dielectric media resembling a protein environment also shows that the excitation being a charge reorganisation involving several different molecular groups of the crystal (see Fig. 3.6). The effect of the dielectric environment on the optical properties can be seen very clearly by examining how different non-polar solvents affect the absorption properties of L-pyro-amm. This was performed by changing the solvent from water to benzene and thus from a high dielectric medium to a low dielectric medium (Fig. 3.7). In order to address the role of the solvent and the protein environment experimentally we performed several experiments. We first determined the effect of the protein solvent on the fluorescence excitation and emission spectrum by measuring them in the presence or absence of water shows that the presence of water leads to red shifted peak maximum of the excitation and emission spectra.

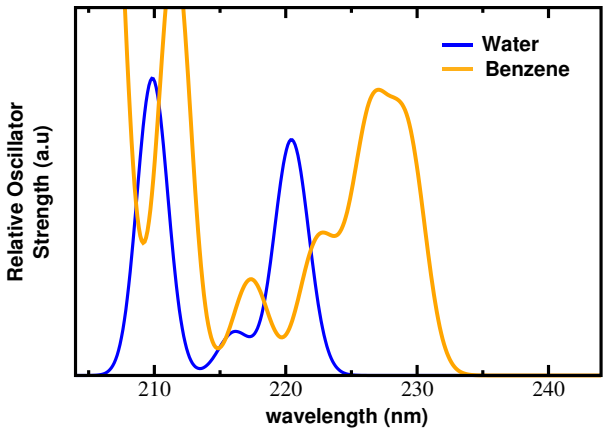

Fig. 3.7 The absorption spectra of small L-Pyro-amm cluster is calculated by using different solvents. As one go from very highly dielectric medium say water to very low like Benzen, the absorption spectra significantly red shifted.

We next investigated to which extent different non-polar solvents would affect the absorption properties of L-pyro-amm by changing the solvent from water to acetonitrile and finally to benzene and thus from a high dielectric medium to a low dielectric medium. As shown in Fig. 3.7, the direct local environment has a significant effect on the absorption of L-pyro-amm, with increasingly non-polar solvents leading to a significant red shift of the absorption spectrum. These observations suggest that the local protein environment significantly contributes to the optical properties of L-pyro-amm.

We have observed previously that the solvent and the direct protein environment is crucial for the optical properties observed [57]. We show here that non polar solvents quench the optical signal less than polar solvents such as water. This is a common feature of certain environmentally sensitive fluorophores [41]. Similarly, increasing the protein concentration leads to increased red shift in the absorption of L-pyro-amm. The latter is comparable to amyloid systems studied previously. The more aggregated the structure, the more red-shifted the fluorescence measured.

3.3.3 Excited State Optimization

Up to this point, we have shown that the vibrations of protons along SHBs are an important part of the structural fluctuations in the ground state structure of L-pyro-amm. In a final set of theoretical studies to ascertain the role of proton transfer in the ground state, as well as to elucidate the presence of other types of vibrational modes, we performed a series of geometry optimisations on the first excited state of the three glutamine systems: L-glu, Lpyro

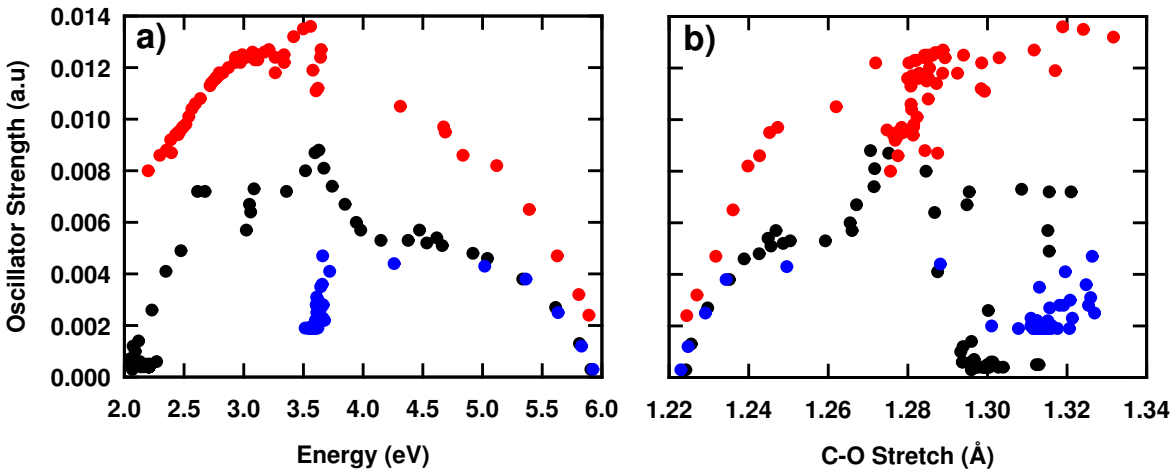

Fig. 3.8 a) The oscillator strength during the optimization of first excited state is plotted vs energy $(E_{excited} - E_{ground})$ for three systems simulated dielectric environment of water. The oscillator strength of L-pyro-amm is greater then L-glu and L-pyro. b) The oscillator strength is plotted vs the active C-O stretch for three systems. L-pyro-amm remains the brightest.

and L-pyro-amm. All the three clusters were immersed in a continuum dielectric constant of 80 corresponding to that of water.

Fig. 3.9 shows the molecular cluster for L-pyro-amm before and after relaxation on the excited state. One of the major structural changes that occurs upon excitation is an increase in the C=O bond length by ~ 0.1 Å. These changes are visually depicted in the inset of Fig. 3.9. Interestingly, we observe very similar structural changes in all the three systems. In Fig. 3.8, the oscillator strength during the optimization of first excited state is plotted vs energy $(E_{excited} - E_{ground})$ for three systems simulated in dielectric environment of water. The oscillator strength of L-pyro-amm is greater than L-glu and L-pyro. The panel b) shows the oscillator strength plotted vs the C-O stretch for the three systems and it is clear that the L-pyro-amm remains the brightest among all.

The evolution of the excited and ground state energies over the course of these events is also shown in left of the panel a) and b) of Fig. 3.9 where the effective emission energy decreases from 210 to 450 nm. Although all three glutamine structures display similar trends on the excited state, L-pyro-amm with the SHB is distinct in its character. It displays the largest oscillator strength indicating that it is the brightest structure and hence more likely to fluorescent which is consistent with our experimental findings. Furthermore, the fate of how the bright or darkness of L-pyro-amm on the first excited state is sensitive to the initial conditions of the proton vibrations. The panel b) of Fig. 3.9 shows that transferring the protons on the ground-state (see the black rectangular regions), significantly reduces the oscillator strengths across the entire relaxation process on the first excited state. Thus,

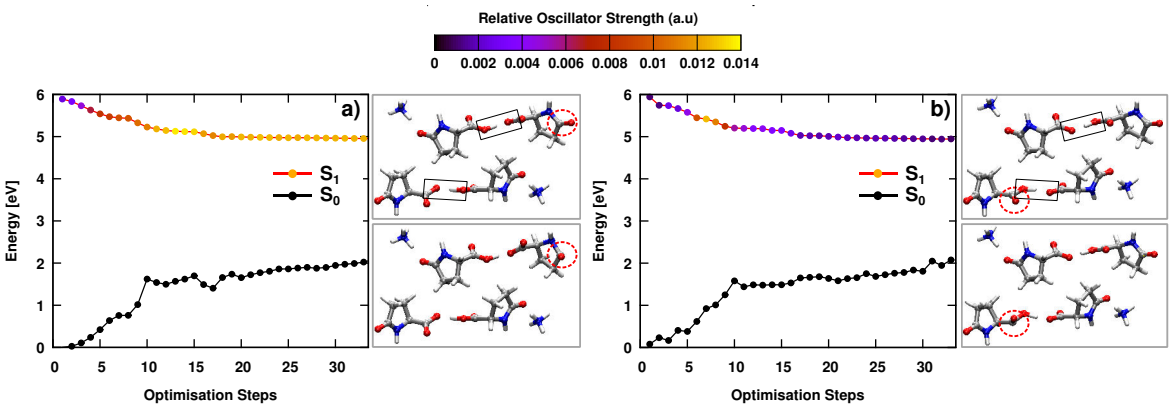

Fig. 3.9 Panel a), The ground state (S_0) and excited state (S_1) energies are plotted as function of geometry relaxation steps of 1^{st} excited state. On the left of panel a) molecular cluster for L-pyro-amm is shown before and after relaxation on the excited state. The red dashed circles showing the changes in $C = O$ vibrational modes. Panel b) illustrate the same, but showing the geometries with proton transfer at the ground state.

we conclude that the optical properties of the glutamine crystals are sensitively tuned by collective vibrational modes.

Chapter 4

Proton Delocalization in Glutamine Aggregates, A Classical Versus Quantum Picture

4.1 Introduction

Proton transfer (PT) along the hydrogen bonds plays a vital role in numerous physical and chemical process [101], such as in enzymatic reactions of biological systems [102], acid-base chemistry of water, changing the pH and pK_a's of the amino acids [103–105] and altering the chemistry of protonated biological ions [106]. The molecular mechanism associated with proton delocalisation through hydrogen bond in biological matter, particularly in proteins, is poorly understood. In these systems, the hydrogen bond network is complex as it involves interactions between different chemical groups with different spatial orientations within the structure. In proteins it has been often proposed that the PT reactions are associated with strong hydrogen bonds of length 2.5 to 2.7 Å [102, 107, 108]. In the previous chapter, we also observe similar trends for the case of L-pyro-amm system. The proton transfer in this system is specific to a very short hydrogen bond (SHB) of the average hydrogen bond length of $\sim 2.5 \pm 0.076$ Å. For all other glutamine systems, where the average hydrogen bond length is longer than $\sim$2.7 Å, proton transfer has not been observed (see Fig. 3.5 of the previous chapter).

However, all these results presented so far describing the structure and dynamics of hydrogen bonds are based on classical simulations, where the protons were treated classically. Due to their light mass, the quantum nature of protons such as zero-point energy (ZPE) and

tunnelling can play an essential role in determining the correct structure and dynamics of hydrogen bonds. Numerous previous studies illustrate the importance of quantum motion of proton involved in hydrogen bonds in different systems such as liquid water [109, 79, 110–112], high pressure phases of ice [99, 113], hydrogen chloride hydrates [114], proton sponges [115, 116], water-filled carbon nano tubes [117], liquid vapour interfaces [118] and proteins [102, 108]. As seen in the previous chapter, the short hydrogen bond in L-pyro-amm system is characterised by a double-well potential with barrier height about $\sim$30 meV. The barrier is much smaller compared to the zero-point energy (ZPE) of a typical O-H bond which is in the order of $\sim$ 0.2 eV. Therefore the quantum effects will make the short hydrogen bond barrierless. The barrierless hydrogen bonds have long been observed and studied in high-pressure ice phases [99]. In ice under high pressure, it has been found that by compressing the hydrogen bond to a shorter length of $\sim$2.4 Å, the zero-point fluctuations lead strongly delocalised proton and hydrogen bond symmetrisation [99]. Also, McKenzie and coworkers [119] investigate the effect of quantum nuclear motion on short hydrogen bonds by using two-state diabatic model. They show that going from moderate to short hydrogen bonds quantum effects completely flatten the potential energy barriers.
In this chapter, we will investigate in detail how NQE modulate the structural and electronic features of different hydrogen bonds in L-glutamine aggregates. Mainly we focus on the SHB of L-pyro-amm system.

4.2 Computational Methods

Finite temperature ground state *ab initio* molecular dynamics simulations were performed to assess the thermodynamics and structure of the hydrogen bond network in L-glutamine systems. The details of these simulations are given in the previous Chapter 3. To investigate the role of the NQE on structural and electronic properties of the hydrogen bond network, we performed the path integral molecular dynamics simulation. In these simulations, each classical particle in its quantum representation is replaced by N replicas (beads). All beads connected through harmonic springs. The computational cost to perform such simulations increase N times compared to the classical one. For efficient sampling, we combine path integrals with Langevin thermostat (PIGLET) [120], which permits the usage of a small number of beads. For All PIGLET simulations, we used six beads which have been shown to give good convergence for various statistical properties in liquid water [111]. The production runs of classical and quantum simulations for each system were 50 ps and $\sim$ 9 ps respectively.

4.3 Results and Discussion

Our results are broadly divided into the classical (AIMD) and quantum (PIMD) analysis of the hydrogen bonds network of L-glutamine systems (L-glu and L-pyro-amm). In Section 4.3.1, we will discuss the thermodynamics of the hydrogen bond network and the role of NQE in L-glu system. Section 4.3.2 is dedicated to discussing the free energy analysis of proton transfer coordinate in the L-pyro-amm system and the effect of nuclear quantum motion on symmetrisation of the SHB. In Section 4.3.2, the role of NQE on the structural correlation between proton transfer coordinate and oscillations of the nearby ammonium ions is discussed. The electronic properties of the hydrogen bonds are investigated in Section 4.3.4 by using the maximally localized Wannier's functions [121–124]. Finally in Section 4.4. we conclude and briefly summarise our results.

4.3.1 Hydrogen Bonding in L-glu

In the following, we will focus on the hydrogen bond patterns observed in L-glu crystals. In the previous chapter, we have seen that, compared to L-pyro-amm, L-glu show week optical properties. The optical features of this system were shown insensitive to the temperature effects. The central difference between the structure of the two systems is reflected from their hydrogen bond network. In comparison to L-pyro-amm, the hydrogen bond network in L-glu rather have a simple structure. In the proceeding sections, we will discuss this difference in detail by investigating the structural, dynamical and electronic properties of different hydrogen bonds of the two systems. The leftmost panels of Fig. 4.1 shows the snapshots of L-glu structure taken from classical (top) and six beads quantum (bottom) simulations. The hydrogen bonds in this system labelled as a, b and c are highlighted in blue dashed lines. From finite temperature *ab initio* molecular dynamics simulations, we investigate the structure and dynamics of these hydrogen bonds and also the role of NQE is studied in detail. The right panels of Fig. 4.1 are illustrating the corresponding free energy profile as a function of PTC(r) and the heavy atoms compression coordinate defined as $R = d_{X-H} + d_{H-X}$ for each hydrogen bond, where d_{X-H} and d_{H-X} denotes the distance between proton (H) with donor and acceptor atoms (X) respectively. The top and bottom three panels are showing the results from classical and quantum simulations, respectively. From our classical simulation we find that the average bond lengths of three hydrogen bonds to be 2.68 ± 0.09 Å for HB a, 2.88 ± 0.11 Å for HB b and 2.88 ± 0.12 Å for HB c. It is clear from the figure that the free energy profile of PTC is classically characterised by narrow single well potential. No proton transfer has been observed among all the hydrogen bonds. In quantum simulations, the distribution becomes fatter and proton delocalisation is observed

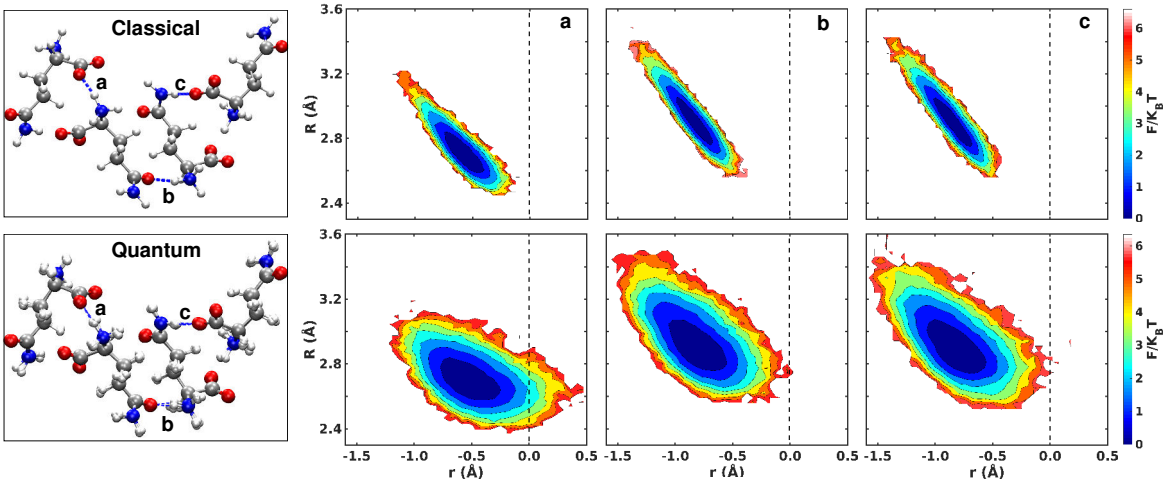

Fig. 4.1 The leftmost panel showing the snapshots taken from classical (top) and six beads quantum (bottom) simulations of L-glu crystal. The hydrogen bonds of the systems label as a, b and c are shown in the blue dashed lines involving the termini and side-chain groups. The right panels illustrating the corresponding free energy profile as a function of PTC define as $r = d_{X-H} - d_{H-X}$ and heavy atoms compression coordinate defined as $R = d_{X-H} + d_{H-X}$, for each hydrogen bond obtained from classical (top) and quantum (bottom) simulations.

only along the short hydrogen bond HB a as seen from the positive value of PTC. While for the other two cases, there are no such events. Xin-Zheng Li and coworkers [125] showed for a variety of hydrogen bonds in different systems, the NQE weakens the weak hydrogen bonds but relatively strengthens the strong hydrogen bonds. For the short hydrogen bond, we also observed similar trends. Fig. 4.2 illustrates the heavy atoms distance distribution computed from classical (black) and quantum (red) simulations. It is clear from the figure that for short hydrogen bond (solid line), the heavy atom distance squeezes towards left by turning on the quantum effects. However, in case of other hydrogen bonds this effect was absent (HB b and c). The heavy atom distance distribution for HB c is plotted in dashed lines. On the hydrogen bonding of L-glu system, we conclude that NQE's strengthens the short hydrogen bond and proton delocalization, while the rest of the two hydrogen bonds do not show this behaviour.

4.3.2 Proton Delocalization and Hydrogen Bond symmetrization in L-pyro-amm

As discussed earlier, the critical feature in the hydrogen bond structure of L-pyro-amm is the presence of a very short hydrogen bond of an average length of 2.5 Å. Panel a) of Fig. 4.3 illustrates the zoomed snapshot of the L-pyro-amm system showing the hydrogen bond

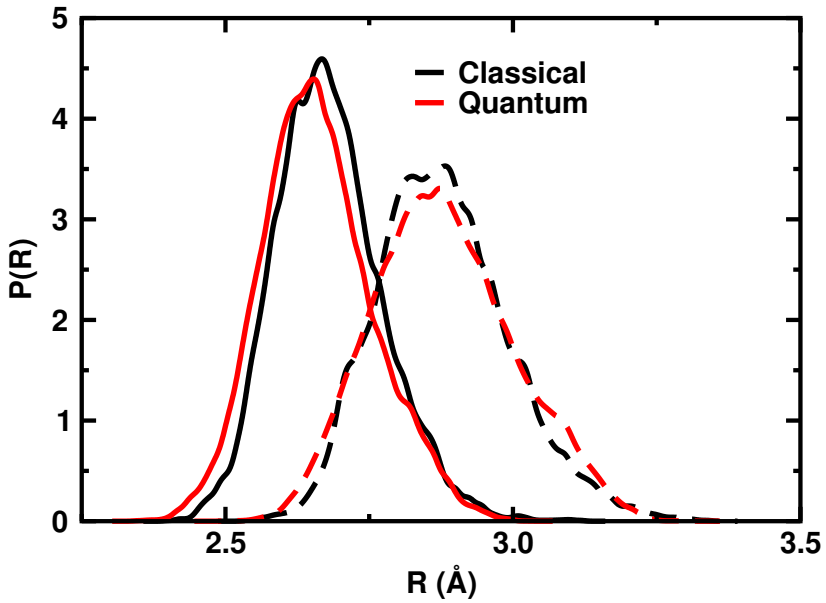

Fig. 4.2 The distribution of heavy atoms compression coordinate (R) is plotted for strong (solid lines) charge-charge hydrogen bond and charge-dipole (dashed line) hydrogen bond of L-glu system.

network within the structure which involve interactions between different chemical groups. The SHB highlighted in a rectangular region with a dashed red line. The hydrogen bonds formed by ammonium ions are shown in blue and orange dashed lines. Where different colours show the ammonium ion interacting with oxygens of different chemical groups. Similarly, the ring nitrogen forms a hydrogen bond with neighbouring ring oxygen (dotted green line) and oxygen of the SHB site (dotted orange line).

We focus first on the SHB, Panel b) of Fig. 4.3 showing the free energy profile of PTC obtained from classical and quantum simulations. As we see with the inclusion of the NQE's, the barrier turned to be flat. The panel c) and d) respectively illustrates the classical and quantum free energy distribution as a function of compression coordinate (R) and PTC. It is clear from the figure that the compression coordinate squeezes in quantum case hence strengthening the SHB. The difference depicted by the horizontal dashed line, which is a reference to the classical minimum and maximum value of the compression coordinate. Though quantum effects make the SHB barrierless, its asymmetric feature persists. To investigate the origin of this asymmetry, we have computed the radial distribution function of two oxygen atoms O_1 and O_2 (highlighted in panel b) of Fig. 4.3) separately with all nitrogen atoms.

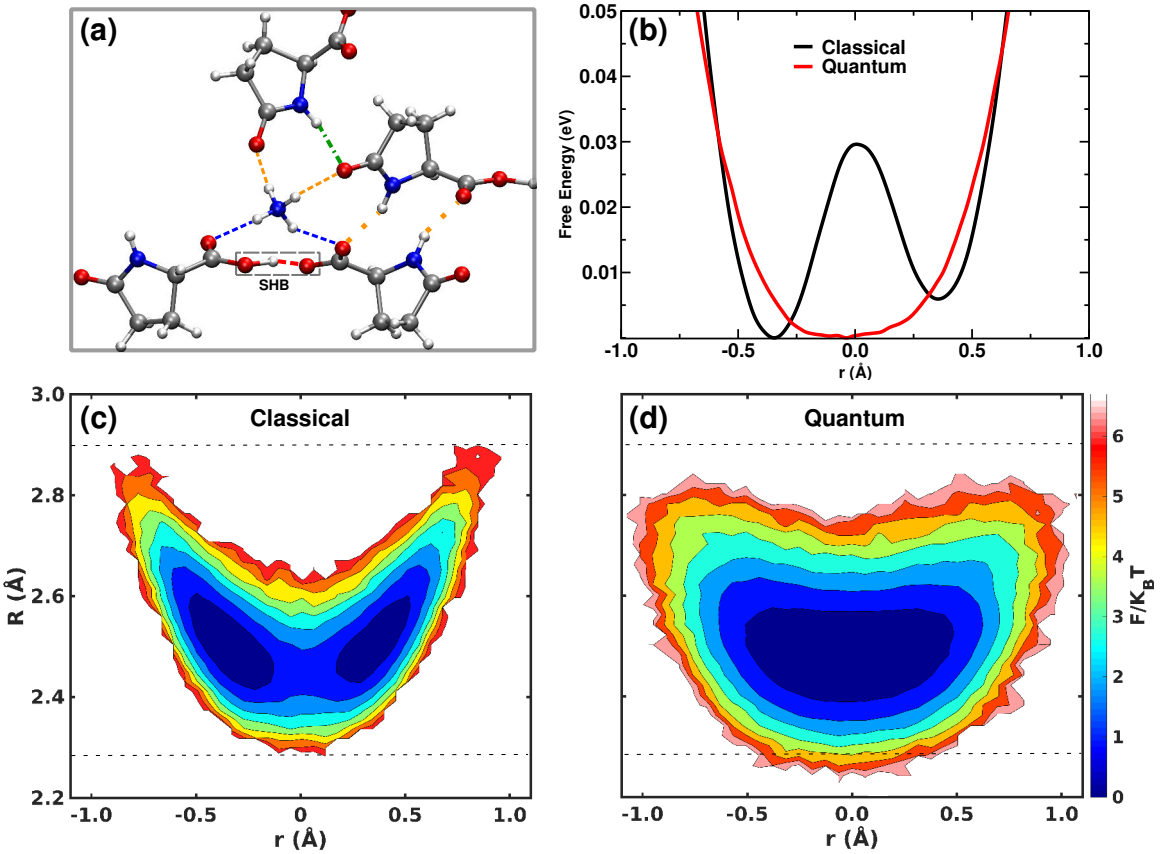

Fig. 4.3 (a) The zoomed snapshot of the L-pyro-amm structure, reflecting the dense hydrogen bond network in the vicinity of SHB region. The dashed colour lines illustrate different hydrogen bonds formed between different charge species. The network includes the SHB highlighted in the rectangular region with a dashed red line. The ammonium hydrogen bonds formed between different charge and dipolar groups as highlighted by dashed blue and orange lines respectively. Similarly, the interactions of ring nitrogen with charge and dipolar groups shown by dotted orange (charge) and green (dipole) lines. (b) The free energy profile of SHB as a function of PT coordinate is plotted with and without NQE's in c) and d). The two dimensional free energy profile as a function of PTC(r) and heavy atoms compression coordinate (R) is plotted for classical (c) and quantum (d).

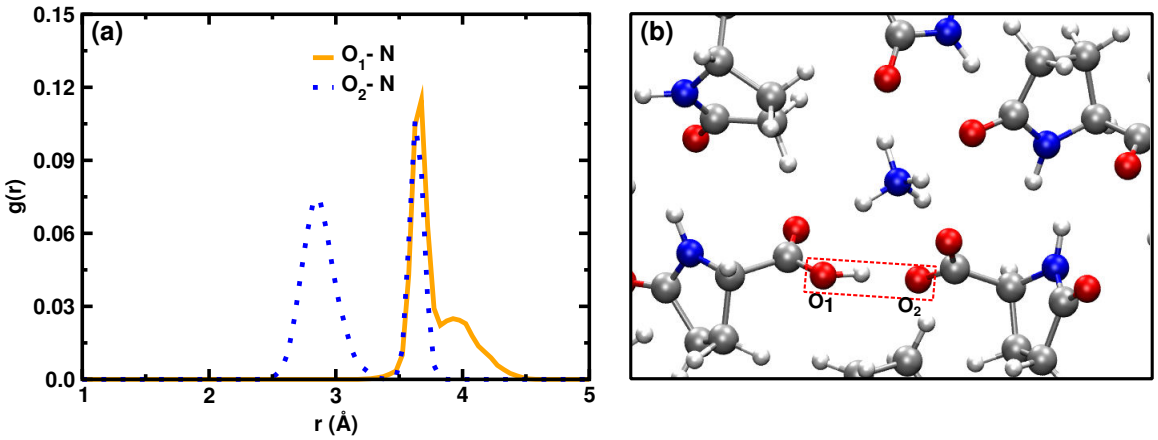

Fig. 4.4 The radial distribution function of the two oxygen atoms (O_1 and O_2 highlighted in lower right panel) with neighbouring nitrogen atoms.

The asymmetry in O_1 and O_2 environment is due to the position of ammonium ion, which spends more time close to O_2 then O_1. The best of our knowledge this kind of asymmetric feature of the SHB, particularly in single amino acid protein crystals has not been reported before. In other systems such as in high-pressure ice, the chemical environment for two oxygen atoms is similar. Therefore NQE's lead to the hydrogen bond symmetrization [99]. In the previous studies quantifying the number of short hydrogen bonds in an extensive database of protein structures shows that almost all protein ensemble contains short hydrogen bonds in the structure [126]. The length of these bonds considered less than 2.7 Å. As we already saw, the short hydrogen bonds facilitate proton delocalization in L-glu and L-pyro-amm system. One can argue that, is asymmetry in proton delocalization a generic feature of all proteins ? Moreover, how NQE's modulate this property for a variety of different short hydrogen bonds in different protein systems ?

Including SHB, L-pyro-amm structure is also complexed with ammonium ions which are interacting with different oxygen atoms in the surrounding. We will see shortly, the hydrogen bond formed by ammonium ions are quite dynamic because of its non-covalent bonded character. Over time it exhibits slow rotational and transnational modes which result in a continuous breaking and formation of hydrogen bonds with surrounding oxygen atoms. Panel a) of Fig. 4.5 showing the local environment around the ammonium ion where it interacts with 12 different oxygen atoms as shown. Oxygen atoms labelled from 1 to 4 belong to ringside while rest of eight making the base like a bowl belongs to SHB site. All these oxygen atoms are considered within five angstroms distance from the nitrogen of the ammonium ion. Panel b) of Fig. 4.5 illustrating the probability distribution of all the individual 12 distances. It is clear from the distributions, the N-O compression for different oxygen atoms could

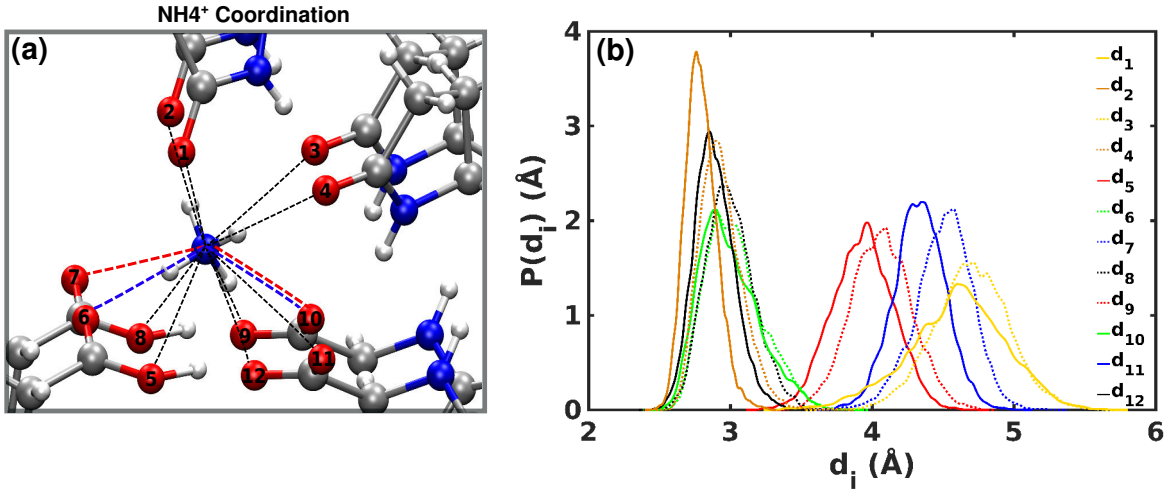

Fig. 4.5 (a) The zoomed snapshot of L-pyro-amm structure is illustrating the local environment around the ammonium ion. The ion is surrounded by twelve different oxygen atoms as labelled from 1 to 12. Among these twelve atoms, the first four oxygen atoms belongs to the ring site while remaining are from SHB site. b) Illustrates the classical probability distributions of all N-O distances.

exceed more than 1.5 Å. Among the 12, six oxygen atoms with even labels (2,4,6 ...) make the hydrogen bonds with ammonium at equilibrium length less than 3.2 Å, while atoms with odd labels (1,3,5,...) are at a greater distance than 3.5 Å.

During its time evolution, the ammonium ion also exhibits slow rotational modes. These modes allow a complete switching of its hydrogen bond from one oxygen atom to other. In order to investigate the ammonium ion rotational flips, we monitor the O-H distances involving ammonium ion to nearest oxygen atoms as shown by blue and orange dashed lines in panel a) of Fig. 4.3. Fig. 4.6 illustrates the time evaluation of these distances. The leftmost vertical panels of Fig. 4.6 showing the snapshots of crystal structure taken over different times. The snapshots highlight different orientations of ammonium ion as a function of time. The four hydrogen atoms of ammonium were colour-coded (black, orange, green and magenta) to keep track of their spatial location over time. In the middle column, the time evaluation of H-O distances is plotted with the same colour code of the corresponding hydrogen atom. It is clear from the figure that after 10's of picoseconds, the ammonium ion makes rotational transitions and bending of H-N-H angles. For example, the black hydrogen atom roughly after the first 45 picoseconds switched its hydrogen bond from ring oxygen to oxygen of SHB site. The switch in the atoms involving in the hydrogen bonds is clearly seen from the snapshot taken at two ps and 75.37 ps respectively. Similarly, the other three hydrogen atoms (orange, green and magenta) make transitions and involve in hydrogen bonds with different oxygen atoms over different times. Among all, the atom

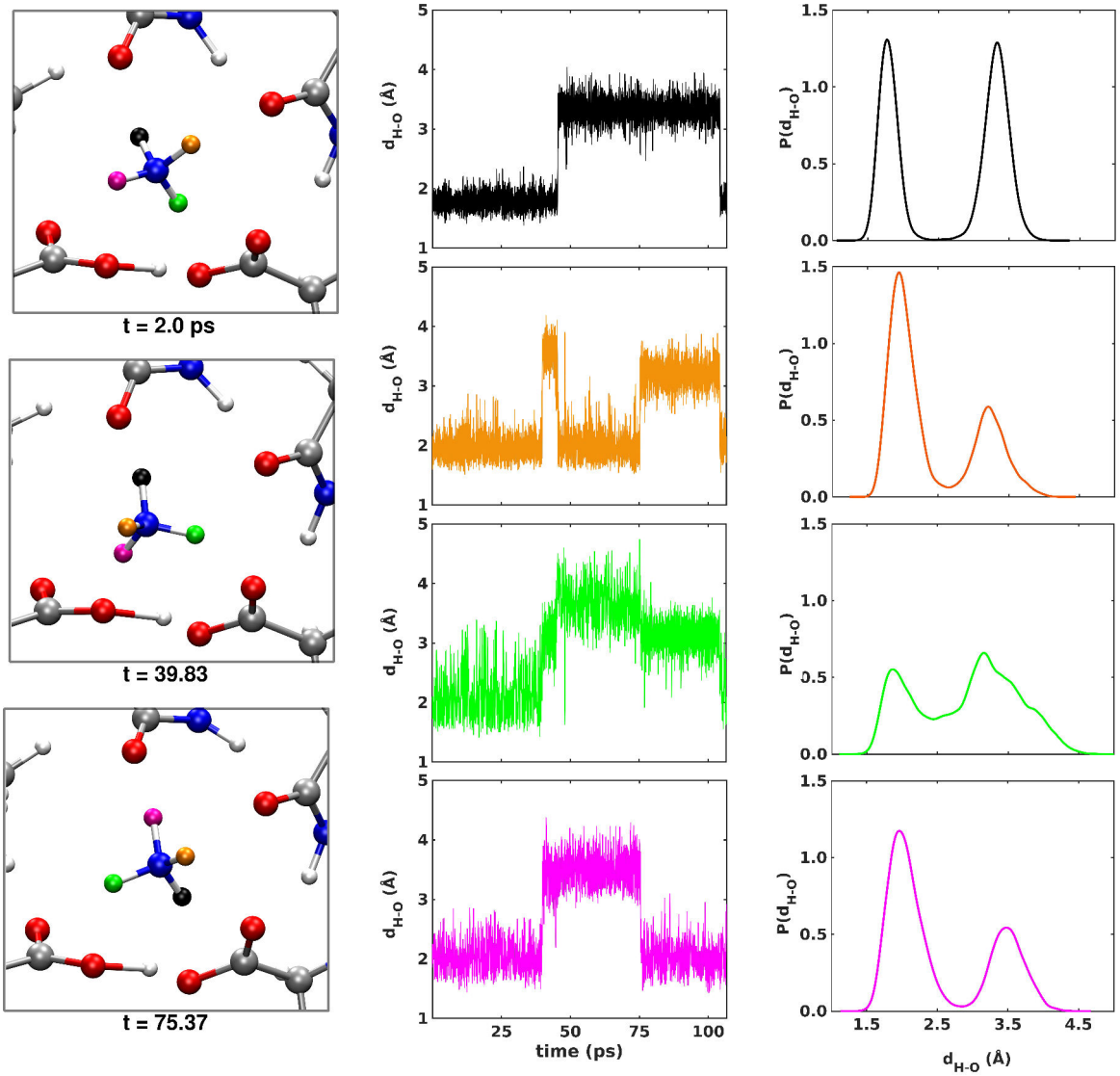

Fig. 4.6 The left vertical panel showing the snapshots of crystal structure taken over different times from molecular dynamics simulations, illustrating different orientations of ammonium ions. Each hydrogen of ammonium is colour coded in order to keep track of their location. The middle vertical panels illustrate the time series of H-O distances and the colour codes are the same as the atom's colour. The oxygen atoms considered here for distance calculations are those who are involved in hydrogen bonds with ammonium ion as shown in panel (a) of Fig. 4.3. The rightmost panels are showing the histogram of these distances.

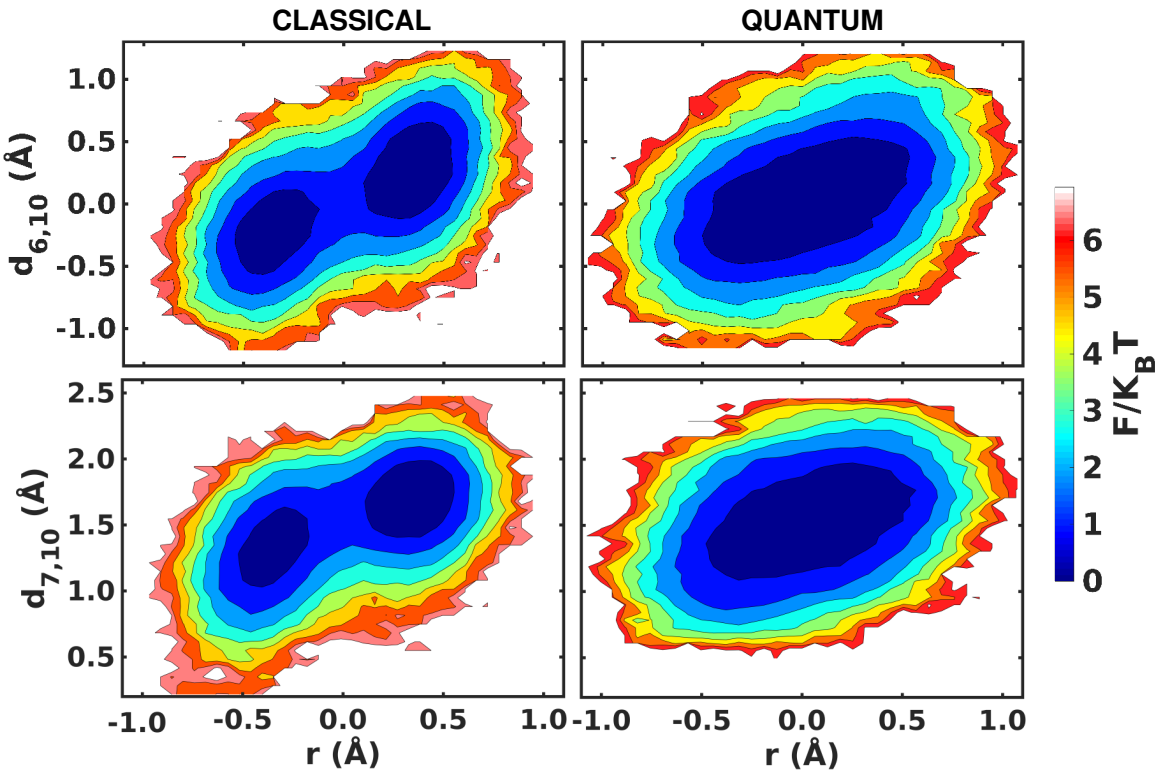

Fig. 4.7 The two dimensional free energy distribution as function of proton transfer coordinate and pairwise difference of N-O distances $d_{6,10}$ and $d_{7,10}$ is estimated from classical (left panels) and quantum simulations (right panels).

highlighted in green exhibits large fluctuations as shown from its time series and histogram in the rightmost panel. The H-O distance for this case stretch from ~ 1.5 to ~ 4.5 Å. We already have seen the importance of ammonium ion, which leads to asymmetry in the SHB. Also, its slow vibrational and rotational modes alter the hydrogen bond patterns continuously in L-pyro-amm systems. Therefore is interesting to see if proton delocalisation is sensitive to translational and rotational modes of the ammonium ion. In next section we discussed this coupling in details.

4.3.3 Coupling Between Proton Transfer to Slow Vibrational Modes of Ammonium Ion

In aqueous systems, the coupling of PT to structural fluctuations of the nearby chemical environment is a long-studied problem. The structural diffusion of excess proton in water is well understood under the framework of Grotthuss mechanism [127–130] which explains the mechanism associated to the structural diffusion of proton along the hydrogen bond network [131, 132]. As shown in previous studies, the proton transfer potential is modulated

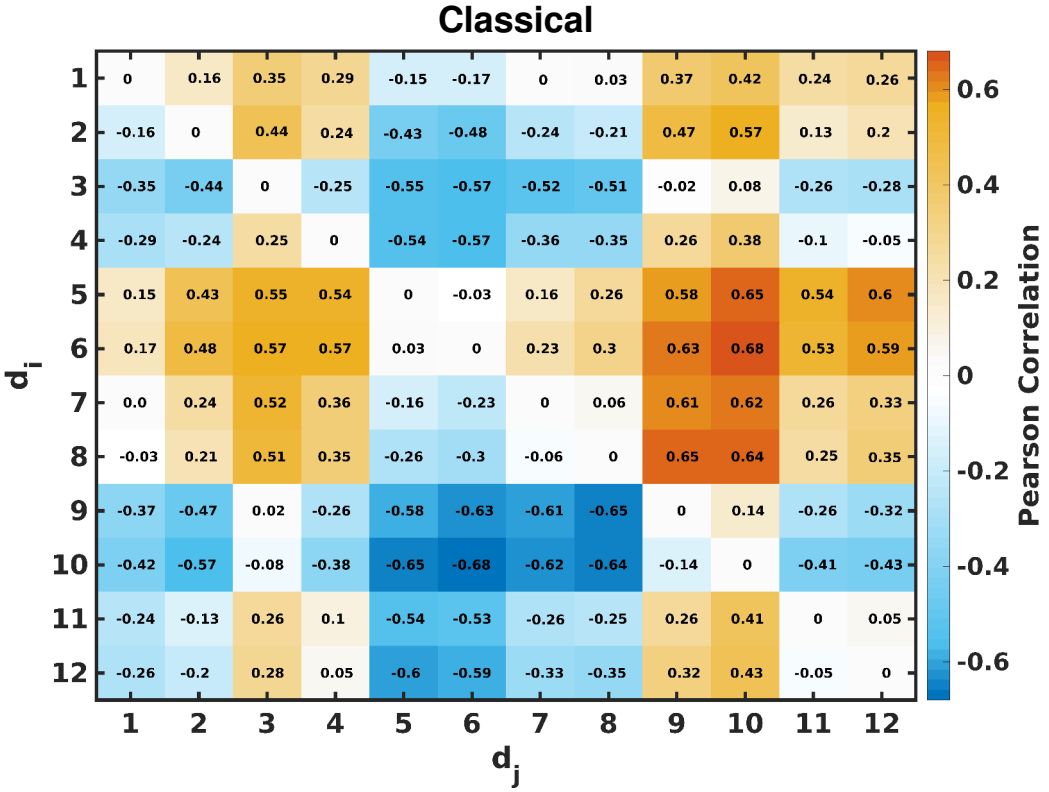

Fig. 4.8 The Pearson correlation matrix is plotted for all the pair of distances shown in panel a) of Fig. 4.5.

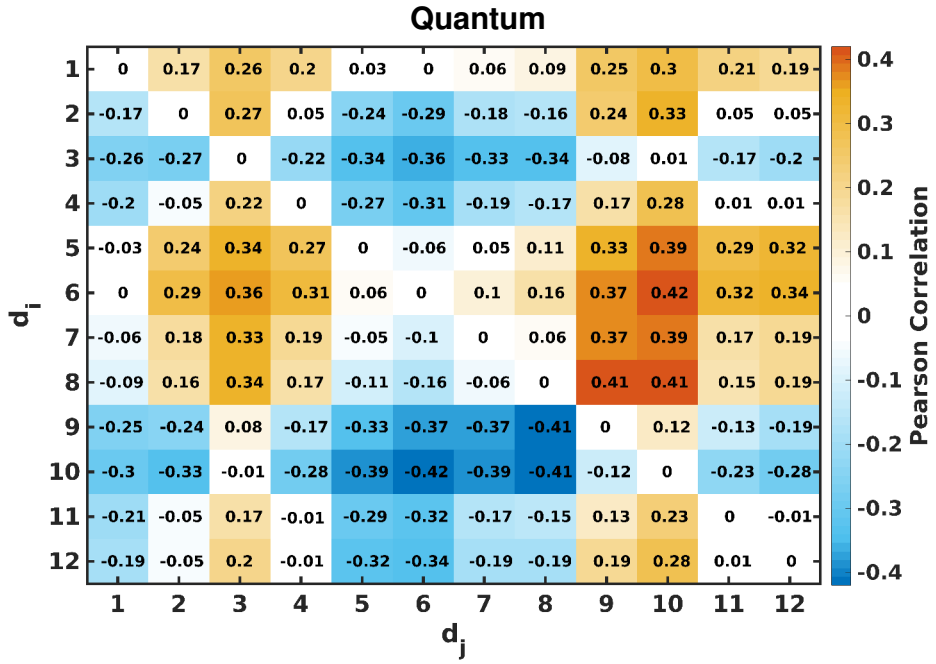

Fig. 4.9 NQE on Pearson correlation matrix plotted between ptc and all the pair of N-O distances.

by fluctuations of lower frequency modes of the surrounding environment [133]. It is thus interesting to examine if there are similar modes in L-Pyro-Amm which are coupled to the proton transfer. In order to asses this information, we computed the correlation between proton transfer coordinate and pairwise difference of the N-O distances $d_{6,10}$ and $d_{7,10}$ (see the red and blue dashed lines in panel a) of Fig. 4.5). The top and bottom two panels of Fig. 4.7 illustrate this coupling both classically (left) and quantum mechanically (right) for the two pairs of distances. As seen in the classical case, with the double-well character, proton transfer is strongly correlated with vibrational modes of ammonium ion. As we see, the barrier of SHB is very small to persist against quantum simulations. Therefore, quantum effects significantly weaken the structural correlations.

In order to investigate the extent of this coupling in details, we computed the Pearson correlations coefficients correlating the PTC to all the pairwise distances involving the 12 N-O compression coordinates. Fig. 4.8 shows the Pearson correlation matrix calculated from classical trajectories. It is clear from the values that the oxygen atoms from the SHB site relatively show stronger correlations compare to the atoms from the ring head sites. As we already see in Fig. 4.7, the quantum effects weaken the structural correlations. In order to investigate the NQE, we re-plot the correlation matrix now by using quantum trajectories.

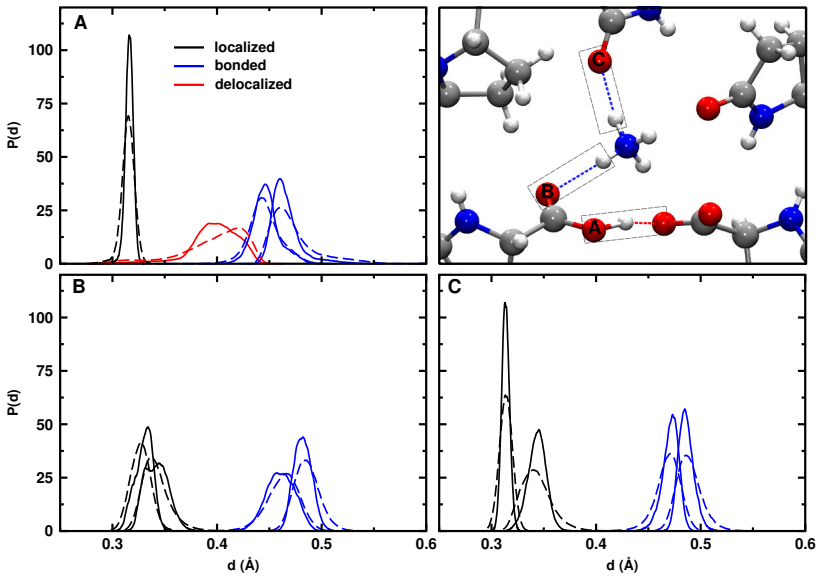

Fig. 4.10 The distributions of the Wannier's centres position from the oxygen atoms of SHB (A) and hydrogen bonds of the ammonium ions (B and C) of L-pyro-amm system are plotted for both classical (solid lines) and quantum simulations (dashed lines). Compared to the classical results, the electronic density get more polarised by turning on the quantum effects as seen from the broadness of the peaks. The substantial polarization effects are seen along the short hydrogen bond where quantum delocalisation of the proton changes the covalent character of O-H bond and hence the delocalisation of the electronic density.

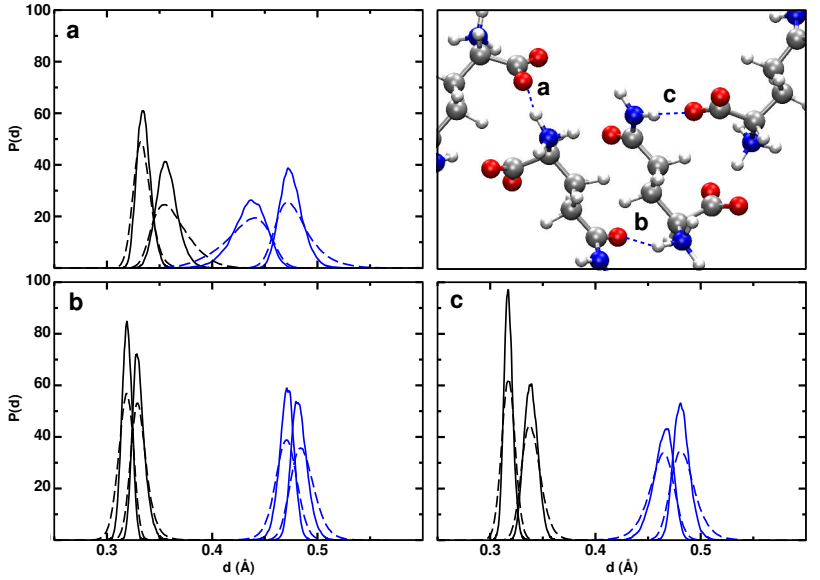

Fig. 4.11 A similar analysis of Wannier centers distributions as shown in Fig. 4.10 is illustrated for the hydrogen bonds in L-glu system. The electronic polarisation sensitive to quantum effects is strong along the short hydrogen bond (see panel a) as compared to the normal hydrogen bonds (see panels b) and c)).

Quantum effects as expected weaken all the structural correlations but the main trends remain the same. The correlations of SHB site oxygen atoms relatively more compared to the atoms from the ring site. This analysis shows the importance of ammonium ion modulating the structural properties of SHB. It provides rich structural diversity in the local environment around the SHB site, which facilitates the proton transfer through the hydrogen bond.

4.3.4 Electronic Properties of the Hydrogen Bonds

In the previous chapter, we show that at T = 0 K, the low energy electronic transitions involve collective charge reorganisations at several parts of the structure, including short hydrogen bond atoms. For small clusters calculations in a protein environment, we saw that the electronic response is sensitive to proton delocalisation along the hydrogen bond.
In order to dig more on the coupling between electron-nuclear motion, we identify the number of Wannier centers within 0.6 Å from the oxygen atoms of different hydrogen bonds in both L-pyro-amm and L-glu systems. The distributions shows that the electronic structure of different hydrogen bonds is very different and is sensitive to the NQE's. More electron polarization is observed along the short hydrogen bonds where the nuclear motion is strong. For instance, in panel A) of Fig. 4.10, the distribution of Wannier centres is shown for the oxygen atoms labeled as A) which is involved in proton transfer along the SHB. Classically the distribution peaks around $\sim$ 0.4 Å shows a strong polarisation of the Wannier centre (solid red line). The peak stretched more to the larger distance by including the quantum effects (dashed red line). This particular behaviour of electronic polarisation is coupled to the proton delocalisation as it is not observed for other cases where oxygen atoms normal normal hydrogen bonds with no proton transfer (see panel B) and C) of Fig. 4.10). Similar trends are observed in the case of glutamine hydrogen bonds. As illustrated in Fig. 4.11, more polarisation of the electronic degree of freedom is associated with strong hydrogen bonds, which facilitate proton delocalisation as seen in panel a) of Fig. 4.1.

4.4 Conclusion

The glutamine aggregates differ in terms of their hydrogen bond network. The difference is reflected from their structural, dynamical and electronic properties. These properties modulate a lot by inclusion of NQE's.
The NQE's strengthen the short hydrogen bond and hence the proton delocalisation.
The structural correlation between low barrier proton transfer coordinate and fluctuations of the nearby environment is well characterised by the quantum effects which show weak

correlations compared to the classical case. Similarly the electronic properties of different hydrogen bonds are sensitive to the classical vs quantum picture of proton motion. Electronic polarization observed to be strong along the short hydrogen bonds. In future, it would be interesting to investigate the role of quantum effects on the optical properties of these systems.

Chapter 5

Structural and Dynamical Heterogeneities at Glutamine-Water Interfaces

5.1 Introduction

The behavior of water at the surfaces of solid amino-acid crystals has received little attention despite its importance in nucleation processes. In this work, we take a first step to fill this gap by using molecular dynamics simulations to study the structural and dynamical properties of water near the (100), (010) and (001) surfaces of L-Glutamine crystals. The stability of these highly hydrophilic surfaces serve as excellent model systems for interrogating the behavior of water.

Water serves as a ubiquitous solvent in a wide variety of physical, chemical and biological processes [134–137]. One of the most studied problems in physical chemistry pertains to how surfaces perturb the structural and dynamical properties of interfacial water. Numerous experimental [34, 35, 138–149] and theoretical [32, 150, 151, 33, 152–154, 152, 155–159, 30, 160–163] studies have been devoted to investigating the extent to which water near biological surfaces is altered and in particular, how different it is from the bulk. The cumulative evidence over the last couple of decades built on studies of water near mostly proteins and DNA is that there is a slow down of a small sub-population of water molecules by a factor of $\sim$4-7 near the interface [31].

The retardation of water near biological interfaces is often understood in terms of the presence of either energetic or geometrical disorder [164, 141]. In the former, polarizing electric fields can create traps for water molecules whereas in the latter, the underlying

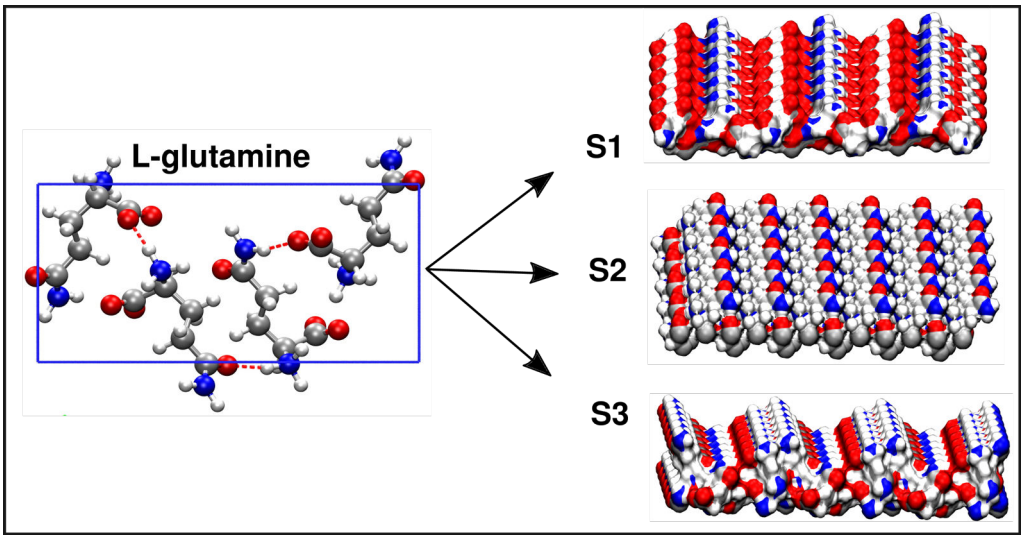

Fig. 5.1 The left panel of the figure shows the unit cell of L-glutamine obtained from Ref. [5] from which a supercell is constructed and then used to generate the three surfaces shown in the right panel: S1 corresponds to (001), S2 to the (010) and S3 to the (100) surface. The different colour codes represent different elements: oxygen in red, nitrogen in blue, carbon in grey and finally hydrogen in white.

geometry affects the diffusion. One of the challenges in interpreting the origins of these effects, is that the water dynamics is obviously coupled to the soft modes associated with the fluctuations of the biological system [36, 37, 165, 38, 39, 158]. In this context, disentangling the molecular origins of dynamic heterogeneities of water becomes rather challenging since the water mobility is also coupled to the dynamics of the solute. In the last decade or so, there has been an increased interest in understanding the properties of solid-aqueous interfaces [166]. There have been several studies investigating the dynamical properties of water near metals [167–169], metal oxide surfaces [170] and also near inorganic mineral surfaces [171]. On the other hand, the behavior of water in close proximity to solid-organic surfaces remains poorly understood. These types of interfaces play an important role in biophysical and engineering processes such as protein crystallization and also nucleation or precipitation of molecular aggregates in solution [172]. Salvalaglio and co-workers have reported the role of different solvents in modulating the morphology of crystal forms of urea [173]. They find that the type of solvent has a significant impact on the shape of the crystals. In the growth of calcium carbonate crystals, Gale and co-workers found that the de-solvation of water molecules at the interface is an important part of the crystal growth mechanism [174, 175]. In all these studies however, a detailed characterization of water dynamics at the interface was not undertaken.

In this work, we use classical molecular dynamics simulations to simulate several interfaces associated with a crystalline form of the amino acid, L-glutamine [5]. Pyroglutamine aggregates have been implicated in numerous pathological conditions related to neurodegenerative diseases [18]. In the last few years there has also been an increased interest in understanding the optical properties of these and other types aggregates [54]. More specifically, hydrogen bonded aggregates of proteins and amino-acids have been found to exhibit fluorescence in the absence of aromatic groups [57, 108]. In this work, we focus on characterizing the surfaces of these crystals in contact with liquid water. Each surface that we examine in contact with liquid water, remains stable on the timescale of hundreds of nanoseconds and features distinct signatures in the chemistry and geometry. The advantage of these systems is that the water dynamics occurs adjacent to a rigid surface.

Our simulations reveal a rich and diverse physical behavior of water at the three different surfaces. The relative orientation of glutamine molecules at each interface leads to different exposure of the charged termini and side-chains to the solvent. This in turn leads to the formation of structured water extending up to a length of $\sim$1 nm. Each surface is characterized by different structural and orientational correlations of water at the interface. We determine several dynamical properties of the interface and show that a small fraction of the water in this region, is reminiscent of a glassy liquid as seen by the presence of rotationally arrested water molecules in some cases and a slow down of water diffusion near the interface. These results have important implications for understanding the growth of these and other organic interfaces such as amino acids, DNA bases and poly-peptides in solution. In the last decade there have also been several advances in surface specific spectroscopy such as sum frequency generation (SFG) allowing for the investigation of the dynamics of water at the complex aqueous interfaces. Our simulations should also motivate experiments like these on crystal amino-acid interfaces since they present very clean systems where one does not have to deal with the soft modes of the protein. Thus disentangling the effects of geometric and energetic disorder can be examined.

The paper is organized as follows: in Section 5.2 we begin with a summary of the systems simulated and computational methods used in this work. In Section 5.3.1, the static structural, electrostatic and orientational correlations of different interfaces are discussed. In Section 5.3.2 we move on to characterizing the translational and rotational dynamics of water molecules at the three surfaces. Section 5.3.3 discusses the effect of creating a crowded environment of glutamine molecules at the interface possibly during nucleation, on the water dynamics. Finally we end in Section 5.4 with some discussion and perspectives of our results.

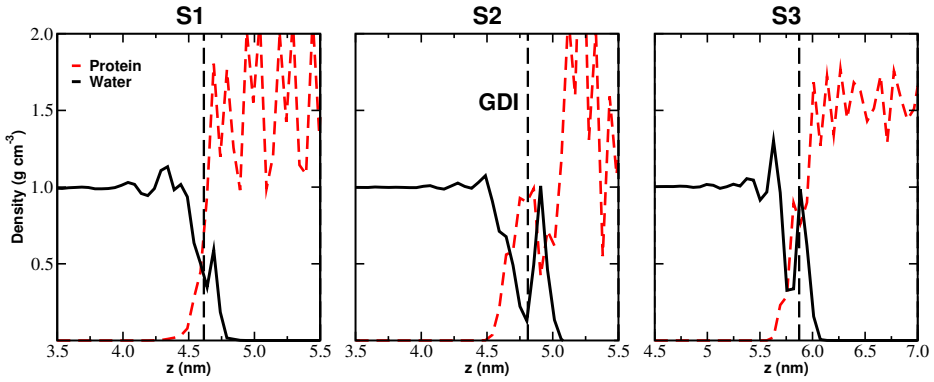

Fig. 5.2 The solid-black and dashed-red curves correspond to the water and protein densities for the three different surfaces simulated. The vertical dashed line corresponds to the Gibbs Dividing Interface (GDI). Near all the three surfaces we observe a structured layer of water.

5.2 Computational Methods

In order to investigate the structural and dynamical properties of L-glutamine-water interfaces, we generated three different crystalline glutamine slabs by creating supercells from the unit cell of the experimentally resolved L-glutamine crystal. The left panel of Fig. 5.1 shows the unit cell of the glutamine crystal which contains four glutamine residues. Note that the crystal is held together by strong hydrogen bonds involving the charged termini groups as well as the polar side-chain. Three interfaces were then created by opening up gaps in the x, y and z direction yielding the (100) (S1), (010) (S2) and (001) (S3) surfaces, respectively. Systems S1 and S2 were made up of 432 glutamine residues, while S3 contains 428 residues. The cell dimensions of the three systems were as follows: 4.803 4.656 3.600 *nm* for S1, 4.656 4.590 3.200 *nm* for S2 and 3.060 6.404 3.880 *nm* for S3. Most of our analysis reported in this paper focuses on the structure and dynamics of water near the pristine crystal surfaces. In order to shed some light on possible initial conditions that form during crystal nucleation, we also conducted some simulations where glutamine molecules were inserted in the bulk. In particular, we conducted simulations increasing the concentration of glutamine molecules in three steps: 0.3, 0.7 and 1M. In the main text we present some of the analysis observed for the 1M concentration and defer the results for the 0.3 and 0.7 M to the Supporting Information.

All the molecular dynamics (MD) simulations were performed using the open source package GROMACS [176]. In all these simulations, we used the OPLS-AA [177] force field together with the TIP4P water model [178, 179]. The three systems S1, S2, S3 in pure water consisted of 6899, 6910 and 7748 water molecules, respectively. In order to assess the sensitivity of some of our reported findings to the choice of both the protein and water model used, we repeated the simulations of one of the interfaces (S1) using a

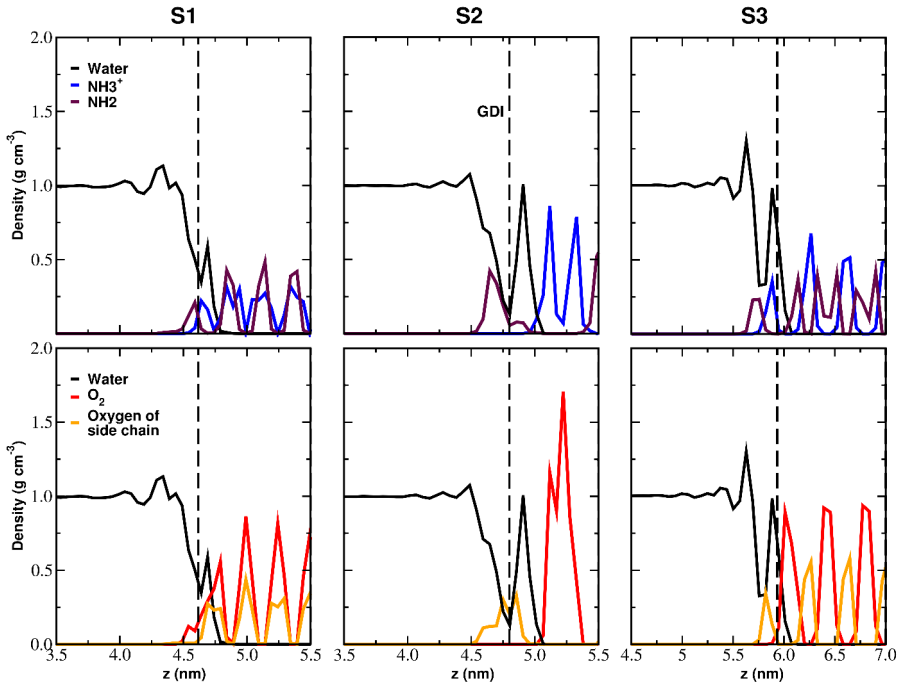

Fig. 5.3 The top panel shows the water density overlapped with the densities associated with donor groups of glutamine (NH_2 and NH_3+). The bottom panel shows the water density overlapped with the densities associated with acceptor groups of glutamine (COO− and the amide C=O of the side chain)

.

combination of CHARMM27 [180] and TIP3P water model [178] (see Fig. 1 in SI). A cut-off radius of 1.4 nm was used to create non-bonded pair list. For the short-range non-bonded interactions a cut-off length at 1.2 nm was chosen for a shifted Lennard-Jones potential while the long-range electrostatic interactions were taken into account via Particle Mesh Ewald-Switch [181] (PME-switch) method with a Coulomb switching cut-off at 1.2 nm. A long range dispersion correction was applied for truncating the van-der-Waals interactions. All bonds were constrained using the LINCS algorithm [182]. A timestep of 2 fs was used for the Verlet integrator. All simulations with 0M concentration were conducted in the canonical ensemble (NVT) at 300 K using the velocity-rescale thermostat [92] with a time-constant of 0.1 ps.

The three surfaces were each run for $\sim$200 ns of which the first 10 ns was treated as equilibration. For the concentrated solutions, all the calculations were conducted in the isothermal-isobaric ensemble at a pressure of 1 bar and temperature of 300 K. The pressure control was carried out by using the semi-isotropic Parrinello-Rahman barostat [183]. The use of the semi-isotropic pressure coupling scheme has already been noted in previous studies when simulating crystal-liquid interfaces [173]. In these simulations after equilibration, the production runs were extended upto 200 ns.

5.3 Results

Our results are divided broadly into two sections: we focus first on establishing the static properties associated with the three different interfaces examined. This includes density and orientational correlations of the water as well as understanding the differences in the geometry and chemistry of the different surfaces. We subsequently examine various dynamical properties of the water including the extent of the perturbation to their rotational and translational mobility.

5.3.1 Statics: Density, Charge and Orientational Correlations

Before describing the structural and orientational correlations of the solvent, it is useful to first build our intuition on how each of the three surfaces S1, S2 and S3 are characterized by very different morphology in both the surface roughness and exposure of different chemical groups to the solvent. The left panel of Fig. 5.1 shows the unit cell of the glutamine crystal from which our surfaces are built. In this figure we see that glutamine is an amino acid in its zwitterionic form (a positive and negatively charged N and C terminus respectively). The side chain of glutamine is a simple amide group that hangs off two CH2 hydrocarbon groups.

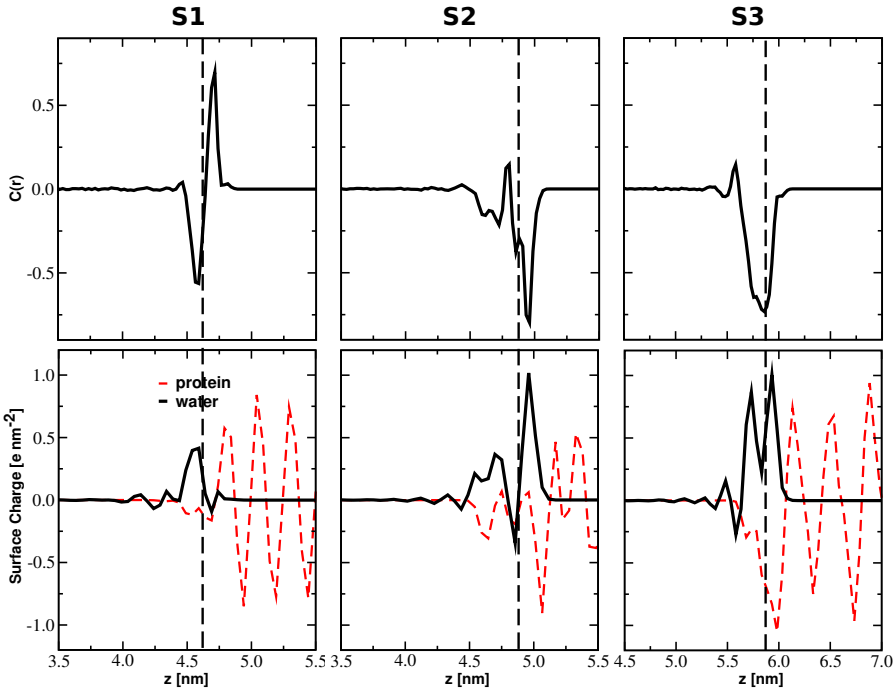

Fig. 5.4 The top panel of the Fig shows the orientational correlation function of water molecules near each surface. Surfaces S2 and S3 appear to have very similar orientational correlations as discussed in the main text. The bottom panel of the figure illustrates the surface charge obtained for water and glutamine.

The right panels of Fig. 5.1 visually depicts the three surfaces color coded in a manner that shows how these different chemical groups are exposed. The differences in the orientation and relative positioning of each terminal group as well as the side chains, leads to each surface having a unique roughness as well as charge distributions.

In order to understand how each interface perturbs the water in close vicinity to it, Fig. 5.2 shows the joint water and protein densities for each surface. In determining the protein densities, all atoms of each amino acid were used. The dashed vertical line in each figure corresponds to the position of the Gibbs dividing interface (GDI) constructed for protein density using a procedure previously reported by Garett and co-workers [184]. Interestingly, we observe that in each system, the water structuring extends over a length scale of $\sim$1 nm. More specifically, there appears to be two regimes in the water layering - one that penetrates into the crystalline structure of the protein and another which extends away from the protein surface. Another striking feature of the density oscillations of the water is that they are characterized by subtle differences for each surface. The S2 surface in particular, has the most pronounced water peak within the crystal followed by S1 and then S3.

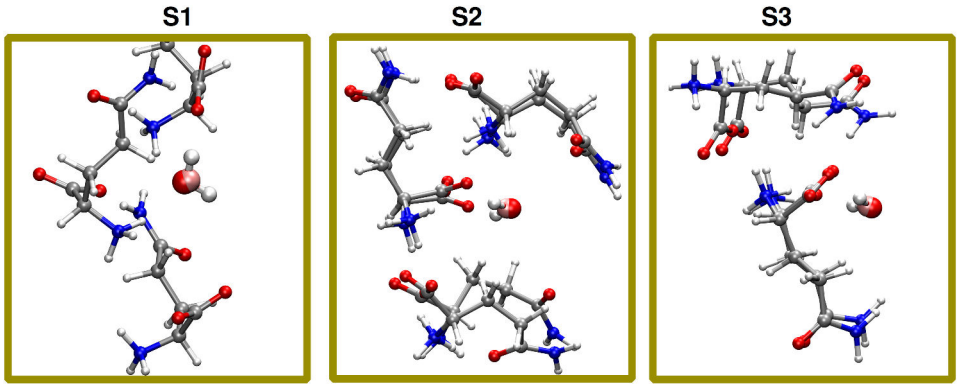

Fig. 5.5 Snapshots taken from the trajectory showing the orientation preference of penetrated water molecules trapped in the inner cavities of each surface.

The structuring we observe at each interface also involves orientational polarization of water molecules. Water penetration into proteins has been observed in several systems with channels or cavities [158, 185, 186]. To best of our knowledge, the presence of highly structured water layers in the context of organic crystal-water interfaces has not been previously reported. The water penetration on the different surfaces is also tuned by the underlying roughness of the interface.

The complexity of each surface is also dictated by how the different polar groups of the amino acid orient relative to each other. It is also important to understand how the water layering is affected by the presence of different charge groups. Fig. 5.3 shows density of the charged groups along the z-axis. Firstly, we observe rather clearly that in the (100) surface, the N and C termini are equally exposed to the solvent while in (010) and (001), the C terminus is buried deeper on the protein-crystal side. This leads to a layer of water that is sandwiched between the positive and negative charge of the N and C terminus respectively.

Besides the structural correlations there are also orientational effects. In order to quantify this, we determined how the water dipoles were oriented relative to the surface normal as a function of distance r from a reference interface. This orientational correlation function is defined below by the $C(r)$

$$C(r) = \frac{1}{N_t}\sum_{i=1}^{N_t}\frac{1}{n_j(r)}\sum_{j}\frac{\mu_j.\mu_0}{|\mu_j|.|\mu_0|} \tag{5.1}$$

In the equation above, $n_j(r)$ is the number of water molecules in a particular slice at distance r from the interface and μ_0 is the vector normal to the surface. A similar procedure was also performed by Galli and co-workers to characterize orientational correlations in bulk water [187].

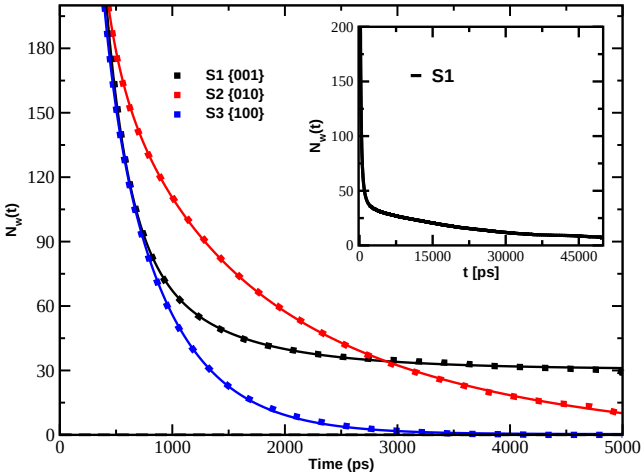

Fig. 5.6 Residence time correlation functions as defined in the text for water molecules near the three surfaces. Black, red and blue curves correspond to surfaces S1, S2 and S3 respectively. The inset shows the long tail of permanent water molecules near the surface S1 where 8 molecules stayed continuously up to 50 ns.

Table 5.1 The values of the fitting parameters for survival probability curves.

Systems	$\langle\tau_s\rangle$ (ps)	n_s	γ	τ_2(ps)	n_2	τ_3(ps)	n_3	n_p
S1	226.432	686.80	0.50	180.76	686.37	41.88	138.23	30.31
S2	1244.36	357.78	0.61	118.99	848.62	12.36	196.27	7.60
S3	129.343	1110.33	0.76	657.92	226.87	—	—	0.34

The upper panel of Fig. 5.4 shows the orientational correlation function of water for the three different surfaces as a function of distance from the GDI (shown again as dashed vertical line). Again, at each surface, the water dipoles have very particular correlations. Surface S2 and S3 are more similar to each other whilst S1 is distinctly different. The positive and negative values of the correlation function indicate the presence of water dipoles pointing in opposite directions relative to the surface. The vast majority of this variation comes from the differences in polarization of the penetrated water layer and the water further away from the interface. In the case of S1, these water molecules anchor themselves so that they donate and accept 2 hydrogen bonds to and from the C-termini and N-termini respectively. Water molecules that are penetrated into the crystal for surfaces S2 and S3 surface are oriented in the opposite direction as seen by the negative sign of $C(r)$ in Fig. 5.4. Fig. 5.5 gives a

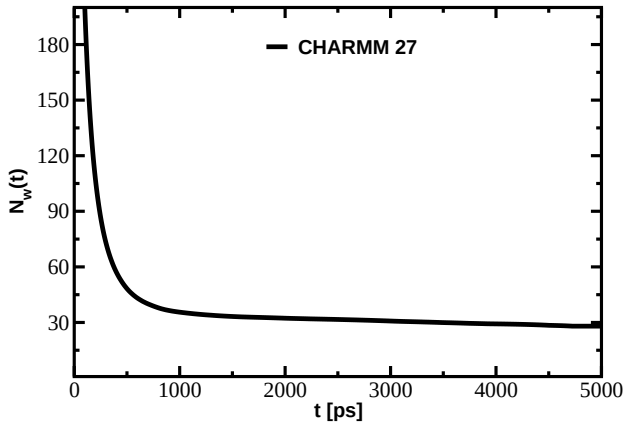

Fig. 5.7 The residence time of water molecules in the hydration shell of S1 surface is shown. The simulations were done by using the CHARMM force field with the TIP3P water model.

more qualitative and illustrative view of these effects showing typical snapshots of water molecules near the three different surfaces reflecting the differences in orientation.

The difference in orientational polarization at each surface is in turn rooted in how the different groups of the amino acids layer at the interface. This can be appreciated more easily by examining the surface charge obtained as a running integral of the total charge density of water and protein along the z-axis. For the case of the S2 and S3 surfaces, the negative orientational correlation of water is due to the hydrogens pointing to the surface resulting in a positive charge density slightly beneath or above the GDI which is compensated by the negative protein charge originating mostly from the C-terminal oxygen groups. Since there is no sharp separation between the positive and negative charges at surface S1, the orientation correlations are not so distinctly reflected in terms of the total charge as we did for the cases of surfaces S2 and S3.

5.3.2 Water Dynamics at Glutamine Surfaces

In the preceding section, we have established that each of the three glutamine interfaces examined has a complex chemistry and geometry which in turn affects the density and orientational correlations in non-trivial ways. For example, one of the interesting features is the presence of water layers that appear to be incorporated into the crystal structure of the amino-acid. In the following, we will examine how these features are reflected in the translational and re-orientational dynamics of water near the three surfaces. In particular, there have been numerous studies showing that biological interfaces slow down re-

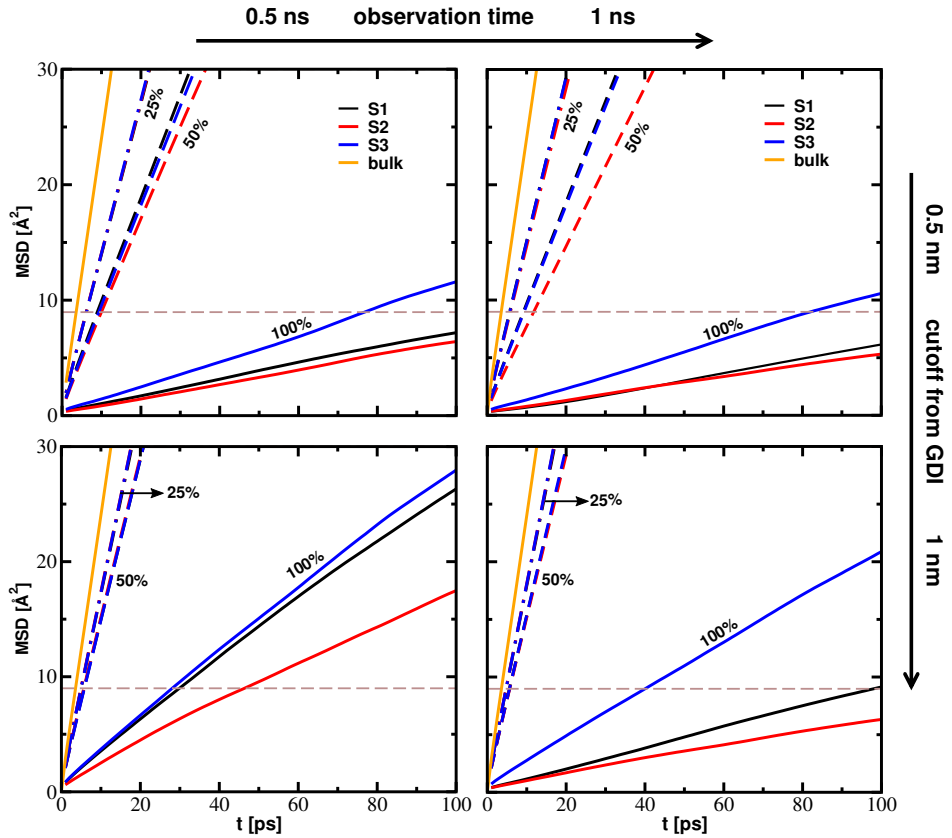

Fig. 5.8 The MSD of water molecules is plotted as a function of their residence time. The water residency was considered from 25% to 100% of the total observation time. The top and bottom panels illustrates the MSD for the three surfaces for waters within 5 Å and 10 Å respectively from the GDI. The left and right panels instead, at each cutoff, shows the MSD for water molecules calculated for total observation time of 0.5 ns and 1 ns respectively. The dashed brown lines shows the distance that a water molecule would diffuse corresponding to the length of a hydrogen bond (∼3 Å)

orientational and translational dynamics as compared to bulk. The translational dynamics of water at the three interfaces was studied using two metrics: first the residence time of waters and secondly the mean squared displacement (MSD) of the water molecules at the interface. The residence time of the water molecules in the hydration shell is estimated by calculating the survival probability $N_w(t)$ as reported in several previous studies [150, 33, 151] The residence time correlation function is described in the equation below where $P_i(t_n,t)$ is the conditional probability for each ith water molecule, such that $P_i(t_n,t) = 1$ if it remains within the hydration shell in the time interval t_n and $t_n + t$ and is otherwise 0.

$$N_w(t) = \frac{1}{N}\sum_{n=1}^{N_t}\sum_{i} P_i(t_n,t) \tag{5.2}$$

Fig. 5.6 compares the residence time correlation function for the water molecules near the three surfaces where we focused on those waters which are within 10 Å of the GDI. Interestingly, the three surfaces exhibit very different water exchange dynamics. In particular, we see that for the S1 surface, on the timescale of 5 ns, there are $\sim$30 waters that remain permanently attached to the surface without exchange. In the case of S2, on the same timescale only 7 waters remain while for S3 there is a complete turnover.

In order to get a more quantitative measure of the timescales associated with the dynamics, all the residence time correlation functions were fit to a combination of a stretched exponential and several exponential functions similar to that performed by Rossky and co-workers [150]:

$$N_w(t) = n_s exp(-t/\tau_s)^{\gamma} + \sum_{i=1}^{2} n_i exp(-t/\tau_i) + n_p \tag{5.3}$$

where n_p refers to the number of permanent water molecules which remain continuously in the hydration shell within the time-window examined. The average characteristic time $\langle\tau_s\rangle$ is obtained by:

$$\langle\tau_s\rangle = \int_0^{\infty} exp(-t/\tau_s)^{\gamma}\,\mathrm{d}t = \frac{\tau_s}{\gamma}\Gamma(\frac{1}{\gamma}) \tag{5.4}$$

The parameters obtained from the fit are shown in Table 5.1. The use of stretched exponential forms has typically been attributed to systems involving glassy heterogeneous dynamics [188, 33, 32, 189]. For all the three surfaces, the γ parameter is different from 1 suggesting this feature. Interestingly, we also see that each surface has a different γ value. This is not so surprising in light of the differences in structural and charge correlations that were discussed earlier. Table 5.1 shows that the residence time exchange of water near surface S2 exhibits the slowest dynamics whereas S3 has the fastest.

The S1 surface has a rather peculiar feature as seen by the non-zero value of n_p. On the timescale of 5 ns, we observe that there are still 30 water molecules that remain trapped at the surface. In the inset of Fig. 5.6 the residence time correlation function for S1 is extended up to 50 ns - even up to this timescale, there are still 8 water molecules that remained trapped. This surface is thus characterized by a long turn over in the dynamics of a small sub-population of waters which correspond to those water molecules that are locked at the surface and stabilized by strong electrostatic interactions involving the N and C termini (see leftmost panel S1 of Fig. 5.5). In order to assess the sensitivity of this result to the choice of the force field, we repeated the simulations for the S1 surface using CHARMM [180] and TIP3P [178]. Fig. 5.7 illustrates the survival probability of water molecules residing in the hydration shell of the S1 surface. The number of the trapped water molecules obtained with CHARMM is 28 after 5 *ns*, while it was 31 with the OPLSAA force field and TIP4P water model. Thus the long-lived trapped water molecules at the interface appears to be a generic feature. The rather long residence times observed in the preceding analysis strongly suggests a slow down in the diffusion near the interface. In order to interrogate the translational dynamics of water, we determined the mean square displacement (MSD) of different populations of water molecules at the interface. The criterion for defining the different types of water molecules was built on various measures: their total residency time as indicated by Fig. 5.6, the thickness of the interface and finally the percentage time that water molecules remained within some distance from the interface. To calibrate ourselves on the various parameters related to the mobility that will be discussed shortly, we determined the MSD for a bulk water simulation of TIP4P and determined the diffusion constant to be $3.88 \times 10^{-5}\text{cm}^2$ which is consistent with previous reports [190].

Table 5.2 The values of the fitting parameters for first rank and second rank dipolar relaxations

	$P_1(t)$			$P_2(t)$		
Systems	τ_R^1 (ns)	γ	$\langle\tau_R^1\rangle$	τ_R^2 (ns)	γ	$\langle\tau_R^2\rangle$
S1	24.17	0.22	1315.45	0.29	0.21	22.41
S2	1.25	0.27	18.83	0.12	0.22	5.57
S3	0.66	0.32	4.61	0.05	0.28	0.62

The top and bottom panels of Fig. 5.8 illustrates the MSD for the three surfaces for waters within 5 Å and 10 Å respectively. The left and right panels instead, at each cutoff, shows the MSD for water molecules that have a residence time of 0.5 ns and 1 ns respectively at the

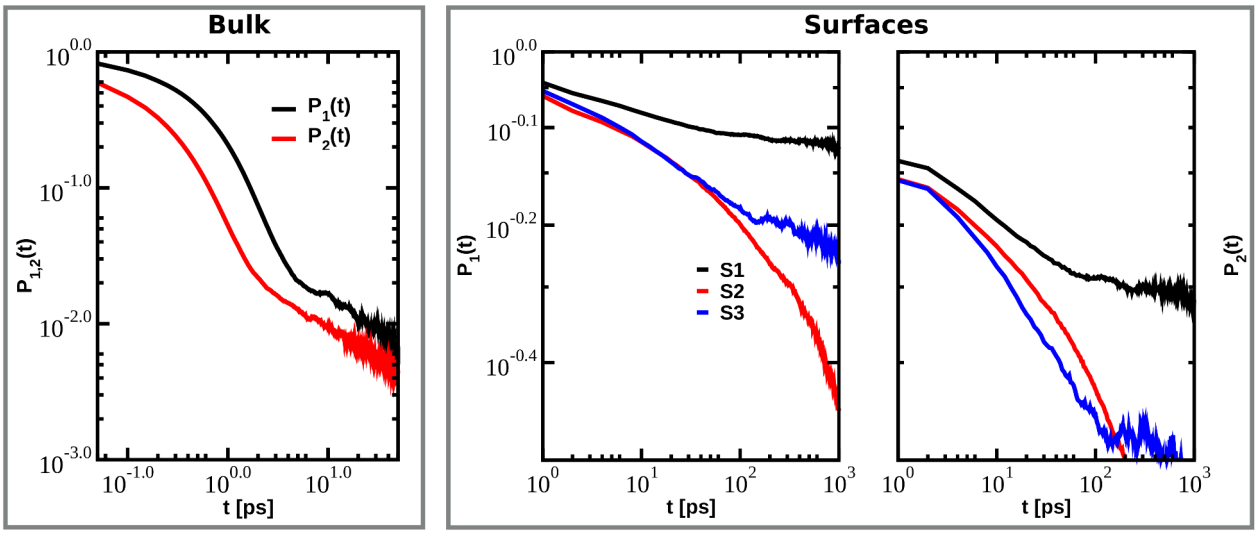

Fig. 5.9 The first and second rank dipolar relaxations of water molecules are plotted for water in bulk (left panel) and for water remain 100% of the observation time in the hydration shell of the three simulated surfaces (right panel).

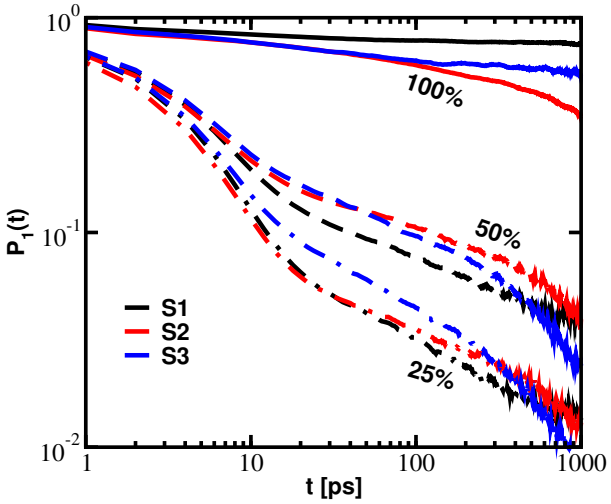

Fig. 5.10 First rank rotational correlation function of the three surfaces plotted as function of water residence time: 100% , 50% and 25% within the hydration shell of width 10 Å from the interface.

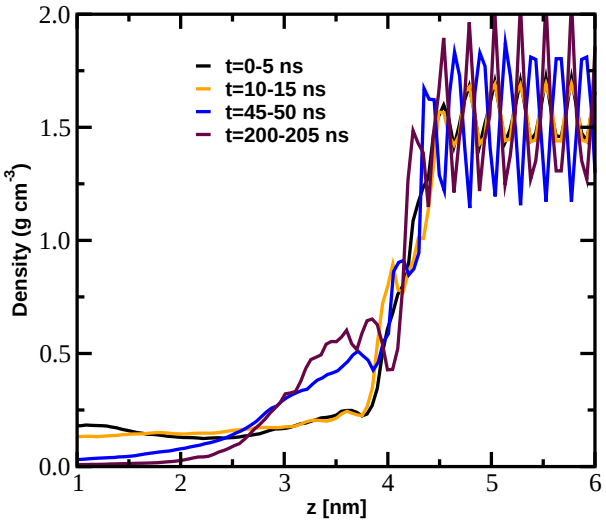

Fig. 5.11 The time evolution of the protein density near the interface is shown for the 1M concentrated solutions for a series of time-windows. Over time, we observe that the glutamine residues in solution migrate to the surface.

interface. As a guide to the eye, the horizontal dashed line shows the distance that a water molecule would diffuse corresponding to the length of a hydrogen bond (∼3 Å). Within each time-window of 0.5 ns or 1 ns, we also examined the dynamics for a larger population of waters by allowing for exchange dynamics within the prescribed cutoff. Thus, for each panel, we also show the MSD for water molecules residing 100%, 50% and 25% of the time.

The MSD for water molecules on each surface is quite different, with surface S3 exhibiting the fastest dynamics consistent with the residence times reported earlier. This feature holds for water molecules with 100% residency and then gets much less pronounced as one reduces the tolerance on the residency going from 50% to 25%. As one might expect, by focusing on a population of water molecules that remain for a longer time at the interface, we observe a more pronounced slow down in the dynamics (see the right panel of Fig.5.8). In the bottom panel, the analysis is repeated for water molecules within a larger cutoff from the interface. The overall trend observed is an enhancement in the MSD relative to the smaller cutoff. However, there is still a slow down in the dynamics at $\sim$ 1 nm compared to the bulk.

To obtain a more quantitative measure of the effect of each surface on the water dynamics, the MSD curves in Fig. 5.8 were fit to the following equation: $\langle r^2 \rangle \sim t^{\alpha}$ between 10 and 100 ps. Besides water molecules that reside 100% of the time, all other populations are characterized by diffusive dynamics with α coefficients close to 1. For the vast majority of the water molecules, for example those characterized by 50% residency, the slowdown in the diffusion constant is within a factor of 3 of bulk water. The small population of water

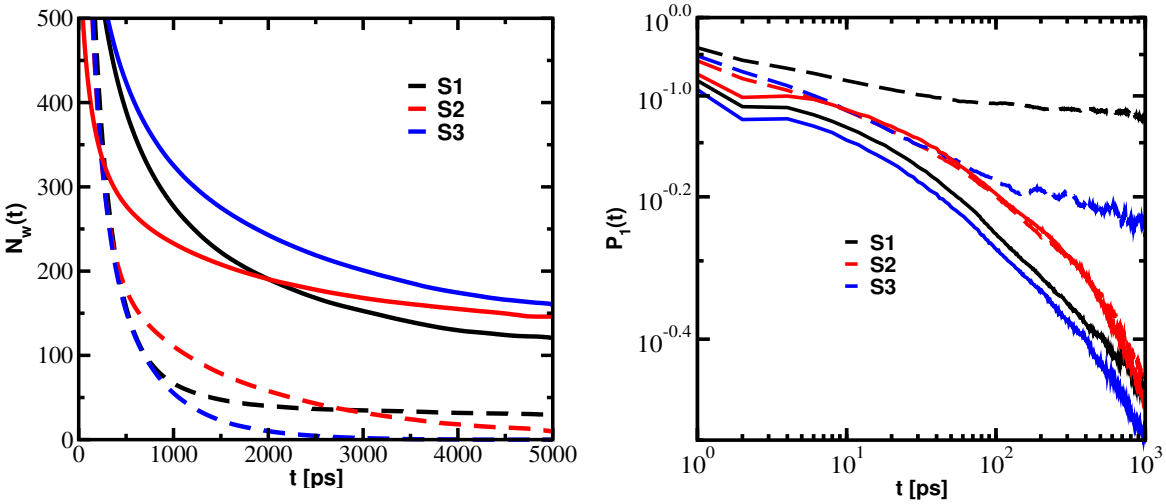

Fig. 5.12 The left and right panels compare the residence times and the $P_1(t)$ rotational correlation functions respectively of the surfaces in 1M concentrated solution (solid lines). The dashed lines correspond to those at 0M concentration.

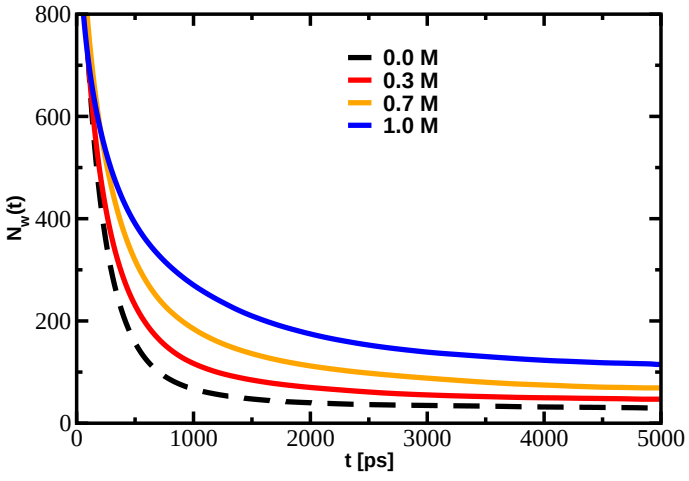

Fig. 5.13 The residence time of water molecules in the hydration shell of S1 surface is plotted as a function of varying concentration of the solvent from 0M to 1M.

Table 5.3 The number of water molecules residing in the hydration shell of width 0.5 nm from GDI of each system.

	0.5 *ns*			1 *ns*		
Systems	100%	50%	25%	100%	50%	25%
S1	5%	35%	78%	3%	23%	80%
S2	7%	27%	68%	5%	18%	72%
S3	5%	31%	70%	1%	22%	68%

molecules characterized by 100% residency over a timescale of less than 1 *ns*, on the other hand, feature a slowdown by an order of magnitude relative to the bulk. It should be stressed however, that this population water molecules make up only $\sim 3-4\%$ of the total ensemble consistent with previous studies [31]. In Table 5.3, we report the fraction of water molecules that remain within 5 Å from the GDI of each surface for 100% , 50% and 25% of the total simulation time. It is clear that for both the 0.5 and 1 *ns* time window, the fraction of water molecules experiencing a slow down

Besides structural perturbations, the orientational correlations of water as seen in Fig. 5.4 shows a substantial degree of polarization at all the interfaces. In order to investigate the effect of different surfaces on the rotational dynamics, we examined the first and second rank rotational correlation functions as done in previous studies [33, 191, 150, 162, 163]:

$$P_1(t) =< cos(\theta(t)) > \tag{5.5}$$

$$P_2(t) =< \frac{3}{2}cos^2(\theta(t)) - \frac{1}{2} > \tag{5.6}$$

Fig. 5.9 illustrates P_1 and P_2 time correlation functions plotted on a log-log scale where we focus on the analysis of water molecules in the bulk (left panel) and at the surfaces (right panel) that have 100% residency over a time period of up to 1 ns. Both P_1 and P_2 were fit to a single stretched exponential between 0 and 25 ps with the following functional form: $P_n(t) = exp(-(t/\tau_R^n)^\gamma)$. Table 5.2 summarizes the fitting parameters obtained along with the average time $\langle \tau_R^n \rangle$ associated with the dipole reorientation which was defined earlier.

The re-orientational dynamics of water near the three surfaces is remarkably different for each surface and also significantly slower than that compared to the bulk. In the case of

surface S1, the rotational dynamics of water occurs on a timescale of over 10's of nanoseconds which is due to the fact that water molecules are orientationally polarized at the interface as seen in Fig. 5.5. In order to determine the nature of the dipole reorientation better at the surface, we examined the ratio of the average reorientation time associated the first and second rank correlation functions. For all the three surfaces we see that this ratio is much larger than 3 (see Table 5.2) indicating that water molecules are undergoing hindered rotations in a cone [150]. Up to here we showed, the rotational relaxation of water near each of the three surfaces for those water molecules that reside 100% of the time during some chosen time window. Fig. 5.10 highlights the decay of rotational correlation function $P_1(t)$ as a function of water residence time. Different populations of water molecules with 100% , 50% and 25% residence time were taken within 10 Å distance from the GDI of each system. It is clear from the figure that the water dynamics undergoes faster rotational relaxation as more exchange events are allowed.

5.3.3 Implications on Crystal Growth

It is beyond the scope of the current work to study the nucleation thermodynamics and underlying mechanisms associated with the growth of our three surfaces. In a recent study, Salvalaglio and co-workers used molecular dynamics simulations to study the growth of a paradigmatic system urea [173]. They found that by increasing the concentration of urea molecules in the bulk, they were able to study the incorporation of urea molecules on the crystalline surfaces and therefore examine the initial stages of surface growth.

The preceding results of the bare crystal surfaces show that they are all very hydrophilic and that there is a significant retardation in the translational and re-orientational dynamics of water at the interface. It is clear from the water densities in Fig. 5.2, that all the three surfaces, are characterized by structured water. In order to incorporate glutamine molecules at the interface, fluctuations along the solvent degree of freedom will very likely be needed. Furthermore, in one of the surfaces illustrated in Fig. 5.5 we observe rotationally arrested water molecules on very long time scales. It is thus interesting to examine, how glutamine molecules in the bulk would be incorporated onto the crystal surface.

We focus the analysis on the simulations conducted at the highest concentration of 1M. Fig. 5.11 shows the time evolution of the glutamine densities at the interface which shows that the free glutamine molecules in the bulk appear to move to the interfacial region interacting with the original pristine surface. A visual inspection of the trajectories indicated that the strongly hydrophilic nature of glutamine as well as that of the original surface results in the formation of glutamine clusters with water molecules sandwiched between.

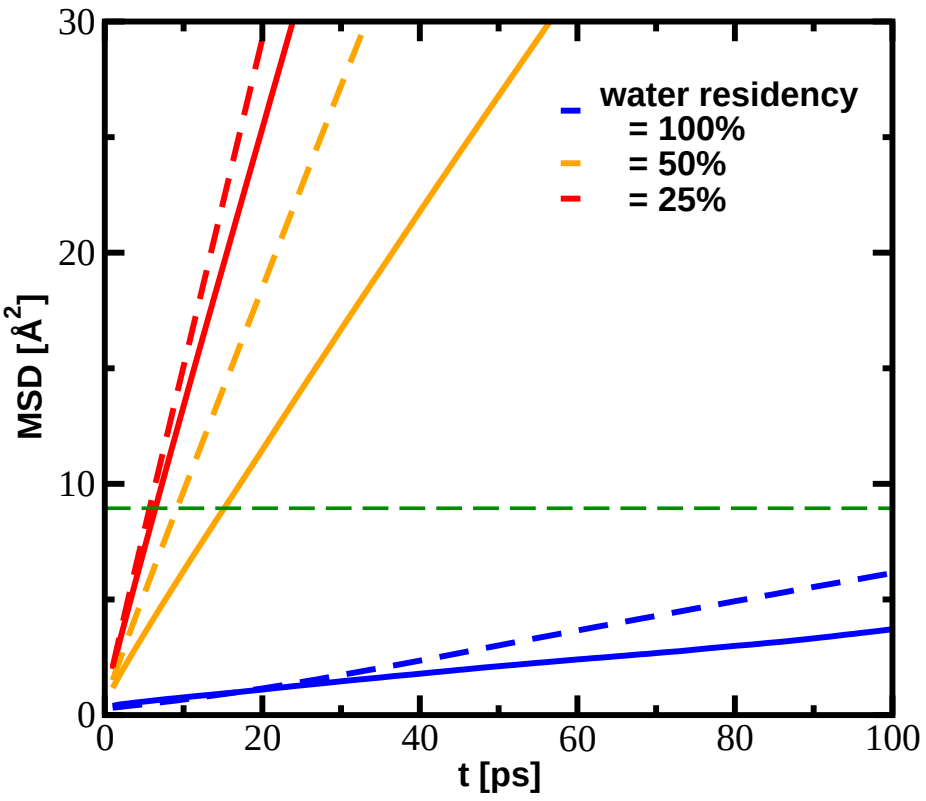

Fig. 5.14 The MSD of water molecules within 5 Å from the GDI of S1. The solid lines illustrates the MSD of the molecules of 1M solution while dashed lines correspond to those at 0M.

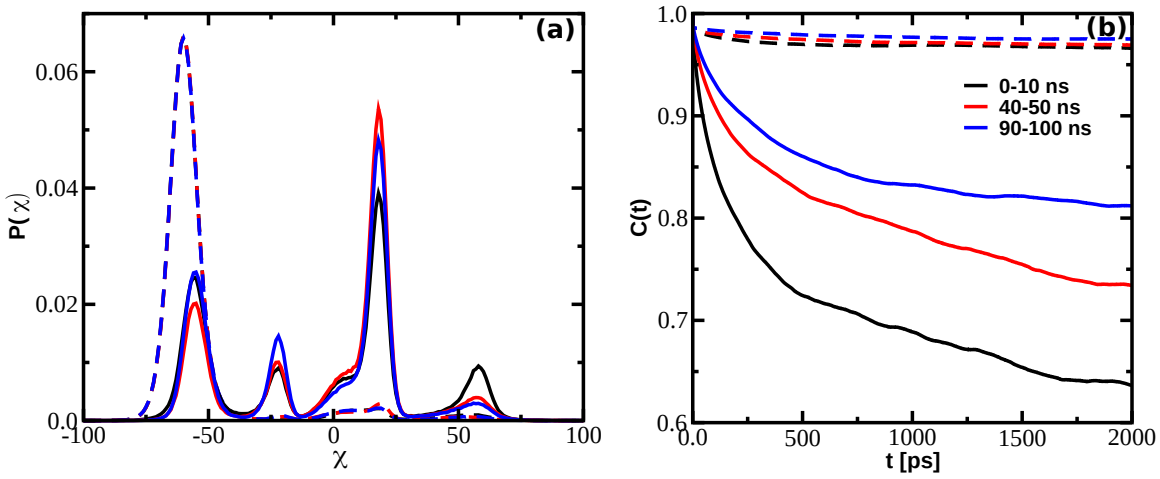

Fig. 5.15 Time resolved average dihedral distributions (panel a)) and auto time correlation functions (panel b)) are plotted for the glutamine residues of system S1. The dashed lines represents the residues belongs to the crystalline surface while the solid line highlights the residues in the solution.

The left and right panels of Fig. 5.12 compares the residence times and the $P_1(t)$ rotational correlation functions respectively obtained for the 1M simulations. The analysis was focused on the last part of the simulation once a significant fraction of glutamine molecules had attached to the surface. Upon binding to the surface, water molecules that are dragged by the glutamine molecules as well as those that were originally there, appear to get trapped. This is seen clearly in the residence time correlation functions which significantly slows down at all the three interfaces reflecting a layer of water that takes a long time to exchange with the bulk since they live in a crowded environment. For more clarity, in Fig. 5.13 residence time of water is plotted for surface S1 as function of glutamine concentration in the solvent varying from 0-1M. The time for this analysis was chosen after 200 ns where most of the glutanime residues already migrated to the surface. The population of the solutes makes a rough jelly like surface. The hydration water gets trapped and its exchanged dynamics get slowdown as compared to the pristine surface.

The water molecules that get trapped at the interface are distinct in their rotational dynamics compared to those at the pristine surfaces. We see in the right panel of Fig. 5.12 that the relaxation dynamics associated with $P_1(t)$ occurs on a much faster timescale. This is due to the fact that the waters that are trapped at the interface in the crowded environment, aren't necessarily pinned to the surface as seen in Fig. 5.5 and hence they are able to move around more freely. As a reference, the fraction of water molecules that reside at the surface for 100% of the time within a 5 Å cutoff correspond to $\sim$12% of the total population.

The slow down of water near the surface due to the crowded environment that occur in the first steps of nucleation is also reflected in the rightmost panel of Fig. 5.14 which shows the mean square displacement of water molecules diffusing within 5 Å from the GDI of S1. An overall slowdown in translational dynamics of water molecules is observed when compared to pristine surfaces (dashed lines in Fig. 5.14).

Although our simulations indicate that glutamine molecules migrate to the interfacial region as seen in Fig. 5.11, we do not observe any successful events involving the growth of the crystal surface. We cannot make any quantitative claims from this on the thermodynamics of crystal growth. However, the preceding analysis suggests that the solvent dynamics trapped at the interface, likely impedes nucleation. The thermodynamics and dynamics of crystal growth will obviously involve a coupling of both solvent and solute degrees of freedom.

The glutamine molecules that move towards the interface form hydrogen bond networks between themselves which results also in a slow down in their conformational dynamics. Furthermore, the conformations that they adopt are also distinct from those required for successful nucleation. This is seen more clearly in the left panel of Fig. 5.15 which illustrates

the distribution of the dihedral angle associated with the glutamine side chain carbon atoms, computed for glutamine molecules in the crystal as well as those that form glutamine clusters over the course of forming a crowded environment at the interface. We see clearly that the typical dihedral angle associated with the side chains in the crystal are peaked at -60° while those in the clusters at the interfaces have conformations that populate very different conformations than those required to be incorporated onto the crystal surface. The crowded environment of the interface is also reflected in the dynamics of the glutamine molecules. The right panel of Fig. 5.15 shows the relaxation dynamics of the same dihedral angle, once again for molecules in the crystal as well as those at the interface. Over time, the relaxation dynamics of the glutamine molecules slow down. Interestingly, the timescales associated with the residence times of water molecules shown in Fig. 5.12 overlap with those involving conformational changes of the dihedral angles of the glutamine molecules.

5.4 Conclusion and Summary

The physical properties of water near organic and inorganic interfaces continues to pose interesting challenges and questions for both experimentalists and theoreticians alike. There have been numerous theoretical and computational efforts to characterize the extent of the slow down of water near soft-matter biological systems such as proteins and DNA. How much these effects extend to solid-organic surfaces such as amino-acid crystal interfaces has not been investigated.

In this work, we performed classical molecular dynamics simulations of three surfaces associated with crystalline L-glutamine. In particular, we compare and contrast the structural and dynamical properties of the three glutamine surfaces: 100, 010 and 001. All the three interfaces are characterized by a structured layer of water involving orientationally polarized water at the surface which is unique for each surface and modulated by the relative positioning of positive and negatively charged groups of the glutamine molecules in contact with the liquid.

The highly hydrophilic surfaces exert a strong field on the water molecules which slows down their dynamics. In particular, we demonstrate that the diffusion constant of water near the surface is reduced by a factor of $\sim$3. Interestingly, on one of the surfaces, water molecules can get embedded into the surface crystal structure and remain trapped for timescales of 10's of nanoseconds.

To assess the implications of our results on crystal nucleation, we also determine the translational and rotational dynamics of water near interfaces where glutamine molecules from the bulk form part of the structured layer. This may resemble conditions that are

generated during crystal nucleation. The important suggestion from our findings is that the water dynamics in these crowded environments changes quite significantly and will likely have effects in the growth of surfaces. Furthermore, we also show that there is a slow down in the conformational fluctuations of the glutamine molecules at the surface. In the future it would be interesting to understand better the role of water in the nucleation mechanism as well as how this changes depending on the chemistry associated with the amino acid.

Chapter 6

Summary

Non-aromatic intrinsic fluorescence in protein crystals and aggregates is observed for the first time in 2004 by Shukla et al [53]. After this observation, many experimental reports confirm similar photo phenomenon in different protein aggregates, particularly those which contain a rich proportion of beta-sheets. Most notable among these systems are the Amyloid aggregates, which are involved in neurodegenerative disorders such as Alzheimer and Parkinson [16–20]. The emission of this kind occur in the visible range, and it is independent of the aromatic residues. As we mentioned in Chapter 1, different previous reports suggest different hypothesis on the origins of this fluorescence [58, 59, 56, 57] The real understanding of this phenomenon in complex molecular systems remains elusive.

In collaboration with Kaminski lab in Cambridge, where the experiments showed that the non-aromatic single amino acid glutamine aggregates show fluorescence during their aggregation, which is similar to amyloid. We took the first step to perform the theoretical spectroscopy on the single amino acid glutamine aggregates by applying a multi-scale computational approach.
In Chapter 3, we computed the ground and excited-state properties of three different glutamine systems where we show that the system with short hydrogen bonds absorb at lower energies and exhibit a rich feature in the optical spectra. The low energy electronic excitations in this system involve collective charge reorganisation over several parts of the crystal structure. We have highlighted the effects of thermal fluctuations and show that in the new system, the SHB permits proton transfer which is characterised by an asymmetric double-well potential. This feature is absent for other systems where hydrogen bond length is longer than 2.7 Å. The effects of explicit solvent environments were investigated, which show similar trends in optical absorption for the three systems. Finally, at the end of this chapter, the role of vibrational modes upon excitation were investigated, and we conclude

that the optical properties of the glutamine crystals sensitively tuned by collective vibrational modes.

The glutamine aggregates are differ in terms of their hydrogen bond network. In Chapter 4, we used classical and quantum methods to dissect in details the structure, dynamics and electronic properties of hydrogen bonds network of these systems. We show that the quantum effect modulates a lot the structural and chemical features of strong hydrogen bonds. In future, it is interesting to investigate the role of quantum effects on optical properties of these systems.

The aggregation of glutamine systems occur in aqueous solution, one of the focus of my thesis was to investigate their coupling with the surrounding water. There have been numerous efforts both on theoretical and computational sides to characterise the extent over which water gets slowed near proteins and DNA [31]. How this behaviour extends to solid-organic interfaces such as amino-acid crystal surfaces has not been investigated.
In Chapter 5, we try to answer this question by performing large scale molecular dynamics simulations for different glutamine surfaces. The stability of these highly hydrophilic surfaces serves as excellent model systems for investigating the behaviour of water at the interface. We showed that at each surface, water displays the characteristic difference in its structure, orientation and dynamics.
Since in the last decade, there have been several advances in surface-specific spectroscopy such as sum-frequency generation (SFG). These experimental techniques are allowing for the investigation of the dynamics of water at the complex aqueous interfaces. Our work will motivate experiments like these on crystal amino-acid interfaces as these are clean systems where one does not have to deal with the soft modes of the protein.
In the end, we also investigate the effect of crowded environment on water dynamics by simulating the surfaces in supersaturated conditions. We show that the binding of the glutamine residues at the interface involves the pockets of trapped water molecules. The crowdy environment changes the water dynamics in a highly non-trivial manner. The insight intended from these simulations suggests that the solvent dynamics may have important implications on crystal nucleation.
In the future, it would be interesting to understand better the role of water in the nucleation mechanism as well as how these changes depend on the chemistry associated with the amino acid.

References

[1] Clara Iannuzzi, Gaetano Irace, and Ivana Sirangelo. Differential effects of glycation on protein aggregation and amyloid formation. *Frontiers in molecular biosciences*, 1:9, 2014.

[2] Jevgenij A Raskatov and David B Teplow. Using chirality to probe the conformational dynamics and assembly of intrinsically disordered amyloid proteins. *Scientific reports*, 7(1):12433, 2017.

[3] Quantitation of peptides and amino acids with a synergy tm ht using uv fluorescence. 2006.

[4] Fiona TS Chan, Dorothea Pinotsi, S Gabriele, Kaminski Schierle, and Clemens F Kaminski. Structure-specific intrinsic fluorescence of protein amyloids used to study their kinetics of aggregation. In *Bio-nanoimaging*, pages 147–155. Elsevier, 2014.

[5] W Cochran and Bruce R Penfold. The crystal structure of l-glutamine. *Acta Crystallographica*, 5(5):644–653, 1952.

[6] E Van Zoeren, HAJ Oonk, and J Kroon. X-ray analysis of l-pyroglutamic acid. a marked case of structural pseudosymmetry. *Acta Crystallographica Section B: Structural Crystallography and Crystal Chemistry*, 34(6):1898–1900, 1978.

[7] George M Whitesides, John P Mathias, and Christopher T Seto. Molecular self-assembly and nanochemistry: a chemical strategy for the synthesis of nanostructures. *Science*, 254(5036):1312–1319, 1991.

[8] Hossein Hosseinkhani, Po-Da Hong, and Dah-Shyong Yu. Self-assembled proteins and peptides for regenerative medicine. *Chemical reviews*, 113(7):4837–4861, 2013.

[9] David J Huggins, May Marsh, and Mike C Payne. Thermodynamic properties of water molecules at a protein–protein interaction surface. *Journal of chemical theory and computation*, 7(11):3514–3522, 2011.

[10] Caroline Duval-Terrié, Jovenka Huguet, and Guy Muller. Self-assembly and hydrophobic clusters of amphiphilic polysaccharides. *Colloids and Surfaces A: Physicochemical and Engineering Aspects*, 220(1-3):105–115, 2003.

[11] Alexandre Tkatchenko, Mariana Rossi, Volker Blum, Joel Ireta, and Matthias Scheffler. Unraveling the stability of polypeptide helices: Critical role of van der waals interactions. *Physical review letters*, 106(11):118102, 2011.

[12] Mariana Rossi, Wei Fang, and Angelos Michaelides. Stability of complex biomolecular structures: Van der waals, hydrogen bond cooperativity, and nuclear quantum effects. *The journal of physical chemistry letters*, 6(21):4233–4238, 2015.

[13] Peter M Steinert. Structure, function, and dynamics of keratin intermediate filaments. *Journal of Investigative Dermatology*, 100(6):729–734, 1993.

[14] Richard Maynes. *Structure and function of collagen types*. Elsevier, 2012.

[15] Daiki Tsukamoto, Isao Sarashina, and Kazuyoshi Endo. Structure and expression of an unusually acidic matrix protein of pearl oyster shells. *Biochemical and biophysical research communications*, 320(4):1175–1180, 2004.

[16] Christopher M Dobson. Protein misfolding, evolution and disease. *Trends in biochemical sciences*, 24(9):329–332, 1999.

[17] Jean-Christophe Rochet and Peter T Lansbury Jr. Amyloid fibrillogenesis: themes and variations. *Current opinion in structural biology*, 10(1):60–68, 2000.

[18] Christopher A Ross and Michelle A Poirier. Protein aggregation and neurodegenerative disease. *Nature medicine*, 10(7s):S10, 2004.

[19] Anthony L Fink. Protein aggregation: folding aggregates, inclusion bodies and amyloid. *Folding and design*, 3(1):R9–R23, 1998.

[20] Christopher M Dobson. Protein folding and misfolding. *Nature*, 426(6968):884, 2003.

[21] Jean D Sipe and Alan S Cohen. History of the amyloid fibril. *Journal of structural biology*, 130(2-3):88–98, 2000.

[22] John Hardy and Dennis J Selkoe. The amyloid hypothesis of alzheimer's disease: progress and problems on the road to therapeutics. *science*, 297(5580):353–356, 2002.

[23] Dennis J Selkoe and John Hardy. The amyloid hypothesis of alzheimer's disease at 25 years. *EMBO molecular medicine*, 8(6):595–608, 2016.

[24] Adriano Aguzzi, Christina Sigurdson, and Mathias Heikenwaelder. Molecular mechanisms of prion pathogenesis. *Annu. Rev. pathmechdis. Mech. Dis.*, 3:11–40, 2008.

[25] Louise C Serpell. Alzheimer's amyloid fibrils: structure and assembly. *Biochimica et Biophysica Acta (BBA)-Molecular Basis of Disease*, 1502(1):16–30, 2000.

[26] Rebecca Nelson, Michael R Sawaya, Melinda Balbirnie, Anders Ø Madsen, Christian Riekel, Robert Grothe, and David Eisenberg. Structure of the cross-β spine of amyloid-like fibrils. *Nature*, 435(7043):773, 2005.

[27] Anthony WP Fitzpatrick, Galia T Debelouchina, Marvin J Bayro, Daniel K Clare, Marc A Caporini, Vikram S Bajaj, Christopher P Jaroniec, Luchun Wang, Vladimir Ladizhansky, Shirley A Müller, et al. Atomic structure and hierarchical assembly of a cross-β amyloid fibril. *Proceedings of the National Academy of Sciences*, 110(14):5468–5473, 2013.

[28] Bertil Halle. Protein hydration dynamics in solution: a critical survey. *Philosophical Transactions of the Royal Society of London. Series B: Biological Sciences*, 359(1448):1207–1224, 2004.

[29] Masayoshi Nakasako. Water–protein interactions from high–resolution protein crystallography. *Philosophical Transactions of the Royal Society of London. Series B: Biological Sciences*, 359(1448):1191–1206, 2004.

[30] Marie-Claire Bellissent-Funel, Ali Hassanali, Martina Havenith, Richard Henchman, Peter Pohl, Fabio Sterpone, David van der Spoel, Yao Xu, and Angel E Garcia. Water determines the structure and dynamics of proteins. *Chemical Reviews*, 116(13):7673–7697, 2016.

[31] Damien Laage, Thomas Elsaesser, and James T Hynes. Water dynamics in the hydration shells of biomolecules. *Chemical reviews*, 117(16):10694–10725, 2017.

[32] Anna Rita Bizzarri and Salvatore Cannistraro. Molecular dynamics of water at the protein- solvent interface, 2002.

[33] Massimo Marchi, Fabio Sterpone, and Matteo Ceccarelli. Water rotational relaxation and diffusion in hydrated lysozyme. *Journal of the American Chemical Society*, 124(23):6787–6791, 2002.

[34] Katrin Amann-Winkel, Marie-Claire Bellissent-Funel, Livia E Bove, Thomas Loerting, Anders Nilsson, Alessandro Paciaroni, Daniel Schlesinger, and Lawrie Skinner. X-ray and neutron scattering of water. *Chemical reviews*, 116(13):7570–7589, 2016.

[35] Robert H Pearson and Irmin Pascher. The molecular structure of lecithin dihydrate. *Nature*, 281(5731):499, 1979.

[36] H Frauenfelder, PW Fenimore, G Chen, and BH McMahon. Protein folding is slaved to solvent motions. *Proceedings of the National Academy of Sciences*, 103(42):15469–15472, 2006.

[37] Paul W Fenimore, Hans Frauenfelder, Benjamin H McMahon, and Fritz G Parak. Slaving: solvent fluctuations dominate protein dynamics and functions. *Proceedings of the National Academy of Sciences*, 99(25):16047–16051, 2002.

[38] Nilashis Nandi, Kankan Bhattacharyya, and Biman Bagchi. Dielectric relaxation and solvation dynamics of water in complex chemical and biological systems. *Chemical Reviews*, 100(6):2013–2046, 2000.

[39] Fabio Sterpone, Matteo Ceccarelli, and Massimo Marchi. Dynamics of hydration in hen egg white lysozyme1. *Journal of molecular biology*, 311(2):409–419, 2001.

[40] Maria L Saviotti and William C Galley. Room temperature phosphorescence and the dynamic aspects of protein structure. *Proceedings of the National Academy of Sciences*, 71(10):4154–4158, 1974.

[41] Joseph R Lakowicz. *Principles of fluorescence spectroscopy*. Springer Science & Business Media, 2013.

[42] Maurice R Eftink and Camillo A Ghiron. Fluorescence quenching studies with proteins. *Analytical biochemistry*, 114(2):199–227, 1981.

[43] Larissa A Munishkina and Anthony L Fink. Fluorescence as a method to reveal structures and membrane-interactions of amyloidogenic proteins. *Biochimica et Biophysica Acta (BBA)-Biomembranes*, 1768(8):1862–1885, 2007.

[44] Hans Kuhn. A quantum-mechanical theory of light absorption of organic dyes and similar compounds. *The Journal of chemical physics*, 17(12):1198–1212, 1949.

[45] M Gabriela Lagorio, Gabriela B Cordon, and Analia Iriel. Reviewing the relevance of fluorescence in biological systems. *Photochemical & Photobiological Sciences*, 14(9):1538–1559, 2015.

[46] EA Burstein, NS Vedenkina, and MN Ivkova. Fluorescence and the location of tryptophan residues in protein molecules. *Photochemistry and photobiology*, 18(4):263–279, 1973.

[47] Joseph M Beechem and Ludwig Brand. Time-resolved fluorescence of proteins. *Annual review of biochemistry*, 54(1):43–71, 1985.

[48] Roger Y Tsien. The green fluorescent protein, 1998.

[49] Douglas C Prasher, Virginia K Eckenrode, William W Ward, Frank G Prendergast, and Milton J Cormier. Primary structure of the aequorea victoria green-fluorescent protein. *Gene*, 111(2):229–233, 1992.

[50] Marc Zimmer. Green fluorescent protein (gfp): applications, structure, and related photophysical behavior. *Chemical reviews*, 102(3):759–782, 2002.

[51] George H Patterson, Susan M Knobel, Wallace D Sharif, Steven R Kain, and David W Piston. Use of the green fluorescent protein and its mutants in quantitative fluorescence microscopy. *Biophysical journal*, 73(5):2782–2790, 1997.

[52] Atsushi Miyawaki and Roger Y Tsien. Monitoring protein conformations and interactions by fluorescence resonance energy transfer between mutants of green fluorescent protein. In *Methods in enzymology*, volume 327, pages 472–500. Elsevier, 2000.

[53] Anshuman Shukla, Sourav Mukherjee, Swati Sharma, Vishal Agrawal, KV Radha Kishan, and Purnananda Guptasarma. A novel uv laser-induced visible blue radiation from protein crystals and aggregates: scattering artifacts or fluorescence transitions of peptide electrons delocalized through hydrogen bonding? *Archives of biochemistry and biophysics*, 428(2):144–153, 2004.

[54] Fiona TS Chan, Gabriele S Kaminski Schierle, Janet R Kumita, Carlos W Bertoncini, Christopher M Dobson, and Clemens F Kaminski. Protein amyloids develop an intrinsic fluorescence signature during aggregation. *Analyst*, 138(7):2156–2162, 2013.

[55] Dorothea Pinotsi, Alexander K Buell, Christopher M Dobson, Gabriele S Kaminski Schierle, and Clemens F Kaminski. A label-free, quantitative assay of amyloid fibril growth based on intrinsic fluorescence. *ChemBioChem*, 14(7):846–850, 2013.

[56] Loretta Laureana Del Mercato, Pier Paolo Pompa, Giuseppe Maruccio, Antonio Della Torre, Stefania Sabella, Antonio Mario Tamburro, Roberto Cingolani, and Ross Rinaldi. Charge transport and intrinsic fluorescence in amyloid-like fibrils. *Proceedings of the National Academy of Sciences*, 104(46):18019–18024, 2007.

[57] Dorothea Pinotsi, Luca Grisanti, Pierre Mahou, Ralph Gebauer, Clemens F Kaminski, Ali Hassanali, and Gabriele S Kaminski Schierle. Proton transfer and structure-specific fluorescence in hydrogen bond-rich protein structures. *Journal of the American Chemical Society*, 138(9):3046–3057, 2016.

[58] L Homchaudhuri and R Swaminathan. Novel absorption and fluorescence characteristics of l-lysine. *Chemistry Letters*, 30(8):844–845, 2001.

[59] Ruquan Ye, Yuanyue Liu, Haoke Zhang, Huifang Su, Yilin Zhang, Liguo Xu, Rongrong Hu, Ryan TK Kwok, Kam Sing Wong, Jacky WY Lam, et al. Non-conventional fluorescent biogenic and synthetic polymers without aromatic rings. *Polymer Chemistry*, 8(10):1722–1727, 2017.

[60] Jay W Ponder and David A Case. Force fields for protein simulations. In *Advances in protein chemistry*, volume 66, pages 27–85. Elsevier, 2003.

[61] Kresten Lindorff-Larsen, Stefano Piana, Kim Palmo, Paul Maragakis, John L Klepeis, Ron O Dror, and David E Shaw. Improved side-chain torsion potentials for the amber ff99sb protein force field. *Proteins: Structure, Function, and Bioinformatics*, 78(8):1950–1958, 2010.

[62] Alexander D MacKerell Jr, Nilesh Banavali, and Nicolas Foloppe. Development and current status of the charmm force field for nucleic acids. *Biopolymers: Original Research on Biomolecules*, 56(4):257–265, 2000.

[63] George A Kaminski, Richard A Friesner, Julian Tirado-Rives, and William L Jorgensen. Evaluation and reparametrization of the opls-aa force field for proteins via comparison with accurate quantum chemical calculations on peptides. *The Journal of Physical Chemistry B*, 105(28):6474–6487, 2001.

[64] Loup Verlet. Computer" experiments" on classical fluids. i. thermodynamical properties of lennard-jones molecules. *Physical review*, 159(1):98, 1967.

[65] William C Swope, Hans C Andersen, Peter H Berens, and Kent R Wilson. A computer simulation method for the calculation of equilibrium constants for the formation of physical clusters of molecules: Application to small water clusters. *The Journal of Chemical Physics*, 76(1):637–649, 1982.

[66] Pierre Hohenberg and Walter Kohn. Inhomogeneous electron gas. *Physical review*, 136(3B):B864, 1964.

[67] Walter Kohn and Lu Jeu Sham. Self-consistent equations including exchange and correlation effects. *Physical review*, 140(4A):A1133, 1965.

[68] Axel D Becke. Density-functional exchange-energy approximation with correct asymptotic behavior. *Physical review A*, 38(6):3098, 1988.

[69] John P Perdew and Yue Wang. Accurate and simple analytic representation of the electron-gas correlation energy. *Physical Review B*, 45(23):13244, 1992.

[70] John P Perdew, Kieron Burke, and Matthias Ernzerhof. Generalized gradient approximation made simple. *Physical review letters*, 77(18):3865, 1996.

[71] Aron J Cohen, Paula Mori-Sánchez, and Weitao Yang. Challenges for density functional theory. *Chemical reviews*, 112(1):289–320, 2011.

[72] Axel D Becke. A new mixing of hartree–fock and local density-functional theories. *The Journal of chemical physics*, 98(2):1372–1377, 1993.

[73] Philip J Stephens, FJ Devlin, CFN Chabalowski, and Michael J Frisch. Ab initio calculation of vibrational absorption and circular dichroism spectra using density functional force fields. *The Journal of physical chemistry*, 98(45):11623–11627, 1994.

[74] Takeshi Yanai, David P Tew, and Nicholas C Handy. A new hybrid exchange–correlation functional using the coulomb-attenuating method (cam-b3lyp). *Chemical Physics Letters*, 393(1-3):51–57, 2004.

[75] Jeng-Da Chai and Martin Head-Gordon. Long-range corrected hybrid density functionals with damped atom–atom dispersion corrections. *Physical Chemistry Chemical Physics*, 10(44):6615–6620, 2008.

[76] Erich Runge and Eberhard KU Gross. Density-functional theory for time-dependent systems. *Physical Review Letters*, 52(12):997, 1984.

[77] Richard Phillips Feynman. Space-time approach to non-relativistic quantum mechanics. In *Feynman's Thesis—A New Approach To Quantum Theory*, pages 71–109. World Scientific, 2005.

[78] RP Feynman and AR Hibbs Quantum Mechanics. Path integrals. *Lecture Notes Phys*, 106, 1979.

[79] Joseph A Morrone and Roberto Car. Nuclear quantum effects in water. *Physical review letters*, 101(1):017801, 2008.

[80] CJ Burnham, GF Reiter, J Mayers, T Abdul-Redah, H Reichert, and H Dosch. On the origin of the redshift of the oh stretch in ice ih: evidence from the momentum distribution of the protons and the infrared spectral density. *Physical Chemistry Chemical Physics*, 8(34):3966–3977, 2006.

[81] Michele Ceriotti, Joshua More, and David E Manolopoulos. i-pi: A python interface for ab initio path integral molecular dynamics simulations. *Computer Physics Communications*, 185(3):1019–1026, 2014.

[82] Michele Ceriotti, Giovanni Bussi, and Michele Parrinello. Colored-noise thermostats à la carte. *Journal of Chemical Theory and Computation*, 6(4):1170–1180, 2010.

[83] Lihi Adler-Abramovich, Daniel Aronov, Peter Beker, Maya Yevnin, Shiri Stempler, Ludmila Buzhansky, Gil Rosenman, and Ehud Gazit. Self-assembled arrays of peptide nanotubes by vapour deposition. *Nature nanotechnology*, 4(12):849, 2009.

[84] Lihi Adler-Abramovich and Ehud Gazit. Correction: The physical properties of supramolecular peptide assemblies: from building block association to technological applications. *Chemical Society Reviews*, 43(20):7236–7236, 2014.

[85] Lihi Adler-Abramovich, Meital Reches, Victoria L Sedman, Stephanie Allen, Saul JB Tendler, and Ehud Gazit. Thermal and chemical stability of diphenylalanine peptide nanotubes: implications for nanotechnological applications. *Langmuir*, 22(3):1313–1320, 2006.

[86] Tatiana N Tikhonova, Nataliya R Rovnyagina, Alexander Ya Zherebker, Nikolai N Sluchanko, Anna A Rubekina, Anton S Orekhov, Eugene N Nikolaev, Victor V Fadeev, Vladimir N Uversky, and Evgeny A Shirshin. Dissection of the deep-blue autofluorescence changes accompanying amyloid fibrillation. *Archives of biochemistry and biophysics*, 651:13–20, 2018.

[87] Hiroshi Mori, K Takio, M Ogawara, and DJ Selkoe. Mass spectrometry of purified amyloid beta protein in alzheimer's disease. *Journal of Biological Chemistry*, 267(24):17082–17086, 1992.

[88] John D Head and Michael C Zerner. A broyden—fletcher—goldfarb—shanno optimization procedure for molecular geometries. *Chemical physics letters*, 122(3):264–270, 1985.

[89] Joost VandeVondele, Matthias Krack, Fawzi Mohamed, Michele Parrinello, Thomas Chassaing, and Jürg Hutter. Quickstep: Fast and accurate density functional calculations using a mixed gaussian and plane waves approach. *Computer Physics Communications*, 167(2):103–128, 2005.

[90] S Goedecker, M Teter, and Jürg Hutter. Separable dual-space gaussian pseudopotentials. *Physical Review B*, 54(3):1703, 1996.

[91] Stefan Grimme, Jens Antony, Stephan Ehrlich, and Helge Krieg. A consistent and accurate ab initio parametrization of density functional dispersion correction (dft-d) for the 94 elements h-pu. *The Journal of chemical physics*, 132(15):154104, 2010.

[92] Giovanni Bussi, Davide Donadio, and Michele Parrinello. Canonical sampling through velocity rescaling. *The Journal of chemical physics*, 126(1):014101, 2007.

[93] Paolo Giannozzi, Oliviero Andreussi, Thomas Brumme, Oana Bunau, M Buongiorno Nardelli, Matteo Calandra, Roberto Car, Carlo Cavazzoni, Davide Ceresoli, Matteo Cococcioni, et al. Advanced capabilities for materials modelling with quantum espresso. *Journal of Physics: Condensed Matter*, 29(46):465901, 2017.

[94] Dario Rocca, Ralph Gebauer, Yousef Saad, and Stefano Baroni. Turbo charging time-dependent density-functional theory with lanczos chains. *The Journal of chemical physics*, 128(15):154105, 2008.

[95] Osman Barış Malcıoğlu, Ralph Gebauer, Dario Rocca, and Stefano Baroni. turbotddft–a code for the simulation of molecular spectra using the liouville–lanczos approach to time-dependent density-functional perturbation theory. *Computer Physics Communications*, 182(8):1744–1754, 2011.

[96] Norman Troullier and José Luís Martins. Efficient pseudopotentials for plane-wave calculations. *Physical review B*, 43(3):1993, 1991.

[97] MJ Frisch, GW Trucks, HB Schlegel, GE Scuseria, MA Robb, JR Cheeseman, G Scalmani, V Barone, GA Petersson, H Nakatsuji, et al. Gaussian 16. *Revision A*, 3, 2016.

[98] Marcus Fändrich and Christopher M Dobson. The behaviour of polyamino acids reveals an inverse side chain effect in amyloid structure formation. *The EMBO journal*, 21(21):5682–5690, 2002.

[99] Magali Benoit, Dominik Marx, and Michele Parrinello. Tunnelling and zero-point motion in high-pressure ice. *Nature*, 392(6673):258, 1998.

[100] I Mandal, S Paul, and R Venkatramani. Optical backbone-sidechain charge transfer transitions in proteins sensitive to secondary structure and modifications. *Faraday discussions*, 207:115–135, 2018.

[101] Dominik Marx, Amalendu Chandra, and Mark E Tuckerman. Aqueous basic solutions: hydroxide solvation, structural diffusion, and comparison to the hydrated proton. *Chemical Reviews*, 110(4):2174–2216, 2010.

[102] Lu Wang, Stephen D Fried, Steven G Boxer, and Thomas E Markland. Quantum delocalization of protons in the hydrogen-bond network of an enzyme active site. *Proceedings of the National Academy of Sciences*, 111(52):18454–18459, 2014.

[103] M Jocelyn Cox, Rutger LA Timmer, Huib J Bakker, Soohyung Park, and Noam Agmon. Distance-dependent proton transfer along water wires connecting acid- base pairs. *The Journal of Physical Chemistry A*, 113(24):6599–6606, 2009.

[104] BJ Siwick, MJ Cox, and HJ Bakker. Long-range proton transfer in aqueous acid- base reactions. *The Journal of Physical Chemistry B*, 112(2):378–389, 2008.

[105] Matteo Rini, Ben-Zion Magnes, Ehud Pines, and Erik TJ Nibbering. Real-time observation of bimodal proton transfer in acid-base pairs in water. *Science*, 301(5631):349–352, 2003.

[106] Chong Fang, Renee R Frontiera, Rosalie Tran, and Richard A Mathies. Mapping gfp structure evolution during proton transfer with femtosecond raman spectroscopy. *Nature*, 462(7270):200, 2009.

[107] W Wallace Cleland, Perry A Frey, and John A Gerlt. The low barrier hydrogen bond in enzymatic catalysis. *Journal of Biological Chemistry*, 273(40):25529–25532, 1998.

[108] Luca Grisanti, Dorothea Pinotsi, Ralph Gebauer, Gabriele S Kaminski Schierle, and Ali A Hassanali. A computational study on how structure influences the optical properties in model crystal structures of amyloid fibrils. *Physical Chemistry Chemical Physics*, 19(5):4030–4040, 2017.

[109] Bin Chen, Ivaylo Ivanov, Michael L Klein, and Michele Parrinello. Hydrogen bonding in water. *Physical Review Letters*, 91(21):215503, 2003.

[110] Michele Ceriotti, Jérôme Cuny, Michele Parrinello, and David E Manolopoulos. Nuclear quantum effects and hydrogen bond fluctuations in water. *Proceedings of the National Academy of Sciences*, 110(39):15591–15596, 2013.

[111] Federico Giberti, Ali A Hassanali, Michele Ceriotti, and Michele Parrinello. The role of quantum effects on structural and electronic fluctuations in neat and charged water. *The Journal of Physical Chemistry B*, 118(46):13226–13235, 2014.

[112] Michele Ceriotti, Wei Fang, Peter G Kusalik, Ross H McKenzie, Angelos Michaelides, Miguel A Morales, and Thomas E Markland. Nuclear quantum effects in water and aqueous systems: Experiment, theory, and current challenges. *Chemical reviews*, 116(13):7529–7550, 2016.

[113] Bet Pamuk, Jose M Soler, R Ramírez, CP Herrero, PW Stephens, PB Allen, and M-V Fernández-Serra. Anomalous nuclear quantum effects in ice. *Physical review letters*, 108(19):193003, 2012.

[114] Ali A Hassanali, Jerome Cuny, Michele Ceriotti, Chris J Pickard, and Michele Parrinello. The fuzzy quantum proton in the hydrogen chloride hydrates. *Journal of the American Chemical Society*, 134(20):8557–8569, 2012.

[115] Yevhen Horbatenko and Sergei F Vyboishchikov. Hydrogen motion in proton sponge cations: A theoretical study. *ChemPhysChem*, 12(6):1118–1129, 2011.

[116] Agnieszka J Bieńko, Zdzisław Latajka, Wanda Sawka-Dobrowolska, Lucjan Sobczyk, Valery A Ozeryanskii, Alexander F Pozharskii, Eugeniusz Grech, and Joanna Nowicka-Scheibe. Low barrier hydrogen bond in protonated proton sponge. x-ray diffraction, infrared, and theoretical ab initio and density functional theory studies. *The Journal of chemical physics*, 119(8):4313–4319, 2003.

[117] Ji Chen, Xin-Zheng Li, Qianfan Zhang, Angelos Michaelides, and Enge Wang. Nature of proton transport in a water-filled carbon nanotube and in liquid water. *Physical Chemistry Chemical Physics*, 15(17):6344–6349, 2013.

[118] Yuki Nagata, Ruben E Pool, Ellen HG Backus, and Mischa Bonn. Nuclear quantum effects affect bond orientation of water at the water-vapor interface. *Physical review letters*, 109(22):226101, 2012.

[119] Ross H McKenzie, Christiaan Bekker, Bijyalaxmi Athokpam, and Sai G Ramesh. Effect of quantum nuclear motion on hydrogen bonding. *The Journal of chemical physics*, 140(17):174508, 2014.

[120] Michele Ceriotti and David E Manolopoulos. Efficient first-principles calculation of the quantum kinetic energy and momentum distribution of nuclei. *Physical review letters*, 109(10):100604, 2012.

[121] Nicola Marzari and David Vanderbilt. Maximally localized generalized wannier functions for composite energy bands. *Physical review B*, 56(20):12847, 1997.

[122] Nicola Marzari, Arash A Mostofi, Jonathan R Yates, Ivo Souza, and David Vanderbilt. Maximally localized wannier functions: Theory and applications. *Reviews of Modern Physics*, 84(4):1419, 2012.

[123] Pier Luigi Silvestrelli and Michele Parrinello. Water molecule dipole in the gas and in the liquid phase. *Physical Review Letters*, 82(16):3308, 1999.

[124] Pier Luigi Silvestrelli and Michele Parrinello. Structural, electronic, and bonding properties of liquid water from first principles. *The Journal of chemical physics*, 111(8):3572–3580, 1999.

[125] Xin-Zheng Li, Brent Walker, and Angelos Michaelides. Quantum nature of the hydrogen bond. *Proceedings of the National Academy of Sciences*, 108(16):6369–6373, 2011.

[126] Sathyapriya Rajagopal and Saraswathi Vishveshwara. Short hydrogen bonds in proteins. *The FEBS journal*, 272(8):1819–1832, 2005.

[127] Dominik Marx. Proton transfer 200 years after von grotthuss: Insights from ab initio simulations. *ChemPhysChem*, 7(9):1848–1870, 2006.

[128] Noam Agmon. The grotthuss mechanism. *Chemical Physics Letters*, 244(5-6):456–462, 1995.

[129] Mark Tuckerman, Kari Laasonen, Michiel Sprik, and Michele Parrinello. Ab initio molecular dynamics simulation of the solvation and transport of h3o+ and oh-ions in water. *The Journal of Physical Chemistry*, 99(16):5749–5752, 1995.

[130] James T Hynes. Physical chemistry: The protean proton in water. *Nature*, 397(6720):565, 1999.

[131] Omar F Mohammed, Dina Pines, Jens Dreyer, Ehud Pines, and Erik TJ Nibbering. Sequential proton transfer through water bridges in acid-base reactions. *Science*, 310(5745):83–86, 2005.

[132] Linas Vilčiauskas, Mark E Tuckerman, Gabriel Bester, Stephen J Paddison, and Klaus-Dieter Kreuer. The mechanism of proton conduction in phosphoric acid. *Nature chemistry*, 4(6):461, 2012.

[133] Ali Hassanali, Federico Giberti, Jérôme Cuny, Thomas D Kühne, and Michele Parrinello. Proton transfer through the water gossamer. *Proceedings of the National Academy of Sciences*, 110(34):13723–13728, 2013.

[134] Felix Franks. *Water: a matrix of life*. Royal Society of Chemistry, 2007.

[135] Robinson G Wilse, Singh Surjit, et al. *Water in biology, chemistry and physics: experimental overviews and computational methodologies*, volume 9. World Scientific, 1996.

[136] Philip Ball. Water as an active constituent in cell biology. *Chemical reviews*, 108(1):74–108, 2008.

[137] David Chandler. Interfaces and the driving force of hydrophobic assembly. *Nature*, 437(7059):640, 2005.

[138] Janet S Finer-Moore, Anthony A Kossiakoff, James H Hurley, Thomas Earnest, and Robert M Stroud. Solvent structure in crystals of trypsin determined by x-ray and neutron diffraction. *Proteins: Structure, Function, and Bioinformatics*, 12(3):203–222, 1992.

[139] DI Svergun, S Richard, MHJ Koch, Z Sayers, S Kuprin, and G Zaccai. Protein hydration in solution: experimental observation by x-ray and neutron scattering. *Proceedings of the National Academy of Sciences*, 95(5):2267–2272, 1998.

[140] Franci Merzel and Jeremy C Smith. Is the first hydration shell of lysozyme of higher density than bulk water? *Proceedings of the National Academy of Sciences*, 99(8):5378–5383, 2002.

[141] Gottfried Otting, Edvards Liepinsh, and Kurt Wuthrich. Protein hydration in aqueous solution. *Science*, 254(5034):974–980, 1991.

[142] Edvards Liepinsh, Gottfried Otting, and Kurt Wüthrich. Nmr observation of individual molecules of hydration water bound to dna duplexes: direct evidence for a spine of hydration water present in aqueous solution. *Nucleic acids research*, 20(24):6549–6553, 1992.

[143] Nathaniel V Nucci, Maxim S Pometun, and A Joshua Wand. Mapping the hydration dynamics of ubiquitin. *Journal of the American Chemical Society*, 133(32):12326–12329, 2011.

[144] Nathaniel V Nucci, Maxim S Pometun, and A Joshua Wand. Site-resolved measurement of water-protein interactions by solution nmr. *Nature structural & molecular biology*, 18(2):245, 2011.

[145] ZF Brotzakis, CCM Groot, W Homsi Brandeburgo, HJ Bakker, and PG Bolhuis. Dynamics of hydration water around native and misfolded α-lactalbumin. *The Journal of Physical Chemistry B*, 120(21):4756–4766, 2016.

[146] Daniela Russo, Greg Hura, and Teresa Head-Gordon. Hydration dynamics near a model protein surface. *Biophysical journal*, 86(3):1852–1862, 2004.

[147] K Wood, M Plazanet, F Gabel, B Kessler, D Oesterhelt, DJ Tobias, G Zaccai, and M Weik. Coupling of protein and hydration-water dynamics in biological membranes. *Proceedings of the National Academy of Sciences*, 104(46):18049–18054, 2007.

[148] Giorgio Schirò, Yann Fichou, Francois-Xavier Gallat, Kathleen Wood, Frank Gabel, Martine Moulin, Michael Härtlein, Matthias Heyden, Jacques-Philippe Colletier, Andrea Orecchini, et al. Translational diffusion of hydration water correlates with functional motions in folded and intrinsically disordered proteins. *Nature communications*, 6:6490, 2015.

[149] Daniela Russo, Rajesh K Murarka, John RD Copley, and Teresa Head-Gordon. Molecular view of water dynamics near model peptides. *The Journal of Physical Chemistry B*, 109(26):12966–12975, 2005.

[150] Francesco Pizzitutti, Massimo Marchi, Fabio Sterpone, and Peter J Rossky. How protein surfaces induce anomalous dynamics of hydration water. *The Journal of Physical Chemistry B*, 111(26):7584–7590, 2007.

[151] Vladimir A Makarov, B Kim Andrews, Paul E Smith, and B Montgomery Pettitt. Residence times of water molecules in the hydration sites of myoglobin. *Biophysical journal*, 79(6):2966–2974, 2000.

[152] Aoife C Fogarty and Damien Laage. Water dynamics in protein hydration shells: The molecular origins of the dynamical perturbation. *The Journal of Physical Chemistry B*, 118(28):7715–7729, 2014.

[153] Richard H Henchman and J Andrew McCammon. Structural and dynamic properties of water around acetylcholinesterase. *Protein Science*, 11(9):2080–2090, 2002.

[154] Tanping Li, Ali A Hassanali, Ya-Ting Kao, Dongping Zhong, and Sherwin J Singer. Hydration dynamics and time scales of coupled water- protein fluctuations. *Journal of the American Chemical Society*, 129(11):3376–3382, 2007.

[155] A Luise, M Falconi, and A Desideri. Molecular dynamics simulation of solvated azurin: correlation between surface solvent accessibility and water residence times. *Proteins: Structure, Function, and Bioinformatics*, 39(1):56–67, 2000.

[156] Peter J Rossky and Martin Karplus. Solvation. a molecular dynamics study of a dipeptide in water. *Journal of the American Chemical Society*, 101(8):1913–1937, 1979.

[157] Matthias Heyden and Douglas J Tobias. Spatial dependence of protein-water collective hydrogen-bond dynamics. *Physical review letters*, 111(21):218101, 2013.

[158] Angel E García and Gerhard Hummer. Water penetration and escape in proteins. *Proteins: Structure, Function, and Bioinformatics*, 38(3):261–272, 2000.

[159] Damien Laage, Guillaume Stirnemann, and James T Hynes. Why water reorientation slows without iceberg formation around hydrophobic solutes. *The Journal of Physical Chemistry B*, 113(8):2428–2435, 2009.

[160] Pooja Rani and Parbati Biswas. Diffusion of hydration water around intrinsically disordered proteins. *The Journal of Physical Chemistry B*, 119(42):13262–13270, 2015.

[161] Sander Pronk, Erik Lindahl, and Peter M Kasson. Dynamic heterogeneity controls diffusion and viscosity near biological interfaces. *Nature communications*, 5:3034, 2014.

[162] S Dellerue and M-C Bellissent-Funel. Relaxational dynamics of water molecules at protein surface. *Chemical Physics*, 258(2-3):315–325, 2000.

[163] Damien Laage and James T Hynes. Reorientional dynamics of water molecules in anionic hydration shells. *Proceedings of the National Academy of Sciences*, 104(27):11167–11172, 2007.

[164] Horace R Drew and Richard E Dickerson. Structure of a b-dna dodecamer: Iii. geometry of hydration. *Journal of molecular biology*, 151(3):535–556, 1981.

[165] Saumyak Mukherjee, Sayantan Mondal, and Biman Bagchi. Mechanism of solvent control of protein dynamics. *Physical Review Letters*, 122(5):058101, 2019.

[166] Patricia A Thiel and Theodore E Madey. The interaction of water with solid surfaces: fundamental aspects. *Surface Science Reports*, 7(6-8):211–385, 1987.

[167] David T Limmer, Adam P Willard, Paul Madden, and David Chandler. Hydration of metal surfaces can be dynamically heterogeneous and hydrophobic. *Proceedings of the National Academy of Sciences*, 110(11):4200–4205, 2013.

[168] Theanne Schiros, Osamu Takahashi, Klas J Andersson, Henrik Öström, Lars GM Pettersson, Anders Nilsson, and Hirohito Ogasawara. The role of substrate electrons in the wetting of a metal surface. *The Journal of chemical physics*, 132(9):094701, 2010.

[169] H Ogasawara, B Brena, D Nordlund, M Nyberg, A Pelmenschikov, LGM Pettersson, and A Nilsson. Structure and bonding of water on pt (111). *Physical review letters*, 89(27):276102, 2002.

[170] A Vittadini, A Selloni, FP Rotzinger, and M Grätzel. Structure and energetics of water adsorbed at tio 2 anatase\(101\) and\(001\) surfaces. *Physical Review Letters*, 81(14):2954, 1998.

[171] Sebastien Kerisit, David J Cooke, Dino Spagnoli, and Stephen C Parker. Molecular dynamics simulations of the interactions between water and inorganic solids. *Journal of Materials Chemistry*, 15(14):1454–1462, 2005.

[172] D Thirumalai, Govardhan Reddy, and John E Straub. Role of water in protein aggregation and amyloid polymorphism. *Accounts of chemical research*, 45(1):83–92, 2011.

[173] Matteo Salvalaglio, Thomas Vetter, Federico Giberti, Marco Mazzotti, and Michele Parrinello. Uncovering molecular details of urea crystal growth in the presence of additives. *Journal of the American Chemical Society*, 134(41):17221–17233, 2012.

[174] Stefano Piana, Franca Jones, and Julian D Gale. Assisted desolvation as a key kinetic step for crystal growth. *Journal of the American Chemical Society*, 128(41):13568–13574, 2006.

[175] Paolo Raiteri and Julian D. Gale. Water is the key to nonclassical nucleation of amorphous calcium carbonate. *Journal of the American Chemical Society*, 132(49):17623–17634, 2010. PMID: 21090620.

[176] Mark James Abraham, Teemu Murtola, Roland Schulz, Szilárd Páll, Jeremy C Smith, Berk Hess, and Erik Lindahl. Gromacs: High performance molecular simulations through multi-level parallelism from laptops to supercomputers. *SoftwareX*, 1:19–25, 2015.

[177] William L Jorgensen, David S Maxwell, and Julian Tirado-Rives. Development and testing of the opls all-atom force field on conformational energetics and properties of organic liquids. *Journal of the American Chemical Society*, 118(45):11225–11236, 1996.

[178] William L Jorgensen, Jayaraman Chandrasekhar, Jeffry D Madura, Roger W Impey, and Michael L Klein. Comparison of simple potential functions for simulating liquid water. *The Journal of chemical physics*, 79(2):926–935, 1983.

[179] William L Jorgensen and Jeffry D Madura. Temperature and size dependence for monte carlo simulations of tip4p water. *Molecular Physics*, 56(6):1381–1392, 1985.

[180] Nicolas Foloppe and Alexander D MacKerell, Jr. All-atom empirical force field for nucleic acids: I. parameter optimization based on small molecule and condensed phase macromolecular target data. *Journal of computational chemistry*, 21(2):86–104, 2000.

[181] Tom Darden, Darrin York, and Lee Pedersen. Particle mesh ewald: An n log (n) method for ewald sums in large systems. *The Journal of chemical physics*, 98(12):10089–10092, 1993.

[182] Berk Hess, Henk Bekker, Herman JC Berendsen, and Johannes GEM Fraaije. Lincs: a linear constraint solver for molecular simulations. *Journal of computational chemistry*, 18(12):1463–1472, 1997.

[183] Michele Parrinello and Aneesur Rahman. Polymorphic transitions in single crystals: A new molecular dynamics method. *Journal of Applied physics*, 52(12):7182–7190, 1981.

[184] Ramona S Taylor, Liem X Dang, and Bruce C Garrett. Molecular dynamics simulations of the liquid/vapor interface of spc/e water. *The Journal of Physical Chemistry*, 100(28):11720–11725, 1996.

[185] Subramanian Vaitheeswaran, Hao Yin, Jayendran C Rasaiah, and Gerhard Hummer. Water clusters in nonpolar cavities. *Proceedings of the National Academy of Sciences*, 101(49):17002–17005, 2004.

[186] OH Griffith, PJ Dehlinger, and SP Van. Shape of the hydrophobic barrier of phospholipid bilayers (evidence for water penetration in biological membranes). *The Journal of membrane biology*, 15(1):159–192, 1974.

[187] Cui Zhang and Giulia Galli. Dipolar correlations in liquid water. *The Journal of chemical physics*, 141(8):084504, 2014.

[188] SH Chung and JR Stevens. Time-dependent correlation and the evaluation of the stretched exponential or kohlrausch–williams–watts function. *American Journal of Physics*, 59(11):1024–1030, 1991.

[189] Claudia Rocchi, Anna Rita Bizzarri, and Salvatore Cannistraro. Water dynamical anomalies evidenced by molecular-dynamics simulations at the solvent-protein interface. *Physical Review E*, 57(3):3315, 1998.

[190] William L Jorgensen and Julian Tirado-Rives. Potential energy functions for atomic-level simulations of water and organic and biomolecular systems. *Proceedings of the National Academy of Sciences*, 102(19):6665–6670, 2005.

[191] Fabio Sterpone, Gino Marchetti, Carlo Pierleoni, and Massimo Marchi. Molecular modeling and simulation of water near model micelles: diffusion, rotational relaxation and structure at the hydration interface. *The Journal of Physical Chemistry B*, 110(23):11504–11510, 2006.